MODELING AND INTERPRETATION OF IN-SITU RADIOMETRIC FLUX MEASUREMENTS ON THE SURFACE OF ASTEROID (162173) RYUGU

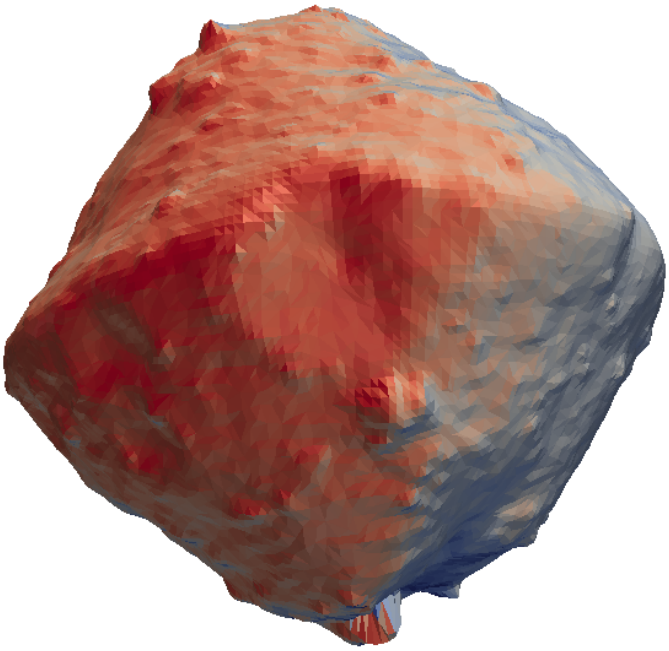

Dissertation
zur Erlangung des akademischen Grades
"doctor rerum naturalium"
(Dr. rer. nat.)

vorgelegt von M.Sc. Maximilian Hamm

im Fachbereich Geowissenschaften
der Freien Universität Berlin
Berlin, 2019

Erstgutachter: Prof. Dr. Ralf Jaumann
Zweitgutachter: Prof. Dr. Kai Wünnemann

Tag der Disputation: 14.11.2019

EIDESSTATTLICHE ERKLÄRUNG

Hiermit erkläre ich, dass ich die beigefügte Dissertation selbständig verfasst und keine anderen als die angegebenen Hilfsmittel genutzt habe.

Ich versichere weiterhin, dass ich die beigefügte Dissertation nur in diesem und keinem anderen Promotionsverfahren eingereicht habe und, dass diesem Promotionsverfahren keine endgültig gescheiterten Promotionsverfahren vorausgegangen sind.

Berlin, 05.08.2019

Maximilian Hamm

to Andrea

A good day is a day
when I learn something new

— William "Bill" D. Phillips, Lindau Nobel Laureate Meeting 2019

亀は …「お礼に太郎さんを竜宮城へお連れしましょう。

さあ、背中に乗ってください」と誘いました。

太郎は竜宮城へ行ってみたいと思い…

The turtle then extended an invitation. "In return, please allow me to show you Ryugu-jo, the palace of the Dragon King. Come, ride on my back." Taro thought he would indeed like to see Ryugu-jo.
(From "The Tale of Urashima Taro")[1]

1 https://www.gov-online.go.jp/eng/publicity/book/hlj/html/201407/201407_09_jp.html

DANKSAGUNG

Ich möchte zuallererst meinen größten Dank an Matthias Grott richten, der mich in den letzten vier Jahren enorm unterstützt hat. Ich wurde von Anfang intensiv in die Hayabusa2-Mission eingebunden, konnte unglaublich viel erfahren und lernen. Ich hatte viel Freiraum, konnte für drei Monate ins Ausland und habe von ihm viel über Betreuung, Schreiben und Präsentieren gelernt. Darüber hinaus hatte er stets ein offenes Ohr, für die zahllosen Sorgen die eine Dissertation begleiten und stand mir immer mit gutem Rat zur Seite. Durch meine Arbeit in der Doktorandenvertretung wurde ich mit den Erfahrungen anderer DoktorandInnen konfrontiert und mir wurde bewusst, dass eine Betreuung wie ich sie erfahren durfte in keiner Weise selbstverständlich ist. Matthias, ich bin dir sehr dankbar für dein Engagement, deine Geduld und die tollen Erfahrungen, die ich in dieser Mission machen durfte.

Diese Arbeit ist meiner Frau Andrea gewidmet, die mir mit Liebe, Offenheit und Verständnis den Antrieb, den Halt und die Kraft gegeben hat, mit der ich die Arbeit schreiben konnte. Andrea, du unterstützt mich bei allem was ich tue und ich bin dir unendlich dankbar dafür. Viel Unterstützung habe ich auch von meinen Eltern und Geschwistern erhalten, die mir immer den Rücken gestärkt haben. Meinen Freunden will ich an dieser Stelle ebenfalls dafür danken, ihr wart Teil dieser Reise und eure Freundschaft und vielfältiges Feedback haben mich sehr unterstützt: Danke an Leo, Alex, Fabi, Linda, Dave, Massi, Diana, Thilo und Lisa, and special thanks to Ihor.

Ich möchte mich außerdem herzlich bei Professor Jaumann bedanken, die Doktorvaterschaft übernommen zu haben und auch bei Professor Wünnemann dafür, dass Sie beide sich als Gutachter bereiterklärt haben.

I was extremely lucky to do my PhD in the frame of a fantastic mission, the Japanese Hayabusa2, which allowed to me to travel to Japan on numerous occasions, and work with a great team. I thank the Japanese Society for the Promotion of Science to fund a three month research project that allowed me to live in Japan and work with amazing colleagues. First of all, I want to thank Senshu-san, who supervised my work in Japan, spend enormous time and effort to help me in Japan and introduced me to the wonders of Japanese culture, food and drinks. I enjoyed my time in Japan and I am very grateful for this wonderful experience. Thank you Matsui-sensei, Wada-san, Ishimaru-san, Yamada-san, Maeda-san, Arai-san, Ishibashi-san and the entire PERC team, and a special thank you to the secretaries of PERC who helped me a lot with my everyday life in Japan. I also want to thank my friends Mayuko and Hiroka, I hope we stay in touch forever. I would also like to thank Okada-san for including me in the TIR team, thank you Yoshikawa-sensei und Tsuda-sensei for letting me be part of the mission, thank you Naoya, Sugita-san, and Miyamoto-sensei. I want to thank Kazunori

Ogawa, who spend time in Berlin, thank you for your help and friendship, and the invitation to come to Kobe, which was a great experience, let's write many more papers together!

Ich möchte weiterhin meinen Kollegen vom DLR danken, die mir ein tolles, stimulierendes Umfeld, viel Hilfe und Rat gegeben haben. Vielen Dank an Professor Doris Breuer, Jörg, Ekkehard, David, Paul, Tina, Nils, der Flammkuchengruppe, Barbara, Frank, KDM, Stefano, meinen Doktorandensprecherkollegen Indhu, Tanja, und Gregor, meinen DoVe-Freunden Nils, Felix, Basi, und Sahar, und meinen MASCOT-Kollegen Jens, Michael, Stefan sowie dem gesamten restliche Team.

Letztendlich will ich auch dem Steuerzahler für die Finanzierung von MASCOT danken. Wir haben meines Erachtens nach das Beste herausgeholt viel Neues über Asteroiden gelernt.

Herzlichen Dank, Thank you and Arigatou,

Max

ABSTRACT

In the presented work, a thermophysical model was developed to calculate the temperature evolution of the surface of asteroid (162173) Ryugu. This asteroid is the target of the Hayabusa2 sample return mission, which carried a lander called Mobile Asteroid surface SCOut (MASCOT). The MASCOT RAdiometer (MARA) measured infrared fluxes emitted by the surface and these measurements were modeled and interpreted using the temperatures calculated with the thermophysical model. The thermophysical properties of Ryugu's surface material were retrieved, and the distribution of thermal forcing acting on the surface of Ryugu, which could cause rock breakdown through thermal fatigue, was studied. This thesis is a cumulative work comprising three studies that were published in peer-reviewed journals.

In the first study, the thermophysical model is presented along with a radiative heat transfer model that relates the simulated temperatures to the MARA measurements and which can account for an arbitrarily complex asteroid surface. The study also presents a method to derive the thermophysical properties of the surface by comparing the modeled fluxes to the observed ones. The presented method allows for the retrieval of thermal inertia, emissivity and rock abundance of the surface, and the study shows that the spectral slope between 6 and 15 µm should be derivable from MARA observations.

In a second study, the thermophysical model was used to study the thermal environment on a spherical atmosphereless body. The diurnal temperature range, which is the main driver of thermal fatigue, was investigated as a function of thermal inertia and rotation axis orientation. It was found that the latitude of the maximum diurnal temperature range is determined by the balance between length of night and insolation power and not limited to the equator. The results imply that most of Ryugu's surface is exposed to similar amounts of thermal forcing.

The third study presents the analysis of the data collected by MARA while observing the temperature evolution of a single boulder on the surface of Ryugu. Here, the model developed in the first study was used to calculate the temperature evolution of the surface within the field of view of MARA, taking the unknown surface orientation and complex illumination condition into consideration. By using the radiative heat transfer model and parameter estimation method presented in the first study, the thermal inertia of the boulder was constrained to a surprisingly low 247-375 $\mathrm{J\,m^{-2}\,K^{-1}\,s^{-1/2}}$. This result indicates a high porosity of the boulder material of 28 to 55% which is consistent with CI or CM chondrites and which is also consistent with observations of other Hayabusa2 and MASCOT instruments. The high porosity implies that Ryugu formed from an aqueously altered and highly porous parent body.

ZUSAMMENFASSUNG

In dieser Doktorarbeit wurde ein thermophysikalisches Modell entwickelt, um Oberflächentemperaturentwicklung des Asteroiden (162173) Ryugu zu berechnen. Dieser Asteroid ist das Ziel der japanischen Hayabusa2-Mission. Im Rahmen dieser Mission sollen Proben des Asteroiden zur Erde gebracht werden und es wurde der Lander "Mobile Asteroid surface SCOut"(MASCOT) auf seiner Oberfläche abgesetzt. Das MASCOT-Radiometer (MARA), eines der Instrumente an Bord von MASCOT, maß die Infrarotstrahlung, die von der Oberfläche emittiert wurde. Diese Messungen konnten mit den berechneten Oberflächentemperaturen modelliert und interpretiert werden. Auf diese Weise konnten Oberflächeneigenschaften wie die thermische Trägheit ermittelt werden und die Verteilung thermo-mechanischer Ermüdung des Asteroidenmaterials untersucht werden. Diese Dissertation ist eine kumulative Arbeit und beinhaltet drei nach Peer-Review-Verfahren veröffentlichte Artikel.

Die erste Studie stellt das erwähnte thermophysikalische Modell vor. Es wurde ein Wärmetransfermodell entwickelt, welches aus den berechneten Oberflächentemperaturen einer beliebig komplexen Oberfläche die entsprechenden MARA Daten simulieren kann. Weiterhin wurde eine Methode dargestellt, mit der die Oberflächeneigenschaften aus den Messdaten abgeleitet werden konnten. Die Studie zeigt, dass die thermische Trägheit, sowie der Emissionsgrad und der Anteil an grobem Material der Oberfläche mit MARA abgeschätzt werden können. Die Arbeit zeigte außerdem, dass mit dem MARA-Instrument der Anstieg des Spektrums im Bereich von 6 bis 15 µm ermittelt werden kann.

Die zweite Studie befasst sich mit der Abhängigkeit des täglichen Temperaturkontrasts vom Breitengrad auf atmosphärelosen, sphärischen Körpern. Dieser Temperaturkontrast ist der wesentliche Treiber von thermo-mechanischer Ermüdung von Regolith auf dem Asteroiden und wurde als Funktion der thermischen Trägheit und der Ausrichtung der Rotationachse untersucht. Das Ergebnis war, dass der Breitengrad, an dem der Temperaturunterschied zwischen Tag und Nacht am größten ist, durch ein Gleichgewicht von Einstrahlungsleistung der Sonne und der Länge der Nacht festgelegt ist und dabei nicht nur auf den Äquator beschränkt ist. Aus dieser Untersuchung konnte abgeleitet werden, dass die Oberfläche von Ryugu größtenteils ähnlichen thermischen Kontrasten ausgesetzt wird.

Die dritte Studie befasst sich mit der Auswertung der MARA-Daten, welche die Temperaturentwicklung eines einzelnen Steins auf der Oberfläche Ryugus zeigen. Hier wurde das in der ersten Studie entwickelte Modell angewandt und zusätzlich wurden die unbekannte Ausrichtung der Oberfläche im Gesichtsfeld MARAs sowie die Wärmestrahlung der Umgebung berücksichtigt. Mit dem Wärmetransfermodell und

der Parameterschätzmethode aus der ersten Studie, konnte die thermische Trägheit nun auf 247-375 $\mathrm{J\,m^{-2}\,K^{-1}\,s^{-1/2}}$ geschätzt werden, was erstaunlich niedrig ist. Dieses Ergebnis lässt sich am ehesten mit einer sehr hohen Porosität des Steins von 28 bis 55% erklären. Die Porosität von CI- und CM-Chondriten ist ähnlich hoch und andere Instrumente von Hayabusa2 und MASCOT kommen zu einem vergleichbaren Ergebnis. Die hohe Porosität deutet darauf hin, dass sich Ryugu aus den Trümmern eines wässrig alterierten, porösen Körpers gebildet hat.

CONTENTS

LIST OF FIGURES

LIST OF TABLES

1 INTRODUCTION

1.1 ASTEROIDS AND METEORITES

Asteroids are remnants of the formation of the solar system and provide insights into processes that have shaped it. Furthermore, asteroids are gaining interest as possible sources of resources but also as a potential hazard to life on Earth (see e.g. the European NEOshield project, Harris et al. (2013)). Consequently, considerable effort is spent on the exploration of these objects. Large telescopic surveys were carried out measuring sizes and orbits of hundred thousands of asteroids (e.g. NEOWISE Mainzer et al. (2011)) and several robotic missions have been launched to investigate asteroids in detail, revealing the diversity among asteroids:

- 1989: Galileo to asteroids (951) Gaspra (Yeomans et al., 1993) and (243) Ida (Belton et al., 1996)
- 1996: NEAR Shoemaker to (253) Mathilde (Veverka et al., 1999) and (433) Eros (Prockter et al., 2002)
- 1999: Stardust flying by (5535) Annefrank (Duxbury et al., 2004)
- 2003: the first Hayabusa mission, a sample return mission to (25143) Itokawa (Fujiwara et al., 2006)
- 2004: Rosetta passing (2867) Steins (Keller et al., 2010) and (21) Lutetia (Schulz et al., 2012)
- 2007: Dawn to (4) Vesta and (1) Ceres (Russell et al., 2011)
- 2014: the sample return mission Haybusa2 to (162173) Ryugu (Watanabe et al., 2019), studied in this thesis
- 2016: the sample return mission OSIRIS-REx to (101955) Bennu (Lauretta et al., 2019)

Fig. 1.1 shows images of the asteroids (1) Ceres, (4) Vesta, (21) Lutetia, (433) Eros, (253) Mathilde, and (25143) Itokawa, which vary significantly in size, shape and surface structure. Ceres' shape is spherical, whereas Vesta is an oblate object. Asteroids, like Eros or Itokawa, are elongated, while others, like Mathilde or Lutetia, have an irregular shape. The size of the asteroids ranges from hundreds of kilometers (Ceres) to few hundred meters (Itokawa). Many asteroid surfaces are covered by craters. However, the

one of Itokawa is almost devoid of craters and Itokawa is an example of a "rubble-pile" asteroid, i.e. loosely bound fragments that re-accreted from a disrupted parent body. Many more missions to asteroids are currently proposed or under development (e.g., DART, DESTINY+, PSYCHE, LUCY).

There is not a clear definition of the term "asteroids". The International Astronomical Union (IAU) defines the terms "planets", "dwarf planets", and "small solar system bodies" and asteroids are a sub-group of the what the IAU defines as "small solar system bodies". The only exception is the large asteroid Ceres which is considered a dwarf planet by the IAU definition as its gravity is strong enough to overcome the rigid forces of its material, giving Ceres its round, spherical shape. Asteroids are distinct from comets as they do not form a coma. However, active asteroids exist where dust ejection produce transient phenomena similar to a cometary coma (Jewitt, 2012). Potential mechanism of this mass loss are rotational instability, impacts, electrostatic repulsion, radiation pressure, dehydration stresses, or thermal cracking (ibid.). An example for an active asteroid is (3200) Phaethon which ejects large amount of material causing the Geminids meteor shower. Phaethon has a perihelion of 0.14 astronomical units (AU) which causes surface temperatures above 1000 K that might lead to strong dehydration or thermal cracking that might drive Phaethon's dust ejection (ibid.). At the same time, comets can become inactive with time when they either lose all their volatiles or evolve to an orbit with less solar energy input where no activity is possible (Hartmann et al., 1987). Consequently, the line between active asteroids and inactive comets is blurred (Harris et al., 2001). Another group of small solar system bodies are the Trans-Neptunian Objects which are often considered to be a different from asteroids as they contain much more ice compared to asteroids and might be the source of comets. It is also debated whether centaurs, i.e. objects between the orbits of Jupiter and Neptune should be considered asteroids or not. Thus, for this work we define asteroids as those small solar system bodies on or inside the orbit of Jupiter, which are not comets, nor satellites.

1.1.1 *Asteroid Orbits and Families*

Since 2015, more than 700000 asteroids are known, most of them due to two large surveys, the Sloan Digital Sky Survey SDSS (Ivezić et al., 2001) and the Wide Field Infrared Survey Explorer WISE (Mainzer et al., 2011). Most of the known asteroids are located in the asteroid main belt between the orbits of Mars and Jupiter, having an estimated total mass of $5 \cdot 10^{-4}$ Earth masses of which one third is contributed by Ceres (DeMeo et al., 2015). The orbits of the main belt asteroids form patterns. Resonances with Jupiter's orbit cause gaps in the orbital distribution of main belt asteroids known as Kirkwood gaps (Dermott et al., 1983; Kirkwood, 1867). Furthermore, many asteroids form "families", which are groups of asteroids with similar, correlated

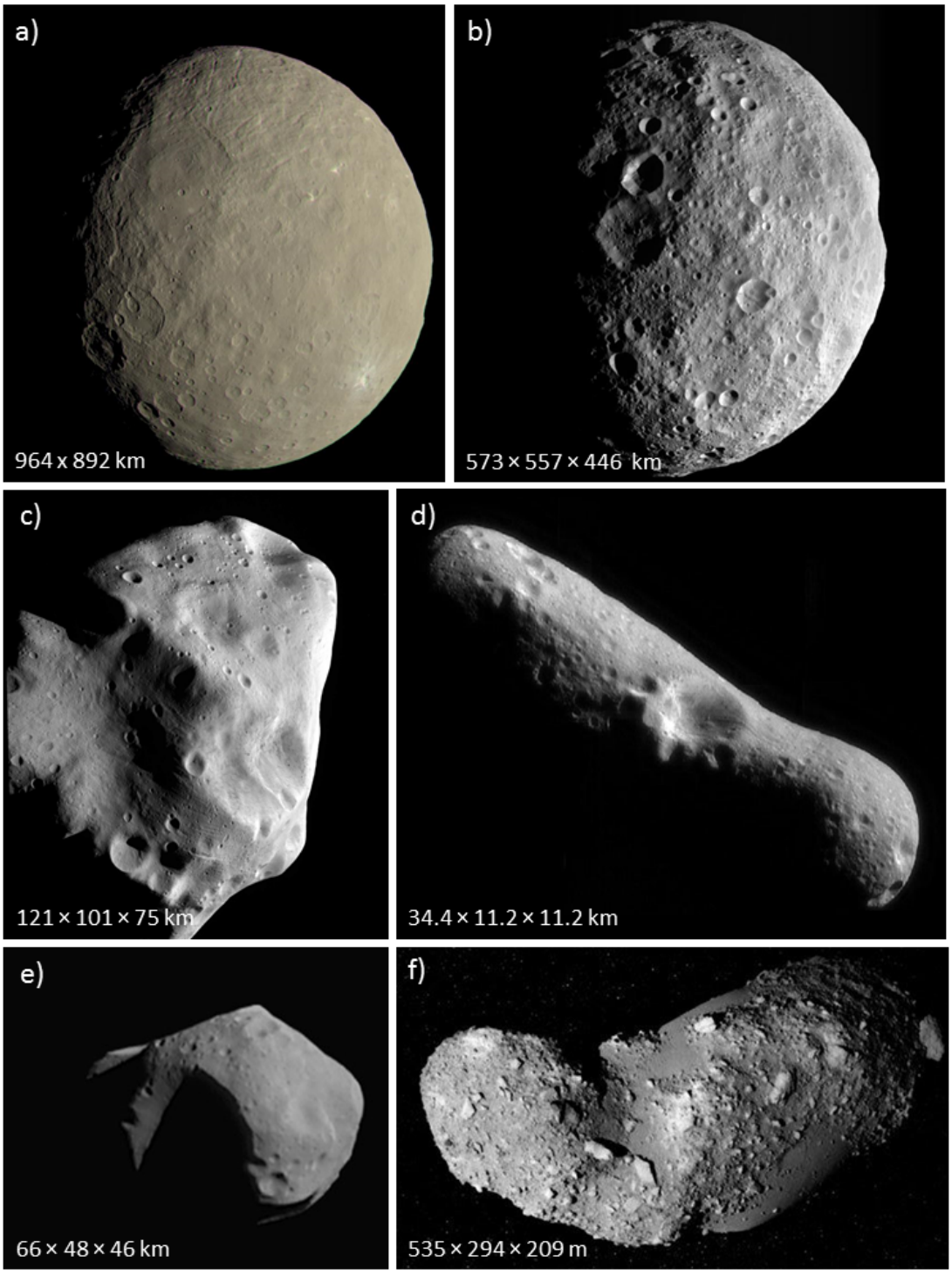

Figure 1.1: Images taken from cameras of spacecraft visiting a) Ceres b) Vesta c) Lutetia d) Eros e) Mathilde f) Itokawa. The numbers in the lower left corner of each image represent the average diameters of a three-axis ellipsoid approximating the asteroid shape. For Ceres, the equatorial diameter and the polar diameter are shown respectively. Image credit: a),b) NASA/JPL-Caltech/UCLA/MPS/DLR/IDA; c) ESA 2010 MPS for OSIRIS Team MPS/UPD/LAM/IAA/RSSD/INTA/UPM/DASP/IDA; d), e) NASA/JPL, f) JAXA

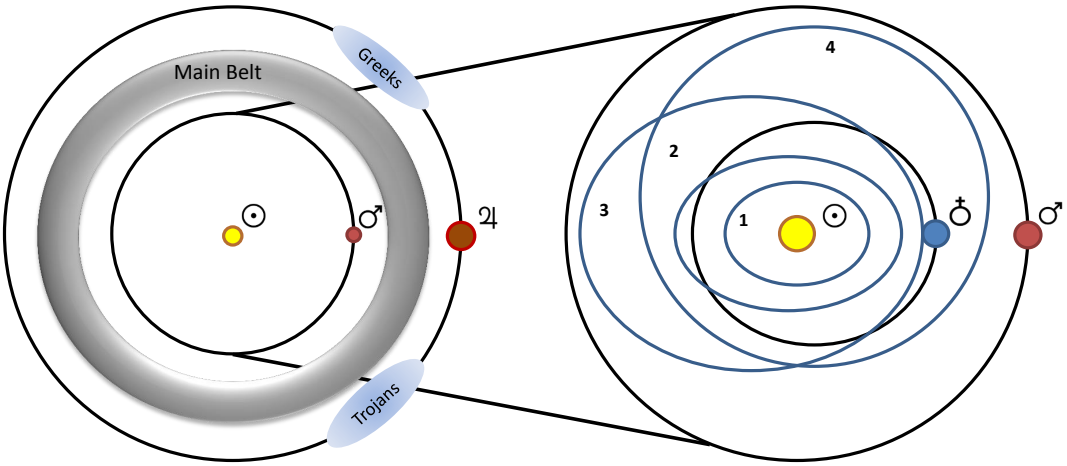

Figure 1.2: Sketch showing important groups of asteroids and their location in the solar system. Sun, Earth, Mars, and Jupiter are marked by their respective astronomical symbol. The main belt is represented by the gray ring. The Greeks and Trojans at the Jupiter Lagrange points L4 and L5 are indicated. The blue, numbered ellipses represent the orbits of four Near-Earth Asteroid groups: 1 - Atiras, 2 - Atens, 3 - Appolo, and 4 - Amor

orbital parameters. Their origins are believed to be catastrophic disruptions of larger parent bodies (Michel et al., 2015).

The outer boundary of the asteroid main belt is defined by a 2:1 resonance with Jupiter's orbit. Beyond this boundary three groups of asteroids are found, the Cybele asteroids with orbits between 3.3 to 3.5 AU, Hildae which are grouped at the 3:2 resonance with Jupiter at 4 AU and the Trojans (Binzel et al., 1992; Dahlgren et al., 1995). The latter are co-orbiting with Jupiter and located at its Lagrange points L4 and L5. The asteroids at L4 are called the Greeks and the ones at L5 Trojans, but the term "Jupiter Trojans" refers to both (see chapter by Emery et al. (2015) in Asteroids IV).

Some asteroids are found close to Earth's orbit, the Near-Earth Asteroids (NEA). They are grouped into four groups (see chapter by Binzel et al. (2015) in Asteroids IV): The Amor group consists of Near-Earth asteroids with orbits outside the the Earth's orbit but approaching it, with a perihelia larger than 1.017 AU (aphelion of Earth) but less than 1.3 AU and a semi-major axis larger than 1 AU. The Atiras have orbits situated inside Earth's orbit without crossing it, but very few have been found to date. The Atens asteroids have a semi-major axis smaller than 1 AU and an aphelion larger than Earth's perihelion at 0.983 AU. They cross the Earth's orbit but remain inside of it for most of their orbital period. The last group is the Apollo group with a semi-major axis larger 1 AU and a perihelion distance smaller than the aphelion distance of the Earth. They cross the Earth's orbit from the outside in. The different types of NEA orbits are illustrated as blue, numbered ellipses in Fig. 1.2, which also shows the Asteroid Main Belt and the Jupiter Trojans.

Taxonomic System	Tholen	Bus-DeMeo	Examples	Mission
S-complex	S	S	S - (951) Gaspra	Galileo
		Sa	S - (5535) Annefrank	Stardust
		Sq	S, Sq, Q - (25143) Itokawa	Hayabusa
		Sr	S - (243) Ida	Galileo
		Sv	S - (433) Eros	NEAR Shoemaker
C-complex	B	B	B - (101955) Bennu	OSIRIS-REx
	C	C	C - (1) Ceres	Dawn
	F	Cb	Cb - (162173) Ryugu	Hayabusa2/MASCOT
	G	Cg	Cb - (253) Mathilde	NEAR Shoemaker
		Cgh	B - (3200) Phaethon	Destiny+ (planned)
		Ch		
X-complex	E	X	M, Xc - (21) Lutetia	Rosetta
	M	Xc	E - (2867) Steins	Rosetta
	P	Xe	P - Trojans	Lucy (planned)
		Xk	Xk - (16) Psyche	Psyche (planned)
Others	T	T	S, Sq, Q - (25143) Itokawa	Hayabusa
	D	D	V - (4) Vesta	Dawn
	O	Q	D - Trojans	Lucy (planned)
	R	O		
	V	R		
	A	V		
		A		
		K		
		L		

Table 1.1: Overview of the Tholen (0.33 µm - 1 µm) and Bus-DeMeo (0.45 µm - 2.45 µm) taxonomic systems, derived from the table given by DeMeo et al. (2015). Examples of asteroids visited by spacecraft and future mission targets are listed with their respective spectral type.

1.1.2 *Spectral Classification of Asteroids*

A second way to classify asteroids is according to their ultraviolet (UV) to near-infrared (NIR) spectra, i.e. the wavelengths ranging from 0.38 µm to 3 µm (DeMeo et al., 2015). Generally, asteroids are are categorized in four groups: the S-complex with moderate silicate absorption features at 1 and 2 µm corresponding to Pyroxene and Olivine respectively, the C-complex with little features but a characteristic 0.7 µm feature indicating the presence of phyllosilicates, the X-complex with moderate spectral slope and no or few subtle features, and those asteroids matching none of the above. These

groups are further divided into various types according to their spectral slopes and features and multiple taxonomy systems of asteroids exist determining these types. Two taxonomy systems, the Tholen and Bus-DeMeo taxnomies, are briefly introduced in the following.

The Tholen taxonomy (Tholen et al., 1989) considers the asteroid spectra from a wavelength 0.33 µm to 1 µm. In the Tholen taxonomy the C-complex is divided into the B-, C-, F-, and G-types. The X-complex is divided into the E-, M- and P-types, and six more types (T, D, O, R, V, and A) are introduced in the "others" group. This taxonomy is commonly used and the terms C-type, S-type, or M-type asteroids refer to this system. As more NIR data became available with time e.g. through the SpeX instrument on the NASA InfraRed Telescope Facility (IRTF) (Rayner et al., 2003), the Bus-DeMeo taxonomy (DeMeo et al., 2009) was introduced incorporating the new data. This system categorizes asteroids into 24 types and considers a broader spectral range from 0.45 µm to 2.45 µm. An overview of these two taxonomic systems is provided in Tab. 1.1. The table also lists examples of asteroids that were visited by spacecraft, or will be visited in future missions. Attributing these asteroids to a single type in the Bus-DeMeo system can be difficult, as some asteroids are only categorized in the Tholen system but not in the Bus-DeMeo taxonomy. Furthermore, some asteroids show spectral features corresponding to various spectral types. For example, regolith on asteroid Itokawa ranges from spectral type S, over Sq to Q, which might indicate that these types represent different stages of space weathering (Koga et al., 2018).

The relative abundance of the various types varies with their orbital groups and an overview of distribution of asteroid classes by mass was provided by DeMeo et al. (2014). Among the NEAs, S-types are the most abundant asteroids. The C-type and B-type asteroids are together the second most numerous group of NEAs. The Q-types are also abundant among the NEAs which is surprising as they are rare elsewhere in the solar system. Compared to the inner main belt, the C-type asteroids are underrepresented among the NEAs (Binzel et al., 2015). In the inner main belt, the largest group are the V-types followed by S- and C-types. C-types become increasingly dominant in the mid and outer main belt where they constitute the largest fraction of mass. Beyond the main belt, the Cybele, Hildae and Trojans consist almost entirely of D- and P-types, with a small fraction of C-types mixed in (Dahlgren et al., 1997; DeMeo et al., 2015). These types of asteroids are considered to be among the first objects to form in the solar system such that the asteroids become increasingly primitive from the outer Belt towards the Trojans (Di Sisto et al., 2005).

1.1.3 *Meteorites*

To date, meteorites are the main source of extraterrestrial material delivered to Earth, besides lunar samples, interplanetary dust particles, and the small particles returned by the Stardust, Genesis and Hayabusa missions. Most of the meteorites are considered

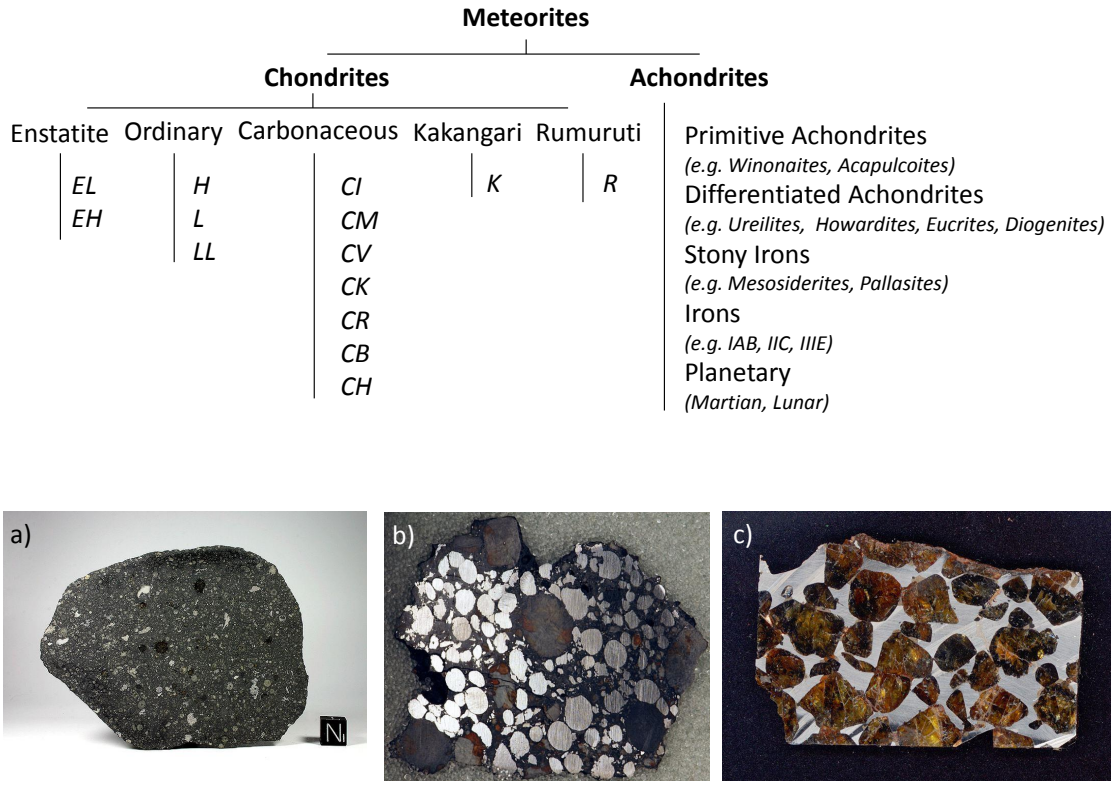

Figure 1.3: Overview of the meteorite classes which are divided into chondrites and achondrites. The images below show examples of meteorites: a) CV chondrite Allende, b) CB chondrite Gujba, c) Pallasite Pallasovka; Image Credit (CC 3.0): a) Matteo Chinellato, b) James St. John, c) Opsoelder

to be fragments of asteroids that collided with Earth, however some meteorites are fragments of the Moon and Mars that were probably ejected during large impacts. Meteorites are categorized according to an independent taxonomy system, based on their chemical composition, oxygen isotopes, and petrography. A review of this classification is provided by Krot et al. (2014) and is summarized in the chapter by DeMeo et al. (2015). Meteorites can be roughly grouped into undifferentiated meteorites (chondrites) and differentiated or partially differentiated ones (achondrites). An overview of the meteorite classification is provided in the upper part of Fig. 1.3. In the following, properties of meteorites will be discussed. While achondrites are briefly mentioned, this section focuses on chondrites, since Ryugu is believed to consist of chondritic material.

With the exception of the above-mentioned planetary meteorites, achondrites are believed to be melted or partially melted fragments of differentiated planetesimals. They are divided into several sub-groups such as irons, which might be fragments of

planetesimal cores, stony irons like the spectacular Pallasites, or stony, differentiated achondrites like the Howardites-Eucrites-Diogenites (HED). Fig. 1.3 c) shows the Pallasite Pallasovka which consists of olivine inclusions that are embedded in a metallic matrix.

Chondrites are primitive, unmelted fragments of undifferentiated small parent bodies or undifferentiated crusts of planetesimals (Neumann et al., 2018). They consist of refractory inclusions and chondrules, which both form at high temperatures (DeMeo et al., 2015), and a fine-grained matrix of dust particles and organics with grain sizes of 5-10 µm. The refractory inclusions encompass a variety of objects like the Calcium-Aluminum Inclusions (CAI) or Amoeboid Olivine Aggregates (AOA). CAIs are the oldest dated object in the solar system with an age of 4567.2 Myr (Connelly et al., 2012). Chondrules are round objects and might have formed 1-3 Myr (Kita et al., 2013) after the CAIs as molten silicate droplets. Absence of chondrites that formed later than 2-4 Myr suggests that planetesimal formation ceased at that point. The timing of these processes is inferred from isotope ratios in the chondrules (e.g. $^{26}Al/^{27}Al$) (Kita et al., 2013; Kleine et al., 2008; Ushikubo et al., 2013).

Generally, the composition of chondrites is similar to the one of the solar photosphere and therefore similar to the solar nebular. An exception are the light elements hydrogen, helium, carbon, and nitrogen, which were depleted by the activity of the early sun (Krot et al., 2014). The bulk composition differs slightly between the various types of chondrites and based on this elemental composition, as well as isotopic compositions, texture (e.g. chondrule abundance and size) mineralogy, and petrology chondrites are divided into five classes containing several groups each of which are briefly introduced in the following summary of the chapter by Krot et al. (ibid.).

Ordinary chondrites are the most common meteorites and divided into the H-, L-, and LL-groups which are distinguished by their iron content, where H represents high iron content, L stands for low iron content, and LL for lower iron content and low metal content (Kallemeyn et al., 1989). Enstatite chondrites are rare, highly reduced, i.e. less oxidized, meteorites and divided into EH-chondrites with relatively high iron content and EL-chondrites containing less iron (Sears et al., 1982). Rumuruti-like R-chondrites are similar to ordinary chondrites but differ from the other chondrites in their high $^{17}O/^{18}O$ ratio (Kallemeyn et al., 1996; Krot et al., 2014). The carbonaceous chondrites are a vast class divided into eight groups named after their respective type-meteorites: CI (Ivuna-like), CM (Mighei-like), CO (Ornans-like), CR (Renazzo-like), CK (Karoonda-like), CV (Vigarano-like), CB (Bencubbin-like). The CH is an exception and the "H" stands for high metal content. The eight groups differ in composition, oxygen isotope ratio as well as matrix abundance and chondrule size. The CI chondrites consist entirely of hydrated matrix with little to no chondrules present. The composition is primitive and matches closely the one of the solar photosphere (Krot et al., 2014). Contrarily, CB and CH contain almost no matrix. These two types contain a high amount of metallic chondrules with up to ten times high metal abundance compared to the other

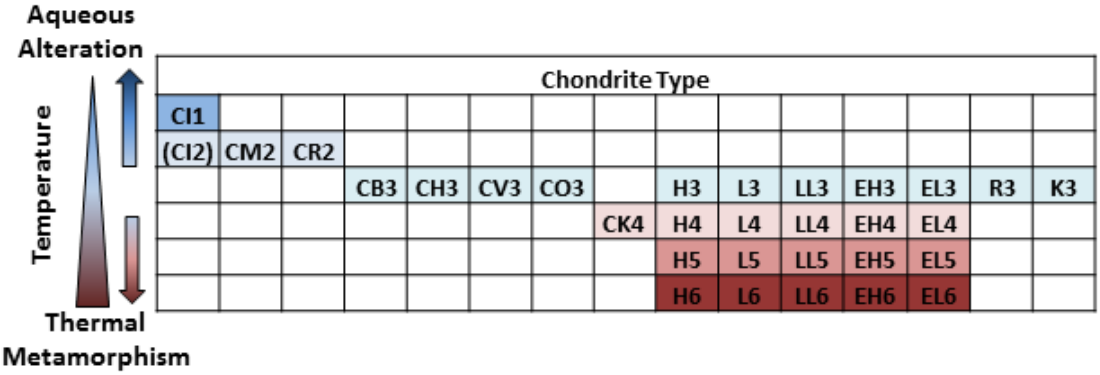

Figure 1.4: Overview of the petrologic types of chondrites, adapted from Koschny et al. (2019). The petrologic types are denoted by the number behind the chondrite chemical group, e.g. CV3 indicates petrologic type 3. With increasing temperature the alteration changes from aqueous alteration to thermal metamorphism.

types (ibid.). CM and CO chondrites show relatively small chondrules. However, CM chondrites contain much more matrix compared to CO chondrites. Furthermore, the chondrules in CM chondrites are metal-poor and enriched in phyllosilicates, whereas metal-rich chondrules are abundant in CO chondrites (Kallemeyn et al., 1981; Krot et al., 2014). CV and CK chondrites contain large chondrules with porphyritic textures, i.e. distinct difference in the size of crystal groups composing the chondrule. While the CV contain large CAIs and AOAs, CK contain very little of these inclusions, and show a higher abundance of matrix compared to CV chondrites (Kallemeyn et al., 1991). Only CI, CM and CR chondrites have a significantly higher abundance of carbon compared to non-carbonaceous chondrites and give this class its name. Kakangari (K) are another small group of rare meteorites combining properties of the other groups, e.g. a large matrix abundance with an enstatite enriched composition, a high metal content similar to H chondrites, and an oxidization state intermediate to enstatite chondrites and H chondrites (Krot et al., 2014; Weisberg et al., 1996). Fig. 1.3 a) and b) show two examples of chondritic meteorites. Image 1.3 a) shows the CV chondrite Allende with large, abundant chondrules and bright CAIs embedded in a dark matrix, b) shows the CB chondrite Gujba which contains large metal chondrules.

This list of chondrite properties is not exhaustive and more information on the complex and diverse differences among the chondrites can be found in the review by Krot et al. (2014) and references therein. In addition to the classification described above, meteorites are divided into petrologic types depending on the extent of thermal metamorphism and aqueous alteration, adding a number 1-6 to the chemical group, e.g. CI1, LL3 (Van Schmus et al., 1967). Depending on water abundance and temperature, the primary, original mineralogy and petrography can be altered. Aqueous alteration is caused by water that accreted with the respective parent bodies and the petrologic

types 1 and 2 denote such meteorites (Brearley, 2006). Chondrite types CM, CR and CI are aqueously altered and include hydrated minerals as well as free water (Jarosewich, 1990; Kallemeyn et al., 1981, 1994). In CI chondrites, all chondrules and CAIs have been destroyed by aqueous alteration, and the matrix is enriched in phyllosilicates and carbonates (Endreß et al., 1996; Krot et al., 2014). Contrarily, ordinary chondrites contain less water and are generally thermally metamorphosed. Metamorphism above 200-300C leads to the removal of water and dehydration of minerals (Akai, 1992; Muenow et al., 1995). Furthermore, it results in recrystallization of the minerals such that the matrix becomes increasingly transparent and the chondrules less defined (Krot et al., 2014; Van Schmus et al., 1967). The petrologic types 4-6 denote the thermally metamorphosed chondrites. Type 3 chondrites are the least altered and neither thermally metamorphosed nor aqueously altered. In these chondrites the pristine structures of chondrules and matrix is preserved. However, the most primitive elemental composition can be found in the heavily aqueously altered CI chondrites. An overview of the petrologic types of chondrites is provided in Fig. 1.4.

It is difficult to relate the well studied meteorites to specific asteroids. The spectra considered in the common asteroid taxonomies are generally featureless and it is thus challenging to infer the composition of asteroids. Furthermore, effects of grain size, temperature, viewing geometry, and space weathering affect the spectra (Reddy et al., 2015). Consequently, no clear mapping between spectral types and meteorite classes exists. Nevertheless, the achondritic HED meteorites are generally attributed to asteroid Vesta and the Dawn mission supports this assumption while showing that some HED meteorites might originate from a different body (McSween et al., 2010). Moreover, the S-complex is generally linked to ordinary chondrites. The first Hayabusa mission returned samples from the S-type asteroid Itokawa, and a clear link could be established between this sample and LL ordinary chondrites (Nakamura et al., 2011). However, while ordinary chondrites are by far the most common meteorite type, S-type asteroids are not the most common type of asteroids (DeMeo et al., 2015). Contrarily, the most common asteroid types belong to the C-complex and are assumed to be related to carbonaceous chondrites which are rare samples compared to ordinary chondrites. The sample return missions Hayabusa2 and OSIRIS-REx will visit a C-type and B-type asteroid respectively, which will contribute to the understanding of the link between carbonaceous chondrites and the corresponding asteroid types. While there are many more possible links between spectral types and meteorite groups, they remain to be established, e.g. by further sample return missions.

1.2 THERMAL INFRARED OBSERVATIONS

1.2.1 *Thermal Inertia*

Observations in the thermal infrared, i.e. at wavelengths between 5 and 25 µm, provide information on the nature of the surface material of planetary bodies. On the one hand, spectral features in the thermal infrared are diagnostic for many minerals (e.g. Emery et al., 2006; Salisbury et al., 1991, and see also section 3.1). On the other hand, the emission of objects in this spectral range is dominated by thermal emission of the surface, and can therefore be related to the thermal conditions of the surface (Harris et al., 2002). The temperature evolution as a response to insolation provides insights to the structural properties of the asteroid surface. The temperature response to insolation of a compact surface is significantly different to the one of a fine-grained regolith cover, or a porous surface.

The thermal response to insolation is generally parametrized in terms of the thermal inertia, and details of this parametrization will be discussed in chapter 3.3. The thermal inertia Γ describes the response of the surface temperature to the periodic forcing imposed by the diurnal insolation cycle. It determines the temperature range of such a diurnal cycle, where an increasing thermal inertia reduces the heating and cooling rate of the surface material. This reduces the daytime temperatures while increasing the nighttime temperatures and the higher the thermal inertia the smaller is the contrast between nighttime and daytime temperatures. Furthermore, the thermal inertia determines the phase lag between the diurnal insolation cycle and the diurnal temperature cycle, where the maximum temperatures are always delayed with respect to the maximum insolation. Surfaces with higher thermal inertia reach their maximum temperature later than surfaces with lower thermal inertia. The thermal inertia is a combination of k thermal conductivity, ρ density and c_p specific heat capacity and is given by:

$$\Gamma = \sqrt{k c_p \rho} \tag{1.1}$$

Through the thermal conductivity k, Γ is coupled to structural properties like grain size and porosity. High porosity and small grain size reduce the thermal conductivity and result in a low thermal inertia (see section 3.4.3). Consequently, observing the temperature evolution allows for the inference of structural properties of asteroid surfaces. The structure provides insights into the history of the asteroid, e.g. its formation, which is relevant for the understanding of solar system formation processes. In particular, the porosity is an important parameter in accretion models (Kataoka, Akimasa et al., 2013; Okuzumi et al., 2012; Ormel, C. W. et al., 2007).

Knowledge of the texture, e.g. the dominant grain size, and the strength of the surface material is essential for engineering interactions between a spacecraft and the asteroid.

This information is crucial for the planning of lander missions or sampling operations, and is also relevant for planning a possible deflection attempt if an asteroid impact is imminent on Earth. However, there are caveats in the derivation of grain size from thermal infrared observation if the regolith grains become too large, as discussed in section 3.6.

The diurnal temperature range of an asteroid surface influences the evolution of the surface material. Temperature differences between the interior of a boulder and its surface cause thermal stresses that can lead to the disintegration of the object (Delbo et al., 2014; Molaro et al., 2015, 2017). Thermal stress can lead to cracks and small pieces can be chipped off, forming small sized regolith. This process is called thermal fatigue and it links the thermal environment of the surface to the evolution of the regolith structure.

1.2.2 *Yarkovsky and YORP Effects*

The thermal conditions on the surface of an asteroid also influence the orbital evolution of the asteroid through the YORP and Yarkovsky effects (Bottke et al., 2006; Rubincam, 1995). The Yarkovsky effect describes the alteration of the asteroid's orbit due to thermal radiation pressure and finite thermal inertia. As described above, the thermal inertia causes a delay between the surface temperature maximum and the maximum insolation, where the peak temperatures are reached in the local afternoon. This causes a systematic anisotropy of the thermal radiation pressure, such that a net force acts on the asteroid throughout its orbit. For prograde rotating asteroids, this effect causes an acceleration and thus increases the semi-major axis of the orbit. For retrograde rotating asteroids the Yarkovksy effect causes deceleration and a decrease in the semi-major axis. Small asteroids are most affected by this and the strength of the effect depends on the heliocentric distance, surface thermal inertia, size, obliquity and rotation rate. As a result of the Yarkovsky effect, the orbits of asteroids change with time which increases the probability to encounter resonances with Jupiter. Furthermore, it causes dynamical spreading of asteroid families after their formation in catastrophic collisions (Bottke et al., 2006). Consequently, many current asteroid orbits could be significantly different from the orbit where they formed. It is therefore essential to take the Yarkovsky effect into consideration when tracing back asteroids to their original populations. The effect was directly measured for various asteroids including Near-Earth Asteroids which might pose an impact hazard as their orbits evolve (e.g. Farnocchia et al. (2013) and Nesvorný et al. (2004)).

The YORP effect (Yarkovsky–O'Keefe–Radzievskii–Paddack) describes the change in rotation axis and period due to anisotropic thermal radiation caused by an irregular shape of the asteroid. The original rotation period of an asteroid can increase or decrease with time and the obliquity will change as well (Bottke et al., 2006; Čapek et al., 2004). The effect strongly depends on the shape of the asteroid but also on its thermal inertia,

roughness, size, and albedo. It has been directly detected for small asteroids, e.g. 2000 PH5 (Lowry et al., 2007; Taylor et al., 2007).

Spin-up due to YORP effect can lead to mobilization of surface material and thus mass movement towards the equator (Bottke, 2008; Scheeres, 2015). In this case an equatorial ridge forms and the shape of the asteroid becomes similar to a spinning top. Examples for such asteroids are (66391) 1999 KW4 (Bottke, 2008; Walsh et al., 2008), (162173) Ryugu (Watanabe et al., 2019), and (101955) Bennu (Scheeres et al., 2019). Walsh et al. (2008) showed that the YORP effect has likely caused a mass shedding on 1999 KW4 which has resulted in the formation of a small satellite. They report that this could be a plausible mechanism to explain that 15 % of the near-Earth and main belt asteroids with diameters below 10 km have satellites. In the case of Bennu and Ryugu this mechanism is proposed to explain their shapes (Scheeres et al., 2019; Watanabe et al., 2019). Nevertheless, the studies report that it cannot yet be excluded that the shape and spin rate is primordial and a result of reaccretion after catastrophic disruption.

Furthermore, the acceleration and deceleration of asteroid rotation due to YORP can explain the excess of very slow and fast rotators among asteroids with sizes below 10 km diameter (Pravec et al., 2000). The change in rotation period and obliquity can occur on a timescale of 10^8 years and it is possible that the rotation period first descreases and then increases again forming a YORP cycle (Rubincam, 2000). The tilt in obliquity and deceleration of the rotation can also cause an asteroid to tumble (Bottke et al., 2006).

A study by Statler (2009) showed that small-scale topographic feature such as craters can cause the YORP effect to vary by 100 %. This adds a stochastic component to the dynamic of the spin evolution of asteroids, since random events such as moderate-size impacts can alter the YORP effect significantly.

1.2.3 *Thermophysical Properties of Asteroids*

Most thermal infrared observations of asteroids and other small solar system bodies are ground- and space-based, telescopic observations. The NEOWISE survey estimated the diameters of more than 100000 asteroids using infrared data (Masiero et al., 2011). For data analysis they did not use a full thermal model but instead the Near-Earth Asteroid Thermal Model (NEATM) (Harris, 1998) which is a derivative of a standard thermal model (STM). A STM assumes zero thermal inertia and spherical shape of the object, which has then an equilibrium temperature depending on the heliocentric distance and albedo. STMs then introduce a correction factor called the beaming factor that accounts for non-spherical shape, roughness, pole position, and non-zero thermal inertia. While the beaming factor is usually fixed in STMs, the NEATM treats the beaming factor as a free parameter (ibid.). This factor incorporates thermal inertia but cannot not easily be related to it. It is used in infrared, spectral surveys for a large number of asteroids of which little information besides their orbit is available (e.g. Landsman et al. (2016)).

However, for some asteroids full thermal models, such as the one used in this thesis (see section 3.3), are applied to retrieve thermal properties but also pole position, albedo, size and shape. The thermal inertias of mission target asteroids (25143) Itokawa (Hayabusa), (101955) Bennu (Osiris-Rex) and (162173) Ryugu (Hayabusa2) were derived this way and found to be 750 (Müller et al., 2005), 310 $\pm$ 70 (Emery et al., 2014) and 150-300 J m^{-2} K^{-1} s$^{-1/2}$ (Müller et al., 2017) respectively. Estimating asteroid's thermal inertia using a full thermophysical model to fit disk-integrated infrared light curves becomes increasingly common (e.g. Magri et al. (2018), Marshall et al. (2017), and Müller et al. (2013)).

The NASA mission Dawn visited Vesta and Ceres and their thermal inertia was retrieved using the data of the Dawn spacecraft's VIR instrument. Both asteroid surfaces were found to have a low thermal inertia of 30 $\pm$ 10 J m^{-2} K^{-1} s$^{-1/2}$ for Vesta (Capria et al., 2014) and < 50 J m^{-2} K^{-1} s$^{-1/2}$ for Ceres (Formisano et al., 2015). In both cases the surface temperature was retrieved from the spectra using a Bayesian retrieval algorith (Keihm et al., 2012) and thermal inertia was derived by fitting the retrieved temperature with a thermophysical model. ESA's Rosetta spacecraft passed the asteroids (21) Lutetia and (2867) Steins observing their thermal emissivity spectra with the VIRTIS instrument. The infrared spectra were fitted using a full thermal model and taking the 3D shape and heat transfer between parts of the surface into account. The thermal inertia of Lutetia was very low, 20-30 J m^{-2} K^{-1} s$^{-1/2}$ (Coradini et al., 2011), whereas the thermal inertia of Steins was an intermediate 110 $\pm$ 13 J m^{-2} K^{-1} s$^{-1/2}$ (Leyrat et al., 2011). At Rosetta's target comet 67P/Churyumov-Gerasimenko the MIRO micro-wave instrument of the orbiter observed the surface at wavelength from 0.5 to 1.6 mm. The thermal inertia was estimated to be 10 - 50 J m^{-2} K^{-1} s$^{-1/2}$ (Gulkis et al., 2015). Furthermore, the MUPUS radiometer on board the Philae lander performed in-situ infrared observations (Spohn et al., 2015). Due to the cavity-like landing site of the lander the diurnal temperature curve had a very complex shape with a steep increase during direct insolation and a shallower evolution during indirect insolation. The thermal inertia was estimated to be 85 $\pm$ 35 J m^{-2} K^{-1} s$^{-1/2}$.

Currently the Hayabusa2 mission's TIR instrument (Okada et al., 2017) and the Osiris-Rex mission's OTES (Christensen et al., 2018) instrument map the thermal properties of asteroids Ryugu and Bennu, respectively. The global thermal inertia were found to be consistent with disk-integrated, telescopic estimates: 200-500 J m^{-2} K^{-1} s$^{-1/2}$ in the case of Ryugu (Sugita et al., 2019) and 350 $\pm$ 10 J m^{-2} K^{-1} s$^{-1/2}$ in the case of Bennu (DellaGiustina et al., 2019). Additionally, in-situ observation in the thermal infrared range were performed by the MARA instrument of MASCOT lander and results of these observations are discussed in chapter 6.

1.3 ABOUT THIS THESIS

The work presented here was carried out as part of the Hayabusa2 and MASCOT missions to asteroid Ryugu. A thermophysical model was developed to calculate the surface temperature evolution of Ryugu. The calculated temperatures were used to model and analyze the in-situ thermal infrared observation of the MARA instrument on the surface of Ryugu with the goal to derive a conservative estimate of the thermal inertia and subsequently estimating the porosity and thermal conductivity of the bulk material on Ryugu. These properties have implications on the composition of Ryugu, a potential link to types of carbonaceous chondrites, as well as the formation of Ryugu. Furthermore, the thermophysical model was used to study the spatial distribution of thermal forcing on Ryugu's surface. The thesis is divided into six chapters following this introduction.

Chapter 2 introduces the Hayabusa2 mission and its target asteroid Ryugu. Furthermore it provides an overview of the MASCOT lander, as well as a description of the MARA instrument, its calibration, and the data set analyzed in chapter 6. Chapter 3 presents the thermophysical model used in this work, its parameters as well as the parameter retrieval method that was used to derive the thermal inertia.

This work is a cumulative dissertation and three published, peer-reviewed journal articles are included in the thesis. The included manuscripts correspond to the final, submitted versions prior to publication. For this dissertation the figures were re-positioned to correspond to the published, type-set versions of the articles. The references of all three manuscripts are attached to the end of the dissertation together with the references of the other chapters, rather than listed individually.

Chapter 4 was published in 2018 as "A Method to Derive Surface Thermophysical Properties of Asteroid (162173) Ryugu (1999JU3) from In-Situ Surface Brightness Temperature Measurements" in "Planetary and Space Science"[1]. This theoretical work presents the approach on the MARA data analysis, presenting the parameter estimation method, the asteroid thermophysical model and introduces the heat transfer model. I was the first author, wrote the article and implemented the thermal model, the heat transfer model, as well as the parameter estimation algorithm, and performed, analyzed and interpreted all simulations.

Chapter 5 was published in 2019 as "Latitudinal dependence of asteroid regolith formation by thermal fatigue" in "Icarus"[2]. In this study it was investigated how the diurnal temperature range is distributed among the latitudes of a spherical, atmosphereless body. The diurnal temperature range is the main driver of regolith formation by thermal fatigue which leads to crack formation in the regolith as well as fragmentation. Consequently, it reduces the thermal inertia of the regolith over time. This theoretical work contributes to the understanding of the thermal properties and their spatial distri-

1 https://doi.org/10.1016/j.pss.2018.03.017
2 https://doi.org/10.1016/j.icarus.2018.09.033

bution on the surface of Ryugu. I was the first author, wrote the article, analyzed the temperature data calculated by co-author Hiroki Senshu, and interpreted the results.

Chapter 6 was published in 2019 as "Low thermal conductivity boulder with high porosity identified on C-type Asteroid (162173) Ryugu" in "Nature Astronomy"[3]. The study presented the in-situ observations of the MARA instrument and the estimates of thermal inertia, thermal conductivity and porosity derived from it. The temperature evolution of a single boulder was observed by MARA and the thermal inertia of this boulder was found to be surprisingly similar to that of fine sand, indicating a high porosity that might be pristine or the result of thermal fatigue. These results are unprecedented and indicate that most of the meteorite samples available on Earth might be substantially different from the surface material of Ryugu. The first author of this paper is Matthias Grott. My contribution as a co-author included the implementation of a new thermal model, specifically adapted to the MASCOT landing site, the implementation of the illumination model, and the data analysis resulting in the published estimate of the boulder's thermal inertia and its uncertainty. Furthermore, I used the thermal model to investigate and exclude the presence of a potential dust cover on the observed boulder. I retrieved porosity and thermal conductivity from the estimated thermal inertia. Moreover, I contributed the text and figures associated with the above.

The final chapter 7 summarizes the results of the three studies and presents the conclusions of this thesis.

3 https://doi.org/10.1038/s41550-019-0832-x

2

MISSION AND INSTRUMENT

2.1 THE HAYABUSA 2 SAMPLE RETURN MISSION

In December 2014, the Japanese Aerospace Exploration Agency (JAXA) launched the Hayabusa2 spacecraft in a sample return mission to the carbonaceous Near-Earth Asteroid (162173) Ryugu, formerly 1999JU3 (Watanabe et al., 2017). Hayabusa2 is the second Japanese sample return mission after the first Hayabusa mission to asteroid (25143) Itokawa (Kawaguchi et al., 2003). The main goal of the mission is to return a sample of a C-type asteroids to Earth. The returned sample will be studied in depth an compared to carbonaceous chondrites. As mentioned above, C-type asteroids are the most abundant type of asteroids, whereas carbonaceous chondrites are rare. Ryugu has been expected to contain hydrated minerals, organics, and volatiles. The data and samples returned from Hayabusa2 should add to the understanding of the origin and evolution of these materials during planetary accretion and how it is related to the water and organics on Earth (Tsuda et al., 2013; Watanabe et al., 2017). Furthermore, Ryugu belongs to the Apollo group asteroids and crosses Earth's orbit at a minimum intersection distance of approximately 167000 km (Wada et al., 2018) which is less than half the distance between Earth and the Moon. Furthermore, it was the only C-type asteroid reachable by the ion engines of Hayabusa2 and matched all the size and geometry requirement for the planned landing operations (Tsuda et al., 2013). To reach the scientific goals, the Hayabusa2 mission carries four science instruments, two sets of small landers (MINERVA-II1/2) (Watanabe et al., 2017) and the European lander MASCOT (Ho et al., 2017), as well as an impact experiment (SCI, Saiki et al. (2017)) including a detachable camera (DCAM3, Ogawa et al. (2017)). The suit of instruments includes the on-board navigation camera set ONC (Kameda et al., 2017), the laser altimeter LIDAR (Mizuno et al., 2017), Near Infrared spectrometer NIRS3 (Iwata et al., 2017), and the thermal infrared mapper TIR (Okada et al., 2017). The Hayabusa2 spacecraft reached Ryugu in June 2018 and started observation campaigns at various altitudes.

2.2 HAYABUSA2 OBSERVATIONS OF RYUGU

Hayabusa2 revealed that Ryugu has a shape known as "spinning top", similar to asteroid (101955) Bennu. It shows a distinct equatorial ridge indicating that Ryugu once rotated twice as fast as the current rotation period and slowed down due to a currently unknown process (Watanabe et al., 2019). Images of the surface of Ryugu recorded

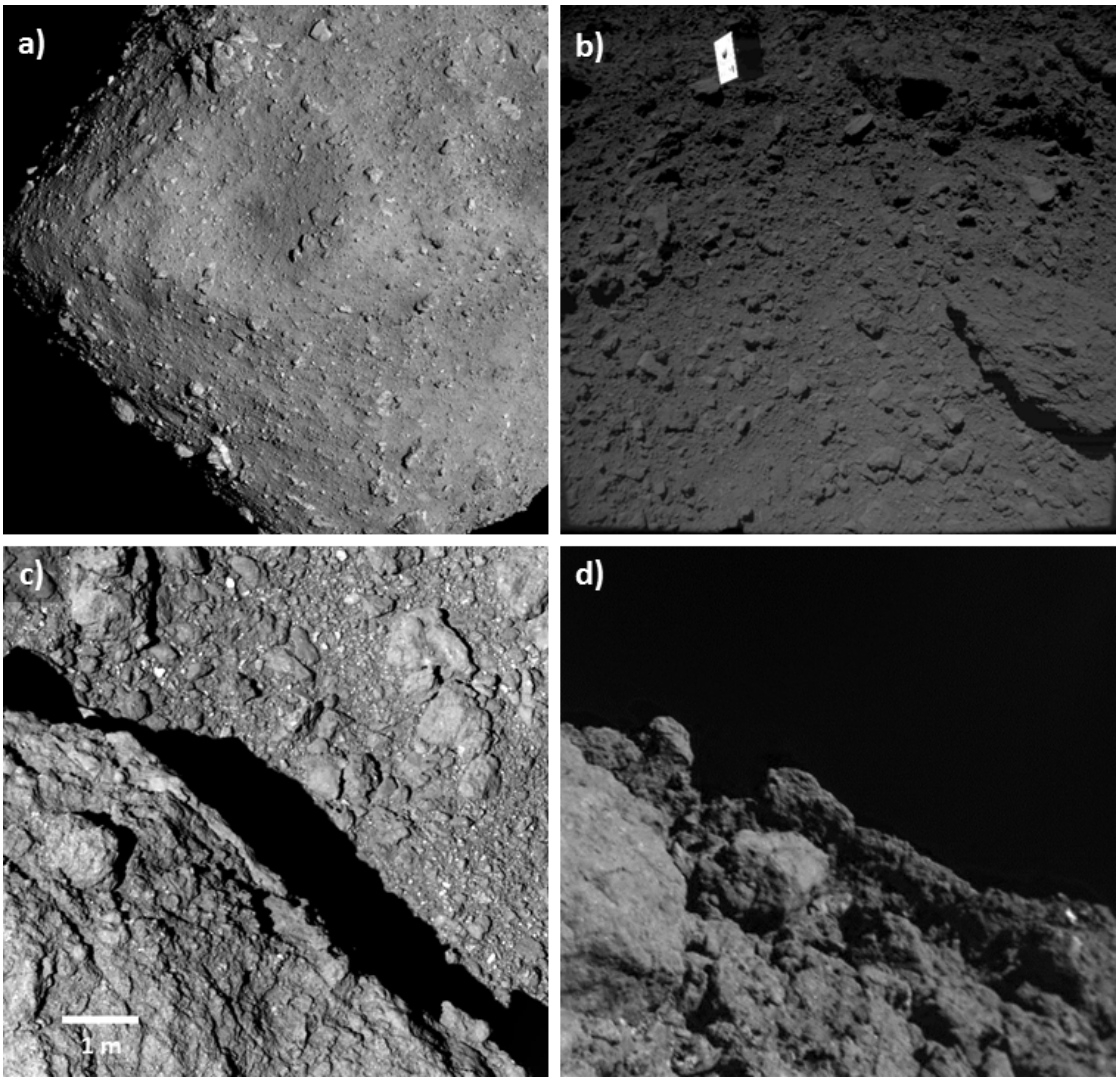

Figure 2.1: a) Image of Ryugu from 6 km altitude, taken with the telescopic ONC-T camera b) Release of the MASCOT lander (upper left) observed with the wideangle ONC-W2 camera at an altitude of less than 60 m, c) Close-up of the surface of Ryugu taken by ONC-T at an altitude of 64 m, d) Image taken by MASCAM on the surface of Ryugu during the descent of the MASCOT lander. Image Credit: a)-c) JAXA, University of Tokyo, Kochi University, Rikkyo University, Nagoya University, Chiba Institute of Technology, Meiji University, University of Aizu, AIST , d) MASCOT, DLR, JAXA

by Hayabusa2 and MASCOT are shown in Fig. 2.1. The images show a surface that is covered by coarse material on all scales. Fine, sand-like regolith is absent. Image a) has been taken from an altitude of 6 km. It shows the equatorial ridge and the large Urashima crater with a diameter of 290 m (Sugita et al., 2019). Image b) was taken during the release operation of MASCOT, which can be seen in the upper left part of the image. It was taken by the wide angle ONC camera from an altitude of less then 60 m. Image c) was taken by the telescopic camera of the ONC system from an altitude of 64 m. It resolves the finer regolith which is revealed to be coarse, decimeter-sized, rough material. It also reveals the similarity between the larger boulder material and the smaller regolith. Image d) was taken on the surface by the MASCAM camera onboard of the MASCOT lander, confirming the impression that the majority of boulders on Ryugu are rough and that fine material is absent.

Using the ONC images and LIDAR measurements a 3D model of Ryugu's shape was constructed. With this and the gravity measurements during descent operations, a bulk density of 1190 $\pm$ 20 kg m^{-3} was derived. It indicates a high overall porosity of at least 50 %, assuming the lowest known grain density for carbonaceous chondrites, i.e. 2420 $\pm$ 60 kg m^{-3} for CI Orgueil (Macke et al., 2011). Such a low bulk density is consistent with Ryugu being a so-called rubble pile asteroid (Watanabe et al., 2019). Rubble-pile asteroids are considered to be loosely bound, reaccreted fragments of catastrophic collisions between parent bodies (Davis et al., 1982; Fujiwara et al., 2006; Sánchez et al., 2012).

Ryugu is now classified as a Cb-type asteroid in the Bus-DeMeo taxonomy system (Watanabe et al., 2019), while formerly estimated to be a Cg (Wada et al., 2018) based on telescopic observations. Ryugu was found to be among the darkest objects in the solar system with a very low geometric albedo of 0.045 $\pm$ 0.002 % at 0.55 µm (Sugita et al., 2019). The NIRS3 instrument found an average reflectance of 0.017 $\pm$ 0.002 at 2 µm (Kitazato et al., 2019). They also found a weak, narrow spectral feature at 2.72 µm across large parts of Ryugu's surface. This indicates the presence of OH groups while the position of the band is consistent with the presence of Magnesium-rich phyllosilicates like Serpentine (ibid.), which are also found in the aqueously altered carbonaceous CI and CM chondrites. However, the authors report that no published meteorite spectrum matches the observation on Ryugu. The low intensity of the feature could be reproduced in laboratory experiments by heating CM2 or CI1 meteorites, which led to dehydration of the samples (ibid.). Consequently Ryugu might have been heated either through shock heating during the destruction of the parent body, partially dehydrated through internal heating of the parent body (Sugita et al., 2019), or heated due the chaotic orbital evolution that might have brought Ryugu very close to the sun (Michel et al., 2010). Another possibility would be a low water-to-rock ratio of Ryugu's parent body during its formation. A possible connection between the spectral Cb-type Ryugu and the CM and CI chondrites might be established by the samples that Hayabusa2 will return.

The ONC camera found the surface of Ryugu to be covered by numerous large

boulders (Sugita et al., 2019). Unlike asteroid (25143) Itokawa (Miyamoto et al., 2007) Ryugu shows no large areas with finer regolith. The boulder density is slightly lower at the equator, which might imply mass movement from the poles towards the equator in agreement with the spinning top shape. Sugita et al. (2019) found four types of boulders: dark rugged boulders, bright smooth ones, bright mottled ones and the unique Otohime Saxum close to the south pole. Dark, rough and brighter, smooth boulders can be seen in the image in Fig. 2.1c and d. The origin of these different boulder populations is not yet clear. A principle component analysis of the color data from ONC supported the results of Kitazato et al. (2019) that the surface material might be similar to heated CI or CM chondrites (Sugita et al., 2019).

2.3 THE MASCOT ASTEROID LANDER

Hayabusa2 carried the small, box-shaped Mobile Asteroid surface SCOut (MASCOT) Lander which was developed in an European collaboration between the German Aerospace Center (Deutsches Zentrum für Luft- und Raumfahrt, DLR) and its French counterpart (Centre national des études spatial, CNES). It is an autonomous lander which weighs 11 kg and has the ability to automatically detect its attitude on the surface, upright itself, and jump to multiple locations on the asteroid (Ho et al., 2017). The mission goal was to provide in-situ measurements of the surface geology composition, magnetization, and thermal properties, and provide a high-resolution ground truth to the measurements taken by the Hayabusa2 spacecraft (ibid.). To carry out its mission MASCOT was equipped with four scientific instruments: a camera MasCam (Jaumann et al., 2017), a magnetometer MasMag (Hercik et al., 2017), an imaging near-infrared spectrometer MicrOmega (Bibring et al., 2017), and the radiometer MARA (Grott et al., 2017), which is in the focus of this thesis.

To bring itself into the correct position for performing the measurements, and to relocate to other parts of the surface, MASCOT was equipped with a mobility mechanism and an attitude control system. The attitude was measured using the Guidance, Navigation, Control (GNC) sensor suite. GNC consisted of two systems with sensors located on the sides of MASCOT. Six Photo-Electric Cell sensors (PEC), one on each side of MASCOT, detected the incident sunlight and from their relative signals the sun vector and MASCOT's attitude relative to the sun could be derived. Furthermore, the Optical Proximity Sensors (OPS) were located on five sides of MASCOT. Each consisted of an infrared light-emitting diode (LED) and a detector. The side of MASCOT facing Ryugu's surface could be determined by measuring the LEDs reflection off the surface (Ho et al., 2017). An eccentric arm inside of MASCOT was accelerated by a motor and generated torque that moved the MASCOT structure. Depending on the applied acceleration, MASCOT could perform a small move, flip, or jump to a new location (ibid.).

During descent MasCam was able to take several images of Ryugu's surface. The

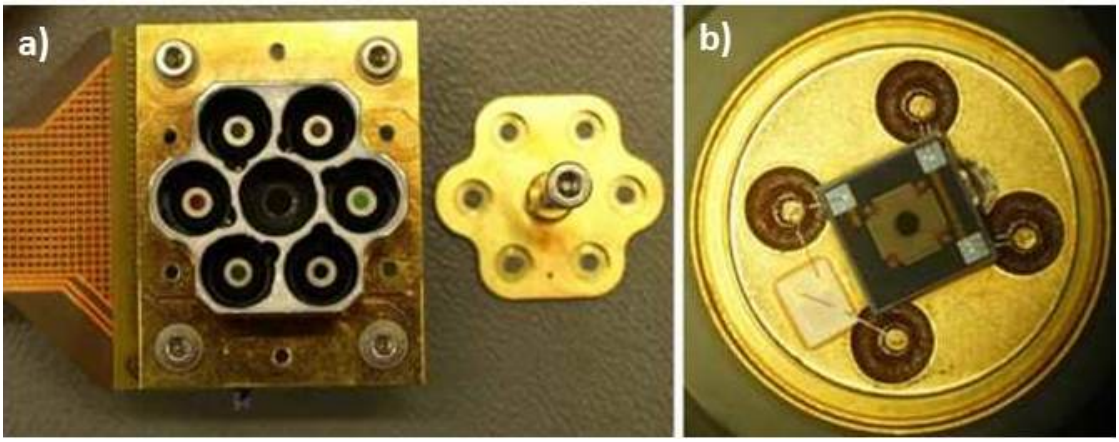

Figure 2.2: a): Photograph of the MARA instrument with the six filters exposed. b): Close-up photograph of one of the six sensors with the sensor housing and filter removed. The black absorber is visible in the center. A PT100 temperature sensor is attached to the lower left part of the sensor, measuring the temperature of the cold junction T_{ref}. Image credit: Adapted by permission of Springer Nature from Space Science Review, Grott et al. (2017)

MasCam team identified two populations of boulders: dark, rugged ones and bright, smooth ones in agreement with the ONC observations (Jaumann et al., 2019). After successfully up-righting itself, MASCOT was able to observe a single 20 - 30 cm sized boulder for a full diurnal cycle. The camera took multiple images under various illumination conditions and with resolution up to 0.15 mm/pixel. The observed boulder belongs to the dark, rugged population reported by Jaumann et al. (2019) and Sugita et al. (2019). Using an LED array MasCam was able to take images at night under red, green, blue and infrared illumination, revealing small inclusions in the dark boulder with variable colors (Jaumann et al., 2019). The MARA instrument was able to measure the full diurnal temperature evolution, which was the first in-situ observation of its kind on an asteroid.

2.4 THE MASCOT RADIOMETER - MARA

This section will provide a brief overview of the MARA instrument, summarizing instrument performance and calibration published by Grott et al. (2017). The MASCOT radiometer MARA measured the thermal flux emitted by an observed surface using six sensors. Each sensor was located behind a filter window, a 8 to 12 µm long-pass, a silicon window transmitting at wavelengths larger than 3 µm and four filters transmitting in narrow bands around 6, 9, 10, and 13 µm. The six filters covered a spectral range that could show characteristic features of chondrites (Reddy et al., 2015). By comparison between the measured fluxes, slopes in the thermal infrared spectrum should be

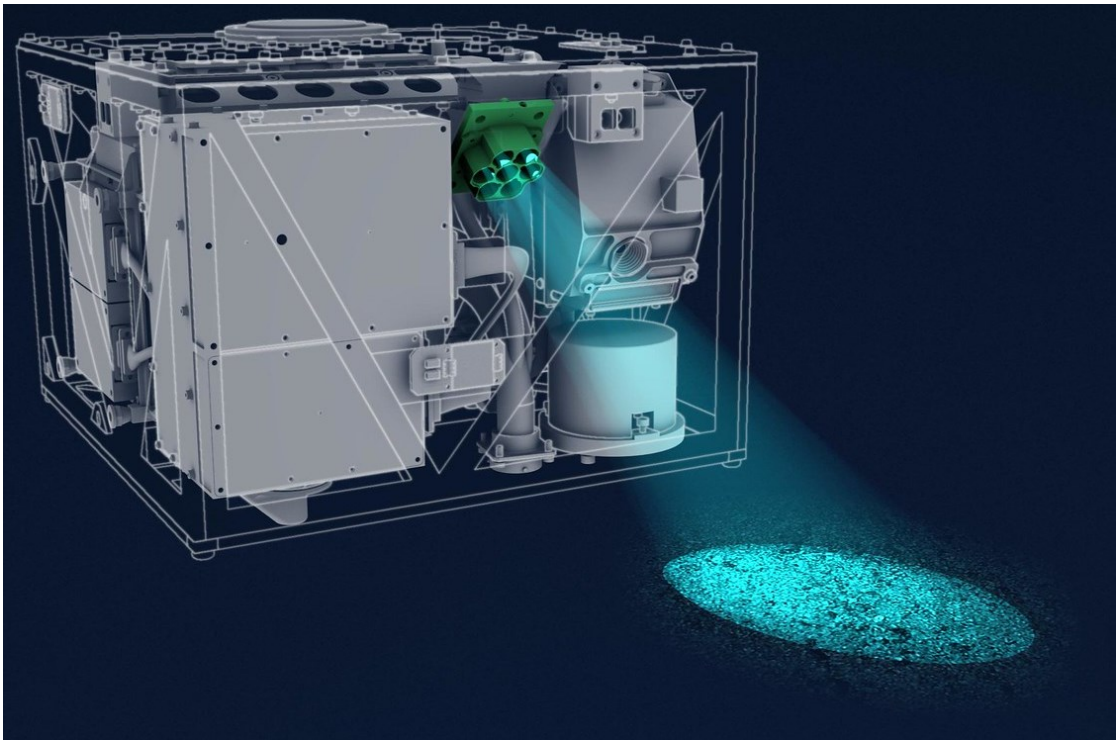

Figure 2.3: Schematics of the MARA instrument within the MASCOT lander. The field of view of MARA is illustrated. It lies within the field of view of the camera. Image credit: DLR

observable, which might help to constrain the composition of the surface material. Each sensor consisted of an absorber that heated or cooled depending on the received heat flux and was connected to a stack of 72 thermocouples. Due to the Seebeck effect the thermocouples generated a signal voltage proportional to the temperature difference between the absorber and the cold junction whose temperature T_{ref} was measured with a PT100 sensor. The Seebeck coefficient of the thermocouples was 135 $\mu V\,K^{-1}$ each. Fig. 2.2a shows an image of MARA with the aperture cover removed, exposing the six filters. Fig. 2.2b shows a close up of one of the sensors with its housing removed. In this image one can see the black absorber in the center and the PT100 sensor which measures T_{ref} in the lower left. Fig. 2.3 shows the position of the MARA instrument (green) within the instrument compartment of MASCOT. The MARA field of view (bright blue) is also shown in the image. It overlapped with the field of view of MasCam such that MasCam images provided important context information to the MARA measurement.

The net heat flux Q_{tot} determining the temperature of the absorber had two sources that could be calculated according to equation 3.15, which is derived in section 3.2 below. One source was the net heat flux exchanged with the observed surface outside

the sensor Q_s and the other source was the net heat flux exchanged within the sensor housing Q_H:

$$Q_s = a_d \pi F_s \int d\lambda \tau(\lambda)[B(T_{ref}, \lambda) - \varepsilon B(T_s, \lambda)]$$

$$Q_H = a_d \pi F_H \int d\lambda [B(T_{ref}, \lambda) - B(T_H, \lambda)] \tag{2.1}$$

$$Q_{tot} = Q_s + Q_H$$

Where a_d is the area of the absorber, ε is the surface emissivity as defined in equation 3.7, F_s is the view factor from the absorber to the target surface, F_H is the view factor from the absorber to the sensor housing, T_s is the temperature of the target surface, and T_H the temperature of the sensor housing. The Planck function $B(T, \lambda)$ is defined in equation 3.1 and view factors are defined in equation 3.9. All heat exchange between absorber and asteroid surface passed the sensor filters, and Fig. 2.4 (left) shows the throughput of the six MARA channels $\tau(\lambda)$, i.e. the combination of transmissivity of the filter window and the absorption of the absorber, as a function of wavelength. The view factor F_s was measured during the geometric calibration, where MARA was placed in conjunction with a collimated blackbody source at a temperature of 1000 K. MARA was then tilted in horizontal and vertical direction and the change in signal voltage was registered. As the tilt angle surpassed the opening angle of the filter aperture the signal decreased and the opening angle of the field of view , $\theta_M = 20°$, was determined as angle where the signal dropped below 10 % of the maximum. The view factor F_s could then be calculated by

$$F_s = \frac{1}{2}(1 - \cos\theta_M) \approx 0.03 \tag{2.2}$$

In an ideal measurement, the only heat exchange occurs between absorber and the target surface, i.e. $Q_H = 0$ and $Q_{tot} = Q_s$. For this, the temperature of the housing needs to be at the same temperature as the absorber. Already a small temperature differences can cause a significant heat transfer between absorber and housing, which would result in an additional, unwanted signal. To avoid this, the temperature of the housing was regulated by a heater assuring that $T_H \approx T_{ref}$.

The signal voltage was approximately proportional to the net heat flux on the absorber and a function of the sensor sensitivity S which has the units of $\mathrm{V\,W^{-1}}$:

$$U \approx S\, Q_s \tag{2.3}$$

The radiometric calibration of MARA determined the sensitivity S as described by Grott et al. (2017). MARA was placed in a space simulation chamber at vacuum conditions with pressures around 10^{-5} bar. For the calibration a cavity blackbody with emissivity of 0.999 was used. With the temperature of the blackbody known, Q_s could be calculated. The calibration was performed for three operation setpoints were the temperature of the MARA instrument was set to: 273, 298, and 323 K. The temperature of the black body was varied from 123 to 373 K.

Small residual temperature differences between the sensor and its housing which caused $Q_H > 0$ were also accounted for in the calibration of the instrument (ibid.). Here, the calibration target temperature and the temperature of MARA were held constant at 298 K and the temperature of the surrounding vacuum chamber was reduced. To compensate the heat loss to the increasingly cold environment, the heating power P_q stabilizing the sensor temperature increased. As the small temperature differences within the housing depend slightly on the balance between environment temperature and P_q, a heating power dependent offset in the signal voltage ΔU could be observed (ibid.). The effect was parametrized by a sensitivity correction S_q:

$$S_q(P_q) = \frac{\partial \Delta U}{\partial P_q} \tag{2.4}$$

Further, non-linear responses of the sensor to the net heat flux Q_s were included in the calibration by introducing the parameters S_1 and S_2 and the three sensitivity parameters S, S_1, and S_2 were calculated by fitting the signal voltages U observed during calibration as a function of blackbody temperature T_{BB}, heating power P_q, and cold junction temperature T_{ref} (ibid.):

$$U - S_q(P_q)P_q = SQ_s(T_{BB}, T_{ref}) + S_2Q_s(T_{BB}, T_{ref})^2 + S_1 \tag{2.5}$$

The raw signal voltage of all six sensors measured during MASCOT mission covering descent and on-asteroid operation is plotted in Fig. 2.5 as a function of time. The first part, tagged SDL for Separation, Descent, Landing, consisted of three short phases. The relative flat signal represents the temperature of the Hayabusa2 spacecraft as observed by MARA when MASCOT was still attached to Hayabusa2. After 1:57 Coordinated Universal Time (UTC) one sees a rapid sequence of large signal changes when MASCOT descended towards the surface of Ryugu rotating and repeatedly observing deep space and the surface of Ryugu. At 2:25 UTC, after tumbling over the surface, MASCOT came to rest on its top side and MARA pointed towards space. The autonomous up-righting failed and MASCOT remained in this position throughout the asteroid night. This phase is tagged as "Deep Space" in Fig. 2.5 and extends from 2:25 to 7:53 UTC. The large peak in signal in the beginning of that phase shows the heating of MARA by direct illumination. As described above, small temperature variations

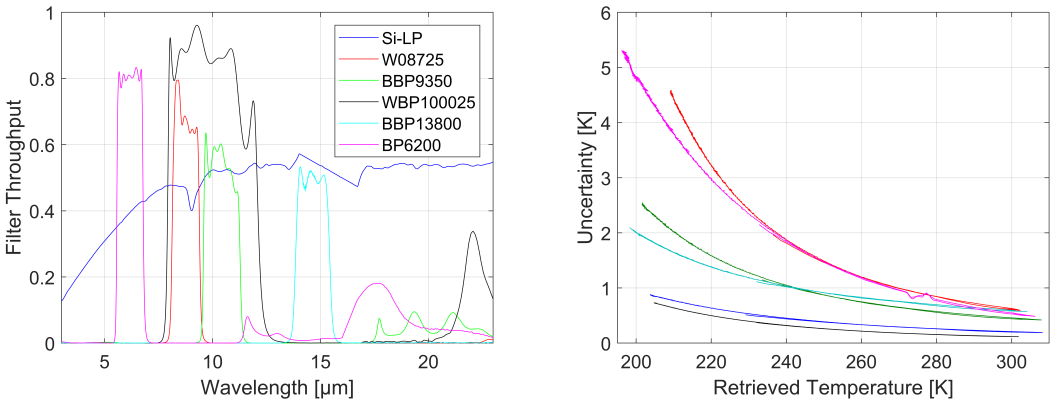

Figure 2.4: Left: Throughput of the six MARA channels as a function of wavelength, with the filter designation listed in the legend. Right: The 1σ uncertainty estimate as function of retrieved temperature for the six MARA sensors.

within the sensor housing can cause a large signal. The direct illumination was beyond the capability of the MARA temperature control system and resulted in a significant temperature gradient within the MARA sensor housing. Due to constraints on the Hayabusa2 operations no commands could be send to MASCOT in that phase. A forced up-righting was commanded as soon as Hayabusa2 established contact with MASCOT. This up-righting was successful and finished just in time before the local sunrise. MARA was able to observe a full diurnal cycle from 7:53 to 15:30 UTC, highlighted by a red box in Fig 2.5. After performing a small move for stereo images at 15:30 UTC , a second sunrise was observed at 15:37 UTC, with the change in field of view resulting in a slightly altered signal. Another local noon and afternoon were observed until 18:00 UTC when a relocation jump was performed by MASCOT. Then MARA could only observe deep space again from 18:49 until 19:03 UTC when the battery of MASCOT ran out.

The radiometric calibration was reviewed regularly during flight and slight changes were found compared to the ground calibration. The final re-calibration of the instrument included the in-flight re-calibrations and made use of the deep-space observation which was essentially an observation of a perfect blackbody with almost 0 K temperature. The sensitivities calculated in this recalibration included uncertainties such as small inhomogeneity in the on-board blackbody, or the uncertainty of the PT100 sensors. The uncertainty of sensitivity estimates of the different calibrations was included into the uncertainty of the measured temperature via Monte-Carlo methods. In the 8-12 µm (denoted WBP10025) band and the silicon longpass the resulting 1σ uncertainty was below 1 K over the observed temperature range. In the narrow bands it was slightly larger during day and much larger during night. The instrument noise was below 0.1 K,

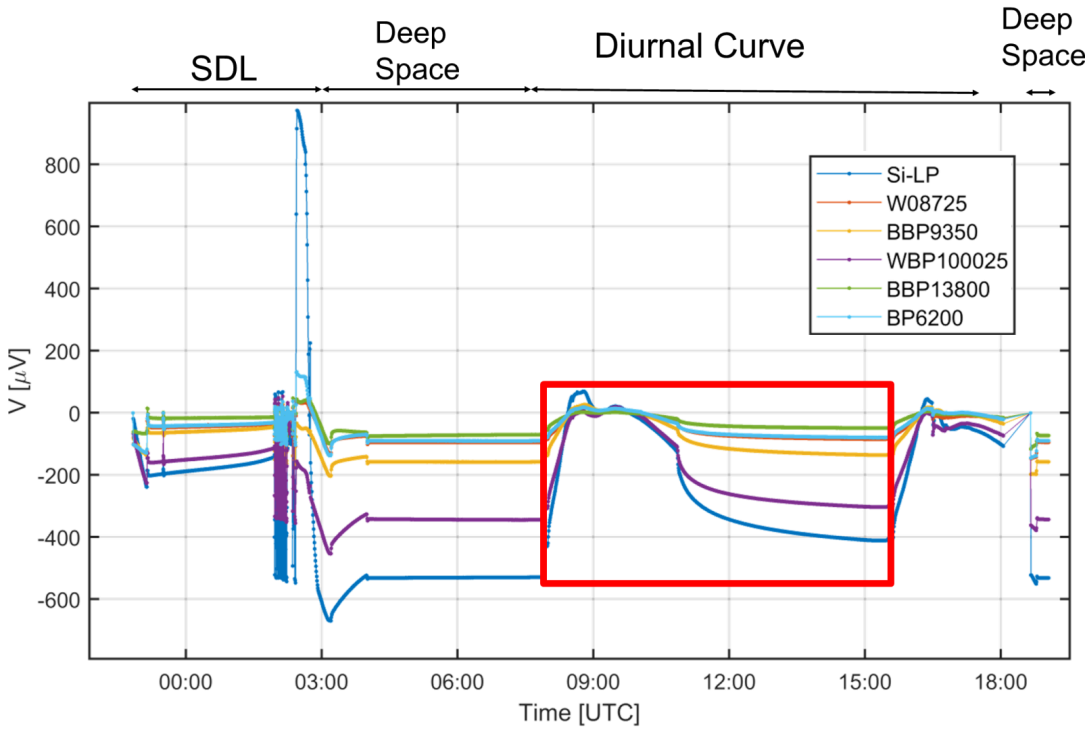

Figure 2.5: Raw signal voltage of the MARA instrument as function of time during descent and on-asteroid operation. The red box indicates the part of the dataset used for analysis in this work.

and did not contribute significantly to the overall uncertainty. Fig. 2.4 (right) shows the estimated uncertainty as a function of the corresponding temperature estimates for all six sensors, under the assumption that the emissivity of the surface is unity. The 8-12 µm filter showed the lowest temperature uncertainty and was used for the analysis of the MARA observations.

3

THEORY AND MODEL

3.1 THERMAL RADIATION

In this thesis, information about the structural properties of asteroid Ryugu's surface material is derived from thermal infrared observation. This chapter provides an overview of the fundamental concepts of this method. The basic principles of thermal radiation and heat transfer are discussed as well as the thermophysical model, thermophysical properties, parameter estimation, and roughness effects.

Every physical body with a defined temperature constantly emits electromagnetic radiation. For an ideal blackbody this radiation obeys Planck's law

$$B(\lambda, T) = \frac{2hc^2}{\lambda^5} \frac{1}{e^{\frac{hc}{\lambda k_B T}} - 1} \tag{3.1}$$

which defines the Planck function $B(\lambda, T)$, with wavelength λ, Planck constant h, speed of light c, Boltzmann constant k_B, and temperature T. Planck's law describes the spectral radiance of an object which is defined as the energy emitted per area, solid angle, and wavelength. Fig. 3.1 shows the spectral radiance of three blackbodies as function of wavelength at different temperatures. The spectral radiance increases strongly with temperature. Furthermore, the maximum of the Planck function shifts towards shorter wavelength with increasing temperatures following Wien's displacement law, given by

$$\lambda_{max} = \frac{b}{T} \tag{3.2}$$

where b is the Wien's displacement constant and $b \approx 2898$ µm K. The temperatures of the Planck functions shown in Fig. 3.1 vary from 223 K to 323 K, which is similar to the temperatures expected on asteroid Ryugu. The emission maxima lie within 9 to 12 µm which is the spectral range of the long-band W10 filter of the MARA instrument.

The radiosity, also called exitance, of a black body J_{BB} is the emitted flux per area and is calculated by integrating equation 3.1 over wavelength and the solid angle

$$J_{BB} = \iint B(\lambda, T) \cos\theta_e d\Omega d\lambda \tag{3.3}$$

where Ω is the solid angle over the emitting surface and θ_e the emittance angle, which is zero for perpendicular emission. The cosine enters the equation as an ideal blackbody is a Lambertian surface.

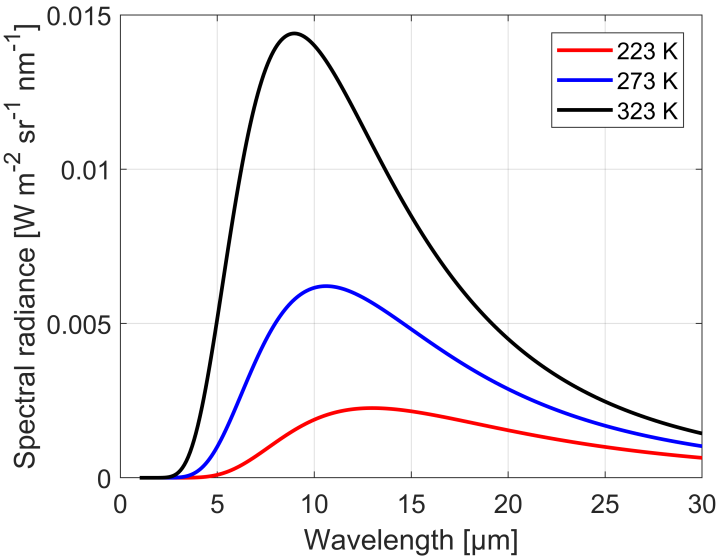

Figure 3.1: The spectral radiance of blackbodies with temperatures indicated in the legend, as a function of wavelength. The spectral radiance follows Planck's law and is described by the Planck function. The maxima shift towards shorter wavelength with increasing temperatures and lie within the transmission range of the MARA filters

A Lambertian surface is defined by its radiance being independent of the emitting direction, where radiance is defined as the flux emitted per solid angle and projected area. Such a Lambertian surface is an ideal, isotropic emitter and an ideal diffuse reflector. The radiosity of the surface follows Lambert's cosine law given by

$$J = J_0 \cos\theta_e \tag{3.4}$$

where J_0 is the maximum radiosity for perpendicular emission. A thought experiment can motivate the cosine dependence in Lambert's law: Given a part of an infinite Lambertian surface with area a observed through a fixed solid angle Ω_f the flux passing through that solid angle is defined as Q_f. If the surface is tilted the projected surface observed under the fixed window of solid angle will be $a_t = a\cos\theta_e$, where θ_e is the angle of the tilt. Here, the surface will be tilted until it is perpendicular to the observer. Since the observed surface is Lambertian it should emit isotropically, i.e. the flux Q_f has to be independent of the observation angle. Through the definition of the radiosity as $J = dQ_f/da$ one arrives at the following condition:

$$\begin{aligned} a_t J_0 &= aJ \\ J &= J_0 \cos\theta_e \end{aligned} \tag{3.5}$$

This property significantly facilitates radiometric calculations and a Lambertian surface is a commonly used model for emitting surfaces.

Integrating equation 3.3 over the full solid angle results in the Stefan-Boltzmann law given by

$$J_{BB} = \sigma_B T^4 \tag{3.6}$$

where $\sigma_B = 5.670373\ 10^{-8}\,\mathrm{W\,m^{-2}\,K^{-4}}$ is the Stefan-Boltzmann constant. Thermal emission from real surfaces differs from that of a blackbody. On the one hand, the spectral radiance generally differs from Planck's law (equation 3.1), according to the spectral properties of the material. On the other hand, a surface usually exhibits some degree of roughness and its emission differs from the one of a Lambertian surface. The spectral deviation from a blackbody is briefly discussed in the following, the effect of roughness is described in section 3.5.

The emissivity ε of a surface is the ratio between its emitted power and the power an ideal blackbody would emit at the same temperature.

$$\begin{aligned} J &= \int\int \varepsilon(\lambda) B(\lambda, T) \cos\theta_e d\Omega d\lambda \\ &= \varepsilon J_{BB} \\ &= \varepsilon \sigma_B T^4 \end{aligned} \tag{3.7}$$

It governs the energy loss of the body through radiative heat transfer, which decreases with lower emissivity. If the temperature of a surface is derived by measuring the emitted flux of the surface and assuming $\varepsilon = 1$, it is called the brightness temperature T_b, i.e. the temperature an ideal blackbody would have when emitting the observed flux.

$$T_b = \left(\frac{J}{\sigma_B}\right)^{1/4} \tag{3.8}$$

Generally, the emissivity depends on the wavelength and for most geologic materials the fundamental vibrations in the crystal structure occur at frequencies in the mid-infrared range (5 - 30 µm) resulting in characteristic spectral features, which was used to identify minerals and rocks in numerous studies over the past decades (e.g. Christensen et al., 2000; Christensen et al., 2001; Cross et al., 1955; Emery et al., 2006; Hunt et al., 1974; Lyon, 1965; Maturilli et al., 2008; Salisbury et al., 1991).

A prominent spectral feature is the Christiansen peak. It is the emissivity maximum (i.e. the reflectance minimum) of a material with multiple microstructure phases and occurs at those wavelength where the refractive indices of the microstructure phases match. For most silicates it lies in the 7.5 - 10 µm range (Reddy et al., 2015). Further

diagnostic features can be located at longer wavelengths. For example, in meteorites the features of Olivine and Pyroxite dominate in a between 8.5 - 12 µm (e.g. Salisbury et al. (1991)). Furthermore, the O-H bond stretching in hydrated phyllosilicates shows typical features around 3 µm and is often found primitive carbonaceous chondrites (e.g. Salisbury et al., 1974; Takir et al., 2012).

3.2 RADIATIVE HEAT TRANSFER MODEL

Surfaces of objects facing each other exchange heat through emission and absorption of electromagnetic radiation. The view factor F_{ij} describes the ratio between the radiation surface j receives from surface i and the total amount of radiation emitted by surface i (McCluney, 1994) and is defined by

$$F_{ij} = \frac{\int_{a_i} \int_{a_j} \cos\vartheta_i \cos\vartheta_j da_i da_j}{\pi a_i R^2} \tag{3.9}$$

where a_i the area of the emitting surface, a_j the area of the receiving surface, R the distance between the two surfaces, ϑ_i and ϑ_j the angles between the ray connecting the two surface centers and the normal vectors of surface i and j respectively. Using the limit of small surface elements and long distances, i.e. $1 \gg da/R^2$, equation 3.9 can be simplified to the commonly used expression (Davidsson et al., 2014):

$$F_{ij} = \frac{\cos\vartheta_i \cos\vartheta_j a_j}{\pi R^2} \tag{3.10}$$

The view factors F_{ij} and F_{ji} are related through the ratio of the areas of the surfaces i and j, such that

$$a_i F_{ij} = a_j F_{ji} \tag{3.11}$$

One method to calculate the heat transfer between surfaces is the net radiation method (Howell et al., 2016), which is described in more detail in section 4.2.2. This method is used here to estimate the net heat flux received by MARA, given a modeled asteroid surface temperature. While this method was developed to calculate heat transfer within an enclosure, it can be applied to the measurement situation on Ryugu by treating the sky as a perfect black body with 0 K temperature.

The spectral radiosity of a surface i is the sum of the emitted radiation and the reflected radiation received from other surfaces, given by

$$J_i(\lambda) = \pi\varepsilon_i B(T_i, \lambda) + (1 - \varepsilon_i) \sum_{j \neq i}^{N} F_{ij} \tau_{ij}(\lambda) J_j(\lambda) \tag{3.12}$$

where ε_i is the emissivity of surface i, $J_j(\lambda)$ the spectral radiosity of surface j, and T_i the temperature of surface i. The factor π is the result of the integration over the solid angle and the cosine of the emission angle, corresponding to Lambert's law. The factor τ_{ij} is 1 unless the radiation passes through a absorptive medium, e.g. one of the filters of the MARA instrument. In this case it is equal to the throughput of the medium. Equation 3.12 results is a set of coupled linear equations. With the solutions for the spectral radiosities $J_i(\lambda)$ one can then calculate the net heat flux for a given surface Q_i

$$Q_i = a_i \pi \int d\lambda \sum_{j \neq i}^{N} F_{ij} \tau_{ij} [J_i(\lambda) - J_j(\lambda)] \tag{3.13}$$

where N is the total number of surfaces. In the simple case of MARA observing a spot with area a_2 on a flat, infinitely large surface, three surfaces exchange heat: the MARA detector (1), the observed surface spot (2), and space (3). The emissivities of the MARA detector and space are assumed to be unity, and since the detector area a_1 is very small compared to the area of the observed surface spot $F_{21} = 0$. Furthermore, we assume that MARA observes only the surface and not deep space, such that $F_{13} = 0$. The radiosities of the three surfaces are then given by

$$\begin{aligned} J_1 &= \pi B(T_1, \lambda) \\ J_2 &= \pi \varepsilon_2 B(T_2, \lambda) \\ J_3 &= 0 \end{aligned} \tag{3.14}$$

Therefore, the net heat flux on the MARA detector is given by

$$Q_1 = a_1 \pi F_{12} \int d\lambda \tau(\lambda) [B(T_1, \lambda) - \varepsilon_2 B(T_2, \lambda)] \tag{3.15}$$

where F_{12} is the field of view of the MARA instrument which was defined in the geometric calibration of the instrument and given in equation 2.2. As the temperature T_1 of the MARA sensor is known from an independent measurement, the temperature of the surface can be estimated from the received flux depending on the assumed surface emissivity ε_2.

3.3 ASTEROID SURFACE THERMOPHYSICAL MODEL

The asteroid surface thermophysical model calculates the temperature evolution of a surface as function of parameters like thermal inertia and emissivity. By variation of these parameters and comparison of the calculated temperatures to observed ones it is possible to estimate the thermophysical properties of the surface material, in particular its thermal inertia.

The temperature evolution of the surface on an asteroid is modeled by solving the one-dimensional heat conduction equation

$$\frac{\partial}{\partial t} c_p(T)\rho(z,T)T(z,t) = \nabla(k(z,T)\nabla T(t,z)) \tag{3.16}$$

where c_p is the heat capacity of the surface material, ρ density, t time, k thermal conductivity, T temperature, and z depth. Equation 3.16 is a second order partial differential equation, which requires two boundary conditions to be defined. At the lower boundary the flux is set to zero, assuming there is no internal heat source and thus no heat flow from inside of the object. The upper boundary condition accounts for interaction of the surface with its environment and is the balance of the heat conduction into the surface, heat radiated by the surface, energy input by insolation, and thermal radiation received from other parts of the asteroid surface.

$$\sigma_B \varepsilon T^4 = (1-A)I + k(0,T)\left.\frac{\partial T}{\partial z}\right|_{z=0} + P_{th} \tag{3.17}$$

where A is bond albedo, I is insolation, and P_{th} is the power of thermal radiation received from the surrounding terrain.

While k, c_p, and ρ are generally functions of temperature and depth, many models neglect these dependencies. In this case, the asteroid surface is represented by a homogenous half-space and the structure of the surface regolith, i.e. grain contacts, pores, etc. is not explicitly modeled but parametrized by constant k, c_p, and ρ representing regolith properties that are averaged over the modeled depth. The thermal evolution of the surface can then be described with a single material parameter, the thermal inertia Γ, which was defined in equation 1.1.

The thermal inertia is motivated by normalizing the spatial variable z to one diurnal skin depth d, which is the depth at which the amplitude of the temperature wave propagating into the surface is attenuated to $1/e$. It is given by

$$d = \sqrt{\frac{k}{\rho c_p}\frac{P}{\pi}} = \sqrt{\kappa \frac{P}{\pi}} \tag{3.18}$$

where $P = 7.6326$ h is the rotation period in case of Ryugu, and κ the thermal diffusivity. When expressing the upper boundary condition in terms of $z' = z/d$, the only remaining material parameter determining the surface temperature is Γ:

$$\sigma \varepsilon T^4 = (1-A)I + \Gamma\sqrt{\frac{\pi}{P}}\left.\frac{\partial T}{\partial z'}\right|_{z'=0} + P_{th} \tag{3.19}$$

However, it should be noted that Γ is only a physically meaningful parameter at the surface, whereas the diffusivity determines the subsurface temperatures. The

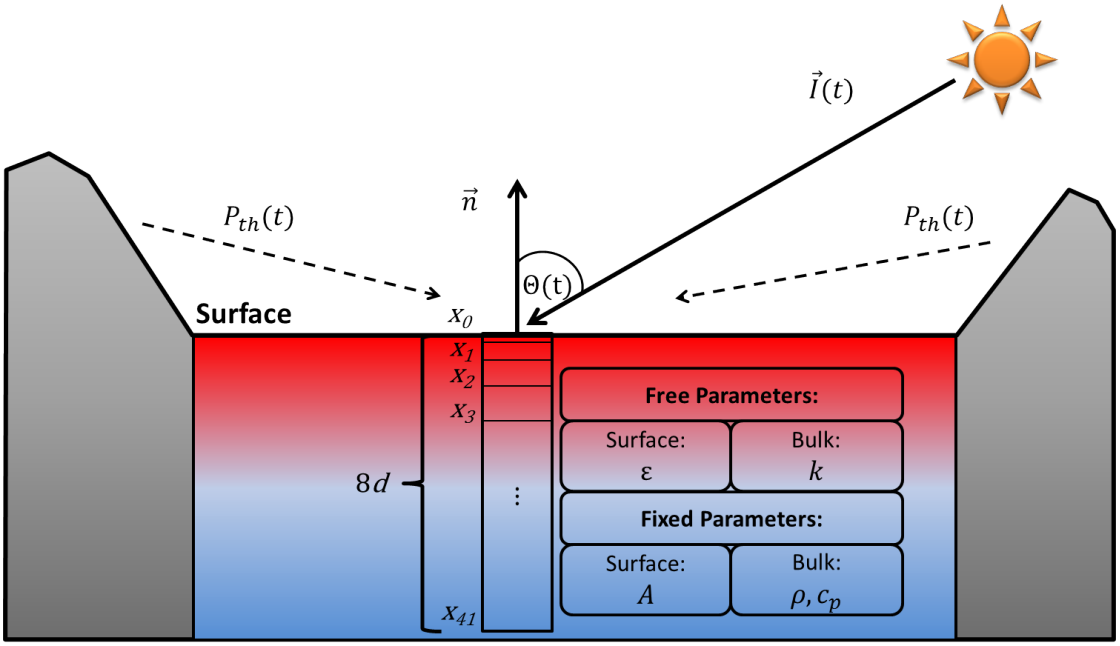

Figure 3.2: Illustration of the thermophysical model with the surface orientation $\vec{n}$, time dependent solar incident angle $\theta(t)$, sun vector $\vec{I}(t)$, and thermal radiation from the environment $P_{th}(t)$. The grid on which the temperatures are calculated is represented by x_0 to x_{41} and has a total length of eight diurnal skin depth d. While thermal conductivity k and emissivity ε are varied for each surface orientation model, the bond albedo A, heat capacity c_p and density ρ are fixed.

assumption of constant k, c_p, and ρ is very common and Γ is a standard parameter used to describe the thermal behavior of surfaces in the planetary science, and examples of such studies were given in section 1.2.

In this work we use a commercial NAG library solver to solve the 1D-heat conduction equation in equation 3.16 using the discussed boundary conditions. The solver employs the Method of Lines to discretize the spatial variables. This results in a set of differential equation at each spatial grid point. The time direction is solved using Gear's implementation of backward differentiation formulas (Gear, 1971). These formulas are higher order, and more stable, generalizations of the backward Euler method. The higher the order, the more of the past time steps are included in the calculation of the next time step. Details of how the NAG solvers implement the Method of Lines and Gear's method are given by Dew et al. (1981).

The spatial grid is defined by 41 grid points of increasing distance, i.e. a given spatial interval between two grid points is 1.2 times larger than the previous one. The grid has a total length of eight diurnal skin depth d to ensure that the diurnal temperature wave is sufficiently attenuated to justify the lower boundary condition where the flux is zero.

The illumination I ultimately drives the temperature evolution on asteroids. It is given by

$$I = \begin{cases} \frac{I_0}{r_h^2} v \cos\theta_I & \text{if } \cos\theta_I \geq 0 \\ 0 & \text{if } \cos\theta_I < 0 \end{cases} \tag{3.20}$$

where $I_0 = 1366.1 \mathrm{W/m^2}$ is the solar constant at 1 astronomical unit (AU), and r_h the heliocentric distance in units of AU. The visibility flag v indicates whether or not the sunlight is block by the topography, with $v = 0$ representing shadowing of the modelled spot by topographic features. The incident angle θ_I is derived from the scalar product between surface normal vector $\vec{n}$ and the normalized solar incident vector $\vec{s}$:

$$\cos\theta_I = \vec{n} \cdot \vec{s} \tag{3.21}$$

For a sphere, $\cos\theta_I$ can be calculated analytically and is given by

$$\cos\theta_I = \cos\phi \cos\delta \cos\psi(t) + \sin\phi \sin\delta \tag{3.22}$$

where δ is solar declination, and ϕ is latitude with $\phi = 0$ at the equator. The local hour angle $\psi(t) = \omega t$ changes with time as the asteroid rotates with frequency ω and noon is defined by $\psi(t = 0) = 0$. On a sphere thermal radiation from the surrounding $P_{th} = 0$ and $v = 1$ for all surface points. The studies presented in chapter 4 and 5 assume a spherical shape of the asteroid. An illustration of the thermophysical model and its parameter is shown in Fig. 3.2.

Generally, the topography of a surface will influence its thermal evolution. On the one hand, topographic features can block sunlight which can shift sunrise and sunset or cast shadows during the day. On the other hand, thermal radiation P_{th} will be exchanged within the topography which needs to be included into the radiative balance in the upper boundary condition.

The topography is usually approximated by digital terrain models (DTM). These models consist of a mesh of triangular facets. The shadowing effects of the topography are modeled by calculating whether the ray between the center of a given facet towards the sun is passing through any other facet of the shape model. Then, the visibility factor v is calculated for each facet of the DTM for any given time step.

A thermal model for the global shape was calculated for the MASCOT landing site selection. Here the calculated temperatures were used to choose a landing site where the MASCOT lander would still be able to operate. The surface temperature needed to be high enough to ensure sufficient power supply through the MASCOT battery. However, at the same time the temperatures needed to be sufficiently low to ensure a low thermal noise of the MASCOT instruments. Fig. 3.3 shows one of the models calculated for the landing site selection, with an assumed uniform thermal inertia

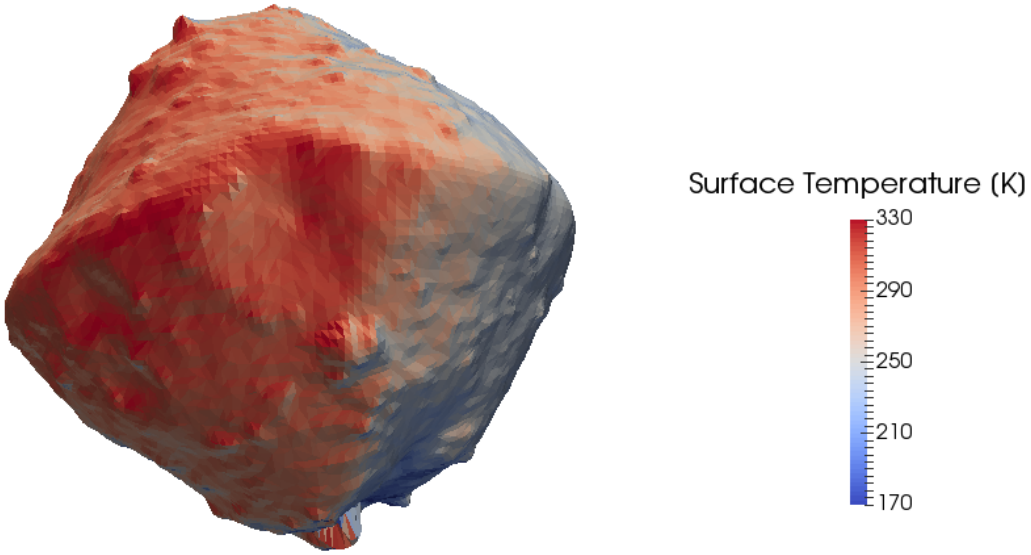

Figure 3.3: Snapshot of the thermal evolution of Ryugu's surface as calculated for the landing site selection for an assumed uniform thermal inertia of 250 $\mathrm{Jm^{-2}K^{-1}s^{-1/2}}$ and a 25000 facet shape model.

of 250 $\mathrm{Jm^{-2}K^{-1}s^{-1/2}}$. In that implementation the radiation exchanged between the facets of the shape model were ignored for the sake of simplicity. Fig. 3.4 shows the maximum and minimum temperatures of the same simulation as a function of latitude and longitude.

For the analysis of the MARA data in chapter 6 the thermal radiation from the environment was taken into account. However, the surface orientation of the target spot was poorly constrained, such that $\vec{n}$ was a free parameter in the thermal model. The thermal radiation exchanged within the topography could in principle be included in the TPM using the net radiation heat transfer method described above. However, such a calculation required large computational resources and since each possible surface orientation would result in a different heat transfer setup, a self consistent model was unfeasible. Instead, P_{th} was estimated assuming that the temperatures of the surrounding topography were in average similar to the temperatures observed by MARA, which was justified as the Hayabusa2 orbiter's infrared camera TIR observed very homogeneous surface temperatures on Ryugu. To estimate the amount of thermal re-radiation that each facet i in local landing site DTM receives from the all N sur-

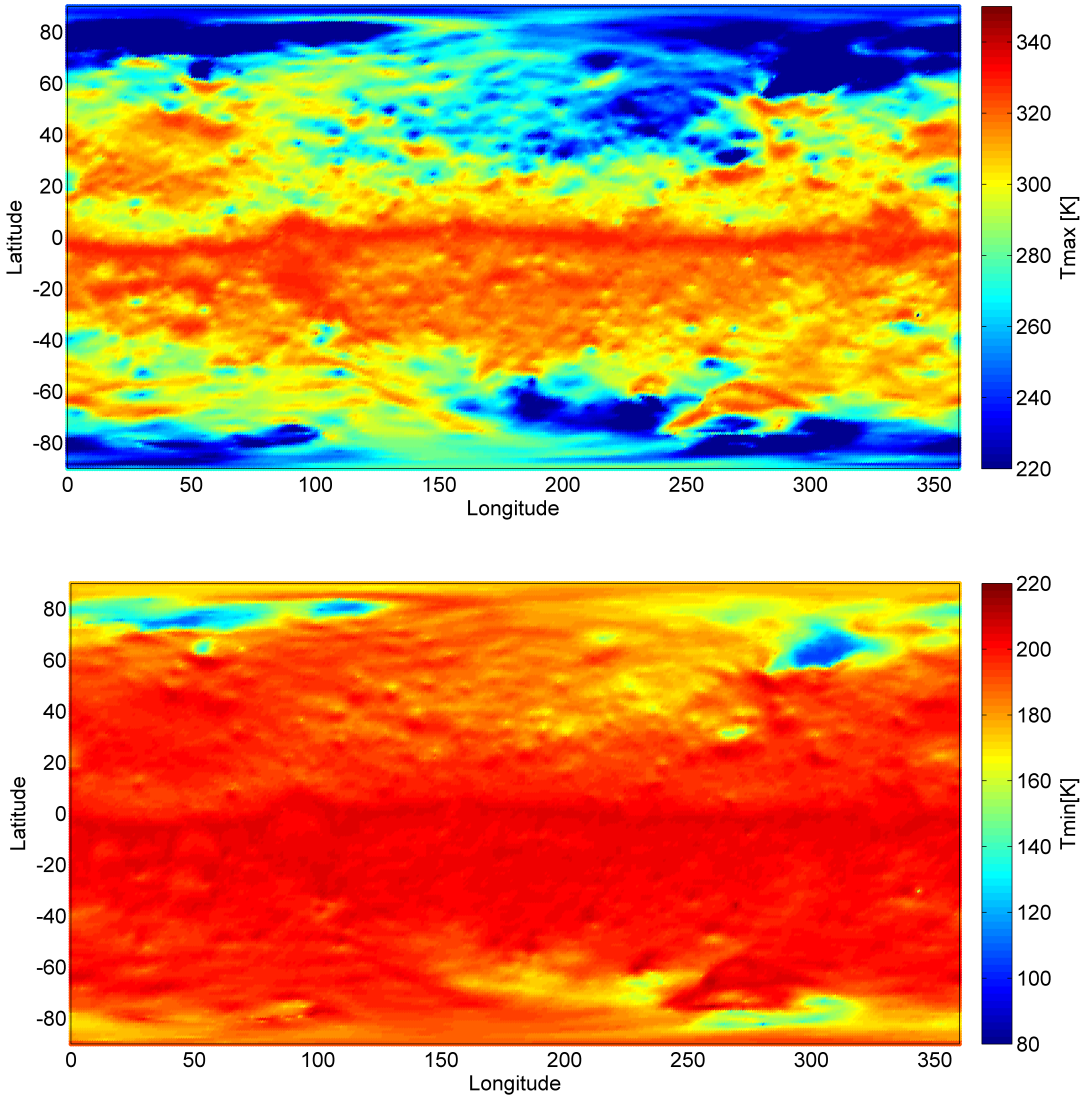

Figure 3.4: Top: Maximum diurnal temperature of the thermal evolution of Ryugu's surface as a function of latitude and longitude, calculated for the landing site selection assuming uniform thermal inertia of 250 $Jm^{-2}K^{-1}s^{-1/2}$ and a 25000 facet shape model. Bottom: Minimum diurnal temperatures as a function of latitude and longitude for the same simulation

rounding facets j, the integrated view factors f_i of the facets i were calculated according to

$$f_i = \sum_{j=1}^{N} F_{ij} \tag{3.23}$$

It was found that the DTM facets near the MASCOT landing site had a view factor to the surrounding topography of below 0.08, with an average of 0.048 ± 0.005 (see Fig. 6.5 and Fig. 6.6). For this first analysis of the MARA data set two sets of models were calculated, one assuming $P_{th} = 0$, and the other assuming the highest view factor found close to the landing site, i.e. $f_{i,max} = 0.08$:

$$P_{th} = f_{i,max} \sigma_B \varepsilon T_{obs}^4 \tag{3.24}$$

This resulted in a conservative estimate of the thermal influence of the topography on the MARA observations.

3.4 MODELS AND MEASUREMENTS OF THERMAL CONDUCTIVITY, DENSITY AND HEAT CAPACITY

The thermal inertia is a useful parameter to describe the diurnal and seasonal temperature evolution of the surface material. However, to deduce structural properties of the surface and to learn more about its nature, the derived thermal inertia needs to be interpreted in terms of the thermal conductivity k, specific heat capacity c_p and density ρ. In this study, values for k, ρ, and c_p are derived from empirical fits and models based on experimental data from meteorites and lunar samples which are briefly summarized in the following sections.

3.4.1 *Density*

In this work, the density ρ in equation 3.16 represents an averaged density of the asteroid surface material over the modeled depth, i.e. the upper few decimeter of the surface. It incorporates the macroscopic and microscopic porosity, as well as the grain density of the regolith material and is defined as

$$\rho = (1 - \phi_{macro}) \rho_b \tag{3.25}$$

where ρ_b is the bulk density of the particles constituting the asteroid's regolith, and ϕ_{macro} is the macroscopic porosity, i.e the volume fraction of empty space between the regolith particles. The bulk density is defined as

$$\rho_b = (1 - \phi_{micro}) \rho_g \tag{3.26}$$

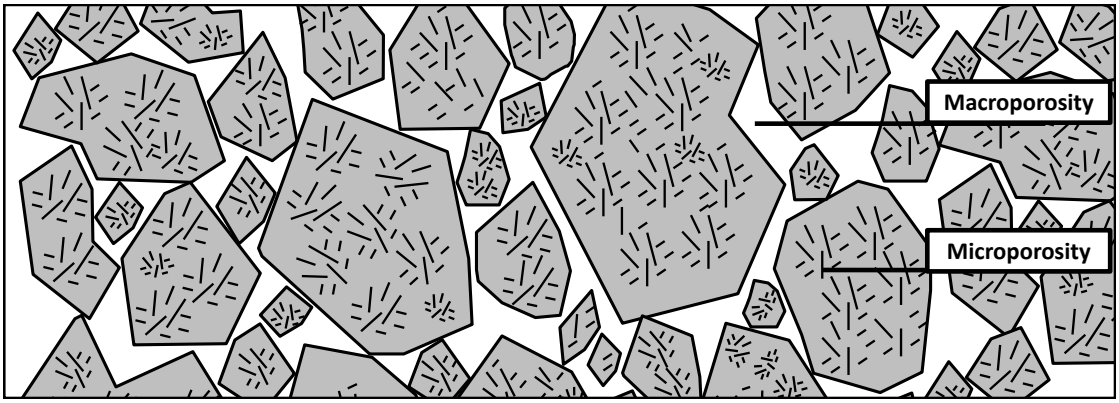

Figure 3.5: Illustration of a regolith cover indicating macroscopic porosity, which is the fraction of empty volume between the regolith particles, and the microscopic porosity, which is the fraction of empty volume within one of the regolith particles, e.g. pores, cracks, etc.

where the grain density ρ_g is the density of individual, microscopic grains that constitute larger particles, and ϕ_{micro} is the volume fraction of empty space between these microscopic grains. This is illustrated in Fig. 3.5 which shows regolith with individual particles and pebbles, indicating the macro- and microporosity.

A summary of measurements of bulk densities, porosity, and grain densities of chondritic meteorites is listed in Tab. 3.1 which is adapted from Flynn et al. (2018) and based on data from Macke (2010). The original data set included meteorite falls and finds. Meteorite falls are meteorites that have been observed falling and were collected shortly afterwards, whereas meteorite finds are meteorites that were found on Earth without observing the fall and which might have been exposed to terrestrial weathering for a long period of time. Where data from meteorite falls is available, only the falls data is shown and such data sets are denoted by the word "falls". The data for CH chondrites is not shown, as it is based on a single sample for which a negative porosity was measured and interpreted as a random measurement error of a porosity close to zero (Macke et al., 2011). The grain densities of the meteorites vary between 2420 and 5650 kg m^{-3} and while ordinary chondrites and dry carbonaceous chondrites generally have slightly larger grain densities, the grain density of the different groups of meteorites is generally similar. An exception are the CB chondrites which show abundant metallic chondrules with high density. The bulk densities show more variance and the carbonaceous chondrites tend towards lower values as their porosity is generally larger compared to ordinary ones. This is in particular true for aqueously altered, carbonaceous chondrites, i.e. CM and CI.

Type	Grain Density [kg m^{-3}]	Bulk Density [kg m^{-3}]	Porosity [%]
Ordinary Chondrites			
H (falls)	3710 ± 10	3350 ± 10	9.5 ± 0.4
L (falls)	3580 ± 10	3300 ± 10	8.0 ± 0.3
LL (falls)	3520 ± 10	3180 ± 20	9.5 ± 0.6
Carbonaceous Chondrites			
CI	2420 ± 60	1570 ± 30	34.9 ± 2.1
CM	2960 ± 40	2270 ± 20	22.2 ± 0.7
CR	3420 ± 80	3110 ± 140	9.5 ± 2.7
CB	5650 ± 10	5250 ± 190	3.9 ± 1.9
CV	3610 ± 10	2970 ± 30	17.7 ± 1.0
CO (falls)	3360 ± 20	3100 ± 70	7.6 ± 2.3
CK	3580 ± 20	2900 ± 50	17.7 ± 1.7
Enstatite Chondrites			
EL (falls)	3610 ± 30	3480 ± 50	3.7 ± 0.9
EH (falls)	3660 ± 40	3580 ± 50	2.1 ± 1.0

Table 3.1: Mean grain densities, bulk densities, and porosities of chondrites as provided by Flynn et al. (2018), based on data from Macke (2010). CH chondrites are not shown, due to measurement errors reportet in Macke et al. (2011). The data set includes both meteorite falls and finds, and when available only the falls are shown in the table indicated by the word "falls".

3.4.2 *Specific Heat Capacity*

Most measurements of the heat capacity of meteorites were performed above room temperature e.g. by Matsui et al. (1979) or Szurgot et al. (2012). Furthermore, Opeil et al. (2012) measured the heat capacity of Shergottite (type of Martian meteorites) "Los Angeles" between 1.9 and 400 K. Their results are summarized in the review article by Flynn et al. (2018). All these measurements where performed for stony meteorites and data for carbonaceous chondrites is entirely missing. However, while it appears that below 200 K heat capacity is a strong function of temperature it is less so at higher temperatures and depending on the sample it lies between 600 and 900 J kg^{-1} K^{-1}. The lunar samples returned by Apollo 14, 15, and 16 were another set of extraterrestrial material for which c_p was measured. In particular c_p of the soil samples 14163, 15301, and 60601, the breccia sample 14321, and basalt sample 15555 where measured by Hemingway et al. (1973) and are plotted in Fig. 3.6a as a function of

sample temperature. The heat capacity of these samples ranged from approximately 600 J kg^{-1} K^{-1} at 200 K to about 900 J kg^{-1} K^{-1} at 350 K, which is similar to the ones obtained for meteorite samples (Opeil et al., 2012). This range of heat capacity was considered to be representative for asteroid Ryugu's surface as well (Hemingway et al., 1973; Wada et al., 2018) and could be approximated by

$$c_p = -23.173 + 2.127T + 1.5009 \cdot 10^{-2}T^2 - 7.3699 \cdot 10^{-5}T^3 + 9.6552 \cdot 10^{-8}T^4 \quad (3.27)$$

where T is the temperature of the sample and c_p is given in units of J kg^{-1} K^{-1}. This fit is shown in Fig. 3.6a as a black line.

3.4.3 *Thermal Conductivity*

While density and heat capacity vary within the same order of magnitude across different meteorite materials, the thermal conductivity can vary over multiple orders of magnitudes depending on the structure of the surface material, in particular its grain size, and contributes most of the variance to the thermal inertia Γ (Neugebauer et al., 1971, e.g.).

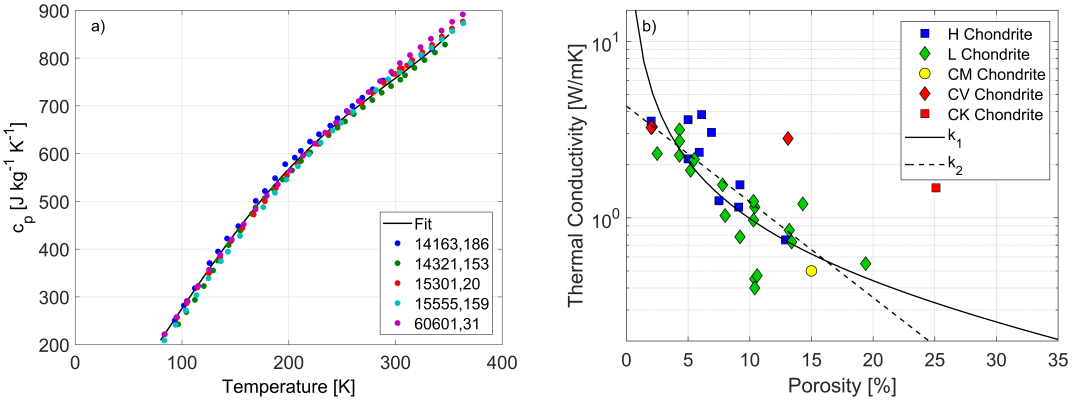

Figure 3.6: a) The specific heat capacity of lunar samples as reported by Hemingway et al. (1973) as a function of temperature with an empirical fit (equation 3.27) b) Thermal conductivity of meteorite samples as a function of porosity. Two models of thermal conductivity $k_1(\phi)$ (Flynn et al., 2018) and $k_2(\phi)$ (Henke et al., 2016) were derived through fitting the data. These models diverge for a porosity larger than 20% were no data is available to constrain the models.

The thermal conductivity describes the ability of a material to conduct heat. It is the sum of the solid thermal conductivity, gas thermal conductivity and a radiative part describing different heat transport mechanisms, respectively. In solid heat conduction, heat is transported in the form of phonons along a crystal lattice and it depends on the

composition of the material. Additionally, heat is conducted via photons of thermal radiation across spaces, e.g. pores or cracks, within the material. This process depends strongly on temperature and porosity, but also on the geometry of the pores. On bodies without atmospheres or abundant volatiles, heat transport through gas is very small and can thus be neglected on asteroids like Ryugu. However, on planets like Mars, the gas thermal conductivity needs to be included in the models (e.g. Vasavada et al. (2017)).

In granular material, such as a fine regolith cover, the solid thermal conductivity is governed by the inter-granular contacts rather than the bulk properties of the particles, and depending on the particle size, radiative heat transfer can contribute significantly to the total thermal conductivity. Recent theoretical models of thermal conductivity in granular material were published by Gundlach et al. (2013) and Sakatani et al. (2017), and the latter was successfully validated in laboratory studies with glass beads and lunar regolith stimulants (Sakatani et al., 2018). Sakatani et al. (2017) describe the solid and radiative contributions to the thermal conductivity as

$$k_{solid} = \frac{4}{\pi^2} k_m \left(1 - \phi_{macro}\right) C \, \xi \, \frac{r_c}{R_p} \tag{3.28}$$

$$k_{rad} = \frac{4\epsilon}{2 - \epsilon} \sigma \, T^3 \left[2 \, \zeta \left(\frac{\phi_{macro}}{1 - \phi_{macro}} \right)^{1/3} R_p \right] \tag{3.29}$$

with k_m the bulk thermal conductivity of the material, ϕ_{macro} the macroporosity between the grains, as illustrated in Fig. 3.5, C the coordination number representing the average number of inter-particle contacts per particle, r_c the radius of the contacts between the individual grains, an empirically determined factor accounting for the contact reduction by particle roughness ξ, a likewise empirically determined factor ζ accounting for the influence of the particle shape on the radiation distance, ε the emissivity of the particles, and the median particle radius R_p.

The bulk thermal conductivity k_m depends on the composition of the material but also on microscopic porosity and temperature. There are only few measurements of bulk thermal conductivity of meteorites, performed by Opeil et al. (2010, 2012), and measurements of thermal diffusivity κ of meteorites performed by Yomogida et al. (1983). The bulk thermal conductivity of meteorites lies between 0.4 and 5.5 W K^{-1} m^{-1} (Flynn et al., 2018), depending only weakly on temperature, for temperatures larger than 100 K. However, the bulk thermal conductivity depends strongly on the microporosity ϕ_{micro}. Two recently published models fitting the porosity dependence of k_m were introduced by Henke et al. (2016) and Flynn et al. (2018).

Henke et al. (2016) present a model fitting the data set by Yomogida et al. (1983) and Opeil et al. (2012):

$$k_m(\phi_{micro}) = 4.3 e^{-\phi_{micro}/0.08} \; [\mathrm{W\,m^{-1}\,K^{-1}}] \tag{3.30}$$

In the same work they present numerical models for the thermal conductivity of sintered grains, which match well thermal conductivity measurements of sandstone and sintered glass beads, but follow an entirely differend trend compared to the meteorite thermal conductivity. For Henke et al. (2016) this difference implies that the porosity in meteorites is not well described by sintered grains but rather by cracks within the meteorites which are caused by impacts or dehydration.

An alternative model is given by Flynn et al. (2018):

$$k_m(\phi_{micro}) = 0.11 \frac{1-\phi_{micro}}{\phi_{micro}} \ [\mathrm{W\,m^{-1}\,K^{-1}}] \tag{3.31}$$

In this model the meteorite is considered to be composed of a stack of two-dimensional layers between which heat is conducted and where the thermal conductivity scales with the contact area. This area is reduced by porosity and should scale with $(1-\phi_{micro})$. At the same time the thermal resistance $r = k^{-1}$ should scale with ϕ_{micro} which motivates the $(1-\phi_{micro})\phi_{micro}^{-1}$-dependency of equation 3.31. The factor of 0.11 is obtained by fitting the model to the meteorite data set. However, while providing a good fit to the meteorite data the model diverges for low porosity.

Almost the entire data set of Yomogida et al. (1983) and Opeil et al. (2012) consists of H and L chondrites, with very few E and LL chondrites. The thermal conductivity of only two carbonaceous chondrites was measured: CM2 Cold Bokkeveld with 0.5 W $\mathrm{K^{-1}\ m^{-1}}$ at 200 K and CK4 NWA 5515 with 1.48 W $\mathrm{K^{-1}\ m^{-1}}$ at the same temperature, and the thermal diffusivity of CV3 Leoville was measured by Yomogida et al. (1983). Therefore, the fits provided by Flynn et al. (2018) and Henke et al. (2016) might be a bias towards the more compact H and L chondrites. The data and models are shown in Fig. 3.6b and the model proposed by Flynn et al. (2018) is denoted $k_1(\phi)$ in the plot, while the fit by Henke et al. (2016) is denoted $k_2(\phi)$. Data for highly porous meteorite samples is lacking entirely and the two proposed models drastically diverge for a porosity larger 20 %. While the thermal conductivity of CM2 Cold Bokkeveld is fitted well by both models, the thermal conductivity of CK4 NWA 5515, and CV3 Leoville cannot be explained by k_1 or k_2. This could indicate that the porosity in that samples is fundamentally different from the others, e.g. the porosity could be more similar to sintered grains than to impact cracks as described by Henke et al. (ibid.). However, since the porosity of these two sample was not measured but modeled, it could also be an artifact of that method. CV3 Leoville appears multiple times in the plot, as the porosity differed between individual samples of that meteorite.

3.5 ROUGH SURFACES

As mentioned above, real surfaces are rough. The surface roughness causes small-scale heterogeneity in the surface temperature which is unresolved in an observing

instrument. This heterogeneity occurs as some parts of the topography face the sun while others point away from it. For example, at low solar elevation part of a crater wall will be shadowed while the opposite part faces the sun at a low incident angle and receives more flux compared to a flat surface. As a consequence, the observed flux depends on the observation geometry and rough surfaces are therefore non-Lambertian emitters. If the sun illuminates a surface from behind the observer, the observed flux will be enhanced by roughness, as the observed parts of the surface also face the sun. Contrarily, observations opposing the sun will measure lower fluxes compared to a flat surface.

Roughness is present at various length scales from large topographic features down to fine structures of the regolith grains. When the scale of the rough topography approaches the thermal diffusion length, temperatures equilibrate and roughness becomes less important. The diffusion length is defined here as the length a temperature signal propagates given a characteristic time t. It is a generalization of the diurnal skin depth d that was defined above, where the time scale is proportional to the rotation period $t = P/\pi$ and which is the length defined by a $1/e$ attenuation of the diurnal temperature wave. The diffusion length is generally given by

$$L = \sqrt{t\kappa} \tag{3.32}$$

where κ is the thermal diffusivity. For most observations in the thermal infrared the roughness of a surface is on a scale that is large enough to sustain temperature heterogeneity and yet too small to be resolved by the observing instrument, such that surface roughness needs to be included in the data analysis.

A common approach to account for roughness is to calculate a correction factor relating the flux of a modeled, rough surface to that of an ideal Lambertian emitter. This correction factor c depends on the angle between the surface normal and the observation direction θ_e, the solar incident angle θ_i, the angle θ_s between the observation direction and the solar vector projected onto the surface, a set of parameters describing the applied roughness model α_r, and the wavelength. The latter is due to the fact that the emission of a mixture of temperatures is the weighted sum of shifted Planck functions. The radiosity of rough surface is then given by

$$J_{rough} = \iint d\lambda d\Omega c(\theta_e, \theta_s, \theta_i, \alpha_r, \lambda)\tau(\lambda)FB(\lambda, T)\cos\theta_e \tag{3.33}$$

The correction factor c can than be multiplied to the modeled fluxes of the complex thermophysical models that are fitted to the data and where a direct implementation of small-scale roughness features is in most cases not feasible.

A common roughness model assumes a surface covered by spherical craters with a given radius and depth. Here, the thermal evolution is calculated assuming a given crater density and neglecting thermal conductivity, i.e. $k = 0$ (Giese et al., 1990; Kührt

et al., 1992; Lagerros, 1996). The latter assumption reduces the computational effort significantly, but the roughness effect vanishes at night. Parameters of this model are opening angle of the crater and the crater density d_c.

A more complex roughness model was developed by Davidsson et al. (2014) and Davidsson et al. (2015), where 1D and 3D thermal evolution was modeled for a variety of surfaces. Craters and trenches were modeled as well as surfaces with normally distributed, random elevation offsets and surfaces with self-similar, fractal topography. They found that the different types of roughness are generally similar but can show substantial differences at certain observation geometries. The various measures for degree of roughness (e.g. crater density, RMS slope, etc.) can be related to each other. Furthermore, when assuming a finite thermal conductivity, the roughness also affects nighttime temperatures, but to a smaller degree compared to daytime. Davidsson et al. (ibid.) found that self-heating, i.e. the heat transfer between parts of the topography, reduces the roughness effects as heat transfer tends to equilibrate temperatures.

In this study, the spherical crater model by Kührt et al. (1992) is employed, assuming c to be constant within the spectral range of the filters. Furthermore, the opening angle of the crater is fixed, leaving the crater density as the only free roughness parameter. Equation 3.33 thus simplifies to:

$$J_{rough} = c^*(\theta_e, \theta_s, \theta_i, d_c) J_{lambert} \tag{3.34}$$

3.6 PARAMETER ESTIMATION

In this work, the thermal inertia of the surface is retrieved by varying Γ in the thermophysical model and comparing the calculated temperatures to the MARA observation. The best fitting model is chosen by minimizing the χ^2 value which is a sum of squared differences between a given model and the observation, weighted by the uncertainty of the observation and which is defined by

$$\chi^2 = \sum_i \frac{(X_i^* - X_i)^2}{\sigma_i^2} \tag{3.35}$$

where X^* represents the model and X the observation with uncertainty σ for data points i.

The χ^2-value is a measure for the goodness of fit of a proposed model. Its probability distribution $f(\chi^2, \nu)$ can be interpreted as the probability density of a misfit occurring for a correct model, i.e. a model including the true material properties, and a data set whose uncertainties are Gaussian distributed. This means that $f(\chi^2, \nu)$ describes how likely a correct model will result in a χ^2-value for a given data set and the corresponding uncertainty. It depends on the number of degrees of freedom ν which is defined as

$\nu = N - p$, with N the number of data points and p the number of fitted parameters. The expected value of the distribution is equal to ν, which indicates that the average misfit between a model and an observation is close to the standard error of the data set. Very low and high values of χ^2 are unlikely to occur for a correct model, which means that if a model results in a $\chi^2 \gg \nu$ the model is unlikely to explain the data and can therefore be discarded. One can define a threshold value χ^2_c corresponding to a level of confidence α, defined by

$$\alpha = \int_{\chi^2_c}^{\infty} f(\chi^2, \nu) d\chi^2 \tag{3.36}$$

If $\alpha = 0.05$, the probability that a correct model results in a $\chi^2 > \chi^2_c$ is 5 %. Consequently the entirety of models resulting in $\chi^2 < \chi^2_c$ should correspond to a 2σ confidence interval, (also see Chap. 15.6 in Press et al. (1992) and Aster et al. (2013)).

For the interpretation of the MARA data, the parameter space was sampled through a grid search. The thermal model was evaluated varying the thermal inertia in steps of 10 $\mathrm{Jm^{-2}K^{-1}s^{-1/2}}$ and interpolating the resulting temperatures to thermal inertia steps of 1 $\mathrm{Jm^{-2}K^{-1}s^{-1/2}}$ for the grid search.

In the MARA data analysis (s. chapter 6) the thermal inertia was fitted for a variety of surface orientations. Furthermore, the thermal radiation of the terrain P_{th} was varied between 0 and 0.08, and the emissivity of the surface ε was varied between 1 and 0.9 in steps of 0.05. For each case thermal inertia values resulting in $\chi^2 < \chi^2_c$ were accepted. The entire range of accepted thermal inertias was estimated to be the uncertainty of the thermal inertia retrieval, as described in the method section of chapter 6.

Since k and c_p are generally functions of temperatures some studies directly incorporate temperature dependent k and c_p in their thermal model. In this case the thermal inertia is sometimes given for a certain temperature for the sake of comparability to other works. An example would be the thermal inertia estimates on the Moon by Hayne et al. (2017) where thermal inertia is given for a temperature of 273 K. However, while on the moon the temperature difference between day and night is large and can be of the order of hundred K (Paige et al., 2010), this study analyzes only the nighttime temperature observations by MARA where the temperature changed by 60 K, such that the temperature dependence of k and c_p should not be important. Nevertheless, a model incorporating the temperature dependency of k and c_p was fitted to the MARA data set but did not result in a better fit to the observation. Consequently, a temperature dependency of k and c_p for the observed boulder could be neglected.

By assuming c_p, ϕ, and ρ of the asteroid surface material, the thermal conductivity can be estimated from Γ. Through the relation of R_p and k, as described in equation 3.28 and 3.29, one can in principle try to estimate the typical regolith particle size of an planetary surface from such a thermal conductivity estimate. This was done in the case of Ryugu prior to the arrival of Hayabusa2, where the telescopically derived thermal inertia was 150 - 300 $\mathrm{J\,m^{-2}\,K^{-1}\,s^{-1/2}}$ (Müller et al., 2017). Under the assumption of a

bulk density of $\rho = 1100 - 1500\ \mathrm{kg\,m^{-3}}$, and a heat capacity of $c_p = 758\ \mathrm{J\,kg^{-1}\,K^{-1}}$ the regolith grain size was estimated to be $R_p = 3 - 30$ mm (Wada et al., 2018). However, Hayabusa2 and MASCOT revealed that such fine particles are very rare on the surface of Ryugu which is dominated by larger, decimeter to meter-sized objects as described in section 2.2. The assumptions on ρ were based on available meteorite data which might be biased towards denser objects surviving the fall through the atmosphere (Popova et al., 2011). Furthermore, as the particle size approaches the diurnal skin depth the observed diurnal temperature variation begins to represent the bulk properties of the individual regolith particles rather than a regolith cover. Under the assumption of ρ, c_p, and Γ given above the diurnal skin depth ranges from 1.5 to 3 cm, which is close to the estimated particle size. Uncertainties or bias in the other model parameters can have significant consequences for the estimated particle size. A particle size larger than the diurnal skin depth cannot be retrieved from thermal observations as the diurnal temperature range observed on a regolith cover with 5 cm particle size would be indistinguishable from that of a rough 5 m boulder.

In this study, the retrieved thermal inertia Γ was used to derive thermal conductivity and porosity by assuming a grain density $\rho_g = 2420\ \mathrm{kg\,m^{-3}}$ as measured for CI chondrites (Flynn et al., 2018) and c_p given by equation 3.27. The equations 3.28 and 3.29 could not be applied since MARA observed a single boulder rather than a fine, particulate regolith. Therefore, the bulk thermal conductivity models as given in equations 3.30 and 3.31 were used to estimate thermal conductivity and porosity and more details are given in section 6.3.5.

4

A METHOD TO DERIVE SURFACE THERMOPHYSICAL PROPERTIES OF ASTEROID (162173) RYUGU (1999JU3) FROM IN-SITU SURFACE BRIGHTNESS TEMPERATURE MEASUREMENTS

Maximilian Hamm (corresponding author), Matthias Grott, Ekkehard Kührt, Ivanka Pelivan, Jörg Knollenberg
German Aerospace Center (DLR), Insitute of Planetary Research, Rutherfordstr. 2, 12489 Berlin, Germany
Published in Planetary and Space Science, Volume 159, 15 September 2018, Pages 1-10
https://doi.org/10.1016/j.pss.2018.03.017

ABSTRACT

The MASCOT radiometer MARA on board the Hayabusa2 mission will measure surface brightness temperatures on the surface of asteroid (162173) Ryugu in six wavelength bands. Here we present a method to constrain surface thermophysical properties from MARA measurements. Moreover, uncertainties when determining surface thermal inertia as well as emissivity are estimated. Using data from all filters and assuming constant emissivity, thermal inertia of a homogeneous surface can be determined with an uncertainty range of 250 $\pm$16 $Jm^{-2}K^{-1}s^{-1/2}$, while the emissivity uncertainty is below 6 %. Similar results are obtained if emissivity is allowed to vary as a function of wavelength and if the MARA channels with the best signal-to-noise ratio are used to constrain thermal inertia. If the observed surface is heterogeneous and two morphologically different units are present in the instrument's field of view, thermal inertia of the subunits can be retrieved independently if their contrast in terms of thermophysical properties is large enough. If, for example, the surface is covered by equal area fractions of fine-grained and coarse-grained material, then thermal inertia is found to be retrievable with uncertainties of 658 $\pm$78 and 54 $\pm$22 $Jm^{-2}K^{-1}s^{-1/2}$ for the coarse-grained and fine-grained fraction, respectively.

4.1 INTRODUCTION

Surface processes on airless bodies are governed by their surface energy balance, and instruments to measure surface brightness temperatures have been payloads on several orbiter (Chase, 1969; Christensen et al., 2001; Fergason et al., 2006a; Hiesinger et al., 2010; Kieffer et al., 1972; Kührt et al., 1992; Okada et al., 2017; Paige et al., 2010; Tosi et al., 2014) and landed missions (Biele et al., 2008; Fergason et al., 2006b; Gómez-Elvira et al., 2012; Grott et al., 2017; Hamilton et al., 2014; Spohn et al., 2007, 2015; Vasavada et al., 2017). Thermal emission can change the orbit and spin state of small bodies through the Yarkovsky (Bottke et al., 2006; Chesley et al., 2003; Rubincam, 1995) and YORP (Bottke et al., 2006; Paddack, 1969) effects, and thermal fatigue due to repeated temperature cycling can result in breakup of rocks, adding to the generation of surface regolith (Delbo et al., 2014). While surface thermophysical properties depend on the detailed microphysics of grains and inter-grain contacts (e.g., Gundlach et al., 2013; Piqueux et al., 2009a,b; Sakatani et al., 2017), the majority of effects can be captured in a single parameter under the assumption that regolith properties are constant. This parameter is the surface thermal inertia, which determines the response of the surface temperature to insolation. While the assumption of constant regolith properties does not generally hold, it is widely applied since it greatly facilitates the analysis and interpretation of the returned thermal data.

Thermal inertia was derived for numerous planetary bodies from observations by telescope, spacecraft, and landed missions. In general, the data is fit by comparing observed temperatures to numerical thermal models, and surface thermophysical properties are then derived from best fits. Thermal models like the Near Earth Asteroid Thermal Model (NEATM, Harris, 1998) are used to fit data from unresolved observations like, e.g., spaceborne infrared telescopes (for example WISE and Spitzer, see, e.g., Landsman et al., 2016, Harris et al., 2016). The NEATM assumes a spherical shape and neglects rotation, roughness, as well as thermal conductivity and inertia. Instead, they introduce a fitting parameter η, which incorporates thermal inertia. In contrast, more complex thermophysical models (TPM) include heat conduction and often explicitly consider asteroid shape. They can include radiative transfer in the atmosphere (if present, e.g., Kieffer (2013)), or surface roughness (e.g.,Giese et al. (1990) Davidsson et al. (2014)). A TPM has also been used to model telescope data and derive thermal inertia for near-earth asteroid Itokawa (Müller et al., 2005, 2014).

Ideally, fitting a model to the data should consider the entire diurnal temperature curve. However, remote sensing usually delivers only sections of the diurnal curve due to viewing geometry restrictions (Christensen et al., 2001; Fergason et al., 2006a; Okada et al., 2017; Tosi et al., 2014). To compensate for this shortcoming, the fits are usually restricted to the coldest and hottest temperatures since they show the strongest dependence on regolith properties. These temperatures occur just before sunrise and shortly after local noon, respectively (Fergason et al., 2006a,b; Mellon et al., 2000).

Recently, a modified method to derive thermal inertia has been proposed by Takita et al., 2017, who consider the phase shift between the maximum daytime temperature and local noon. This method particularly suits a viewing geometry with the observing spacecraft hovering above the sub-solar point.

The situation is different for landed spacecraft, as those can observe the surface during an entire day-night cycle. This was done on comet 67P/Churyumov-Gerasimenko by the MUPUS radiometer (Spohn et al., 2015), as well as on Mars by the Rover Environmental Station Ground Temperature Sensor REMS-GTS (Hamilton et al., 2014) and the Mars Exploration Rovers' miniTES instruments (Fergason et al., 2006b). Fitting the entire diurnal temperature curve allows for a more precise thermal inertia estimation, since thermal inertia determines the rate of cooling and heating of the surface, and this rate is only fully recorded when the entire diurnal temperature data is available.

Further complications arise if temperatures in the instrument's field of view are heterogeneous below the spatial resolution of the employed sensors. The most common sources for sub-pixel heterogeneity are shadows, surface roughness, and heterogeneous thermal inertia, e.g. boulders and fine grains. The latter was identified as one complication when interpreting temperature data of the REMS-GTS sensor (Hamilton et al., 2014). Yet, surface roughness is known to considerably influence the total flux emitted by a given surface as it causes varying illumination conditions in the field of view (e.g., Kührt et al., 1992, Davidsson et al., 2014). However, if the entire diurnal temperature curve has been observed, a restriction of the analysis to nighttime data removes some of these effects, as temperature equilibration will result in more homogeneous temperatures reducing the effect of former shadowing or surface roughness (Fergason et al., 2006a). Therefore, heterogeneous thermal inertia will be the main source for sub-pixel heterogeneity during night.

In 2014, the Japanese Space Agency (JAXA) launched the Hayabusa2 mission to the near-earth asteroid (NEA) (162173) Ryugu (1999JU3) (Saiki et al., 2013; Tsuda et al., 2013). Hayabusa2 is a sample-return mission that will characterize this Cg-type asteroid (Bus et al., 2002) in great detail upon arrival in 2018, and will return samples to Earth in 2020. Hayabusa2 carries a thermal infrared mapper (TIR) (Okada et al., 2017; Takita et al., 2017) that will globally characterize surface temperatures and surface thermal inertia, as well as the MARA radiometer (Grott et al., 2017) as part of the payload on the MASCOT asteroid lander (Mobile Asteroid SCOuT, Ho et al., 2017). The MAscot RAdiometer (MARA) will observe a surface spot of approximately 12 cm diameter for a full asteroid rotation (7.631 h, Müller et al., 2017). Under nominal landing conditions this spot will consist of undisturbed regolith roughly 30 cm in front of the lander. The emission angle will be 50° in average (Grott et al., 2017).

After the first set of data has been acquired, MASCOT relocates to a second site, to continue to operate until its primary batteries run out, which are expected to last up to 16 h. At the same time, the main spacecraft's TIR instrument will observe the asteroid from the Hayabusa2 home position at about 20 km altitude above the sub-solar point.

Table 4.1: (162173) Ryugu parameters used for calculating surface temperatures in the asteroid TPM.

Parameter	Symbol	Value	Unit
Perihelion Distance	a	0.96315	AU
Eccentricity	e	0.19034	-
Pole Orientation	(λ,β)	(329,-39)	$^\circ$ (ecliptic coordinates)
Rotational Period	P	7.631	h
Bond Albedo	A	0.018	-
Emissivity	ε	0.9	-
Heat capacity	c_p	600	J kg^{-1} K^{-1}
Density	ρ	1270	kg m^{-3}
Thermal Conductivity	k	variable	W m^{-1} K^{-1}

Table 4.2: Overview of MARA channels giving the filter name along with the corresponding transmission wavelength range. To illustrate the wavelength dependence of thermal inertia retrieval when assuming a single thermal inertia while observing a heterogeneous surface, the best-fitting thermal inertia for each MARA channel is also given. In this calculation, the heterogeneous surface was assumed to be covered to 75% by material with $\Gamma = 650$ Jm^{-2}K^{-1}s$^{-1/2}$ and to 25% by material with $\Gamma = 50$ Jm^{-2}K^{-1}s$^{-1/2}$.

Filter Name	B6	W8	B9	B13	W10	SiLP
Wavelength [µm]	5.5-7	8-9.5	9.5-11.5	13.5-15.5	8-12	>3
Γ [Jm^{-2}K^{-1}s$^{-1/2}$]	405	426	398	367	404	377

The simultaneous observations will allow a joint interpretation of MARA and TIR data. MARA operates an array of six detectors which will observe the asteroid's surface in six individual infrared wavelength bands. Four of the employed filters are narrow band (width of 1.5 - 2 µm), while a silicon long pass transmits radiation with wavelength larger than 3 µm and a second broadband filter transmits radiation from 8 to 12 µm (Grott et al., 2017). Tab. 4.2 provides an overview of the filters used by MARA, their transmissivity bands, and their designations in this paper.

In the following, we describe a method to determine surface thermal inertia from MARA data taking instrument errors as well as other sources of uncertainty into account. In particular, the influence of an unknown surface emissivity is discussed. Furthermore, we consider heterogeneous surfaces, and address the feasibility of retrieving multiple

thermal inertias. Synthetic MARA data is generated using an asteroid surface thermal model (Pelivan et al., 2017), which is presented in Sec. 4.2.1. Radiation exchanged between the surface and the MARA detectors is calculated using the net radiation method (Howell et al., 2016), from which synthetic MARA signals are derived taking the instrument's calibration function into account (Grott et al., 2017). Finally, surface thermophysical properties are derived from the generated signals, and confidence limits are estimated.

4.2 METHODS

4.2.1 *Asteroid Thermal Model*

To calculate synthetic MARA data, asteroid surface temperatures during the observation period are simulated. To this end, we use a thermophysical model (TPM) of the target asteroid (162173) Ryugu, which generates diurnal surface temperature curves by solving the one-dimensional heat conduction equation subject to the boundary conditions at the surface (Eq. 4.3) and a boundary condition of zero heat flux at depth. The model is described in detail by Pelivan et al. (2017). The employed solver is part of the commercial NAG Library. It uses the method of lines to convert the partial differential equation into a system of ordinary differential equations and subsequently applies the backward differentiation formula for time integration.

Asteroid surface and subsurface temperatures T are governed by the heat conduction equation

$$\frac{\partial T}{\partial t} = \frac{\pi}{P}\frac{\partial^2 T}{\partial z'^2} \tag{4.1}$$

where t is time, P is the asteroid's rotation period, and $z' = z/d$ is depth normalized to the diurnal thermal skin depth

$$d = \sqrt{\frac{k}{\rho c_p}\frac{P}{\pi}} \tag{4.2}$$

where ρ is regolith density, c_p is regolith heat capacity, and k is regolith thermal conductivity. The upper boundary condition is given by the surface energy balance. As a result of the renormalization we can express it as

$$\sigma_B \varepsilon_{avr} T^4 = (1 - A)S + \Gamma\sqrt{\frac{\pi}{P}}\left.\frac{\partial T}{\partial z'}\right|_{z'=0} \tag{4.3}$$

where σ_B is the Stefan-Boltzmann constant, ε_{avr} is surface emissivity averaged over the Planck function which is approximated by a constant in this study, A is bond albedo, S is insolation, and Γ is thermal inertia. The latter is given by

$$\Gamma = \sqrt{k\rho c_p} \tag{4.4}$$

and governs the surface response to heating. Regolith with low thermal inertia heats up fast during the day and cools rapidly during nighttime, whereas regolith with high thermal inertia reacts slowly to insolation changes. As the range of variability is small for heat capacity and density, variations of thermal conductivity mainly determine the thermal inertia (Neugebauer et al., 1971). Insolation is governed by the solar incidence angle θ_I, which is defined as zero for vertical insolation, and the heliocentric distance r_h. It is given by

$$S = \frac{S_0 \cos\theta_I}{{r_h}^2} \qquad \text{for } \cos(\theta_I) > 0 \tag{4.5}$$

and is zero otherwise. In this study, (162173) Ryugu is assumed to have a spherical shape, such that the solar incidence angle can be expressed analytically.

Under nominal conditions, MASCOT will not shadow the observed surface spot and we therefore ignore this possibility in the following. However, if shadowing does occur during on-asteroid operations, this would be included in the analysis. We estimate that the observed surface spot receives only a few hundred mW to a few W of thermal radiation from MASCOT. This is by orders of magnitudes smaller than the insolation or the heat dissipated during nighttime. Therefore, it can be assumed that the thermal influence of MASCOT on the observed surface is negligible.

It is worth noting that we have assumed regolith properties to be constant in Eqs. 4.1 and 4.3, as thermal inertia cannot be defined if parameters are allowed to vary as a function of temperature or depth. Therefore, one should in principle use the underlying parameters like thermal conductivity directly when analyzing thermal emission. However, this is usually not done since the different parameters in general can not be disentangled using the available data. Nevertheless, temperature dependence of thermal conductivity can have a significant influence on the obtained results (Gundlach et al., 2013; Piqueux et al., 2011; Sakatani et al., 2017), and thermal inertia is therefore generally interpreted at a representative surface temperature when estimating, e.g., grain size from thermal conductivity (Gundlach et al., 2013; Müller et al., 2017). Here we consider only nighttime data, thus minimizing the influence of temperature dependence by restricting the analysis to a section of the diurnal curve with little variability.

Eqs. 4.1 and 4.3 are solved assuming orbital, spin, and material parameters as appropriate for (162173) Ryugu, and relevant parameters are summarized in Tab. 4.1. Rotational parameters were derived from telescopic observations (Müller et al., 2017), while Bond albedo A was calculated from the phase integral q and the geometric albedo $p \sim 0.047$ (ibid.) according to $A = pq$. The phase integral q was determined from the G-slope $G = 0.13 \pm 0.02$ (Ishiguro et al., 2014) according to $q = 0.290 + 0.684G$ (Bowell et al., 1989), which yields $A = 0.018$. The Light Detection and Ranging (LIDAR) instrument of the Hayabusa2 spacecraft will be able to derive the albedo of (162173) Ryugu with an uncertainty of 18 % (Yamada et al., 2017). For the low albedo expected for Ryugu, we find that the corresponding temperature uncertainty is well below the uncertainty of the MARA measurement, and the LIDAR instrument will provide an

albedo map with sufficient resolution to determine the local albedo at the landing site. In addition, the MASCOT Camera (Jaumann et al., 2017) will provide images of the surface in the MARA field of view, further constraining the local albedo. Therefore, albedo is not varied and assumed to be a known quantity in the following.

Given the input parameters, the TPM is integrated in time for three orbital periods. This allows subsurface temperatures to stabilize and surface temperature uncertainties are typically below 0.5 K after this time period. These uncertainties are not the numerical uncertainty but the orbit-to-orbit difference of the surface temperatures at a given orbital difference. Maximum timesteps were restricted to $1/72^{th}$ of a rotation period, resulting in output every 5° of local hour angle. The adopted spatial resolution is 41 gridpoints in the vertical direction, which are distributed at increasing distances over a depth-range of eight annual skindepths. Resulting surface temperatures at the equator are shown in Fig. 4.1 for three different thermal inertias, and temperatures differ significantly depending on Γ. While low thermal inertia surfaces with $\Gamma = 50$ $\mathrm{Jm^{-2}K^{-1}s^{-1/2}}$ exhibit diurnal temperature cycles of 200 K amplitude, high thermal inertia of 650 $\mathrm{Jm^{-2}K^{-1}s^{-1/2}}$ reduces this range to 70 K.

4.2.2 *Net Radiation Method for Heat Transfer*

Once asteroid surface temperatures have been determined using the TPM (Sec. 4.2.1 above), signals generated by the MARA sensors can be simulated by calculating the radiation exchange between instrument and the surface(s) in the field of view. This study uses a heat transfer model applying the net radiation method for enclosures (Howell et al., 2016) to calculate the radiative flux onto the sensors. The general measurement scenario is sketched in Fig. 4.2. MARA is assumed to view multiple surfaces at different temperatures, while surfaces view each other as well as deep space. In the following, we consider each MARA channel independently.

The model calculates the heat exchanged within the enclosure defined by a number of surfaces and deep space, which emit and reflect thermal radiation according to their emissivity ε. In the following, the enclosure consists of one or two asteroid surface elements, the MARA detector, as well as deep space, the latter being modeled as a perfectly black surface at zero temperature. All surfaces are considered to be Lambertian surfaces, and MARA filters are assumed to block all radiation outside their transmission range.

In the heat transfer model, the spectral radiosity J of surface element i can be expressed as

$$J_i(\lambda) = \pi\varepsilon_i B(T_i, \lambda) + (1 - \varepsilon_i) \sum_j^N F_{ij}\tau_{ij}(\lambda) J_j(\lambda) \tag{4.6}$$

where λ is wavelength and $B(T_i, \lambda)$ is the Planck function. The factor π is the result of integrating over the solid angle for a hemisphere, again considering the surface to be a

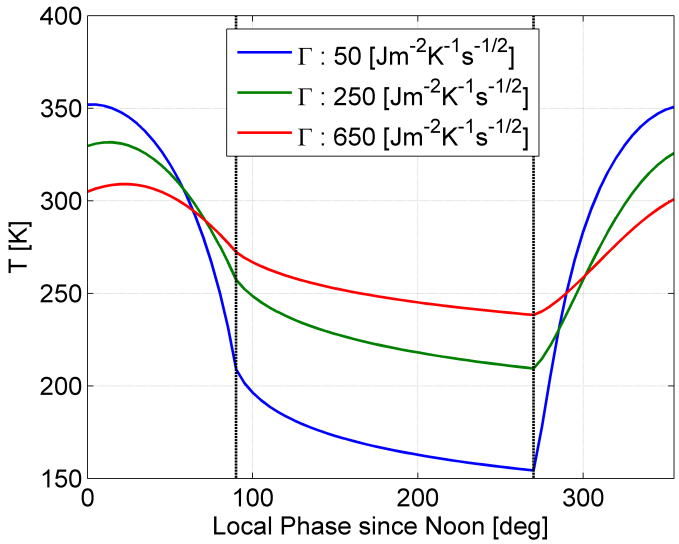

Figure 4.1: Surface temperatures as a function of local phase since noon for three thermal inertias used throughout this study: $\Gamma = 50$, 250 and 650 $\mathrm{Jm^{-2}K^{-1}s^{-1/2}}$. The vertical black lines mark the beginning and end of the night. Temperatures were evaluated at the equator of a spherical Ryugu for a season corresponding to the nominal MASCOT landing around October 1st, 2018.

Lambertian emitter. The detector is chosen to correspond to the first surface element $i = 1$, and $\tau_{ij}(\lambda)$ represents the filter's transmission function. Therefore, all $\tau_{1j}(\lambda)$ and $\tau_{i1}(\lambda)$ are equal to the filter transmissivity $\tau(\lambda)$, while all other $\tau_{ij}(\lambda) = 1$. F_{ij} are the view factors, i.e., the fraction of flux produced by surface j illuminating surface i. The view factors are related by

$$F_{ij} = \frac{a_j}{a_i} F_{ji} \tag{4.7}$$

with a_i being the surface area of element i (Davidsson et al., 2014) and N the number of surfaces participating in the heat exchange. The first term in Eq. 4.6 represents thermal emission of element i, while the reflected fraction of radiation incoming from other surfaces in the enclosure is captured in the second term.

The reflected radiation couples the radiosities of all surfaces within the enclosure, resulting in a coupled set of linear equations that can be rearranged in matrix form according to

$$\boldsymbol{B} = \hat{M} \cdot \boldsymbol{J} \tag{4.8}$$

where $\boldsymbol{B}$ and $\boldsymbol{J}$ are vectors containing the Planck functions and spectral radiosities of all

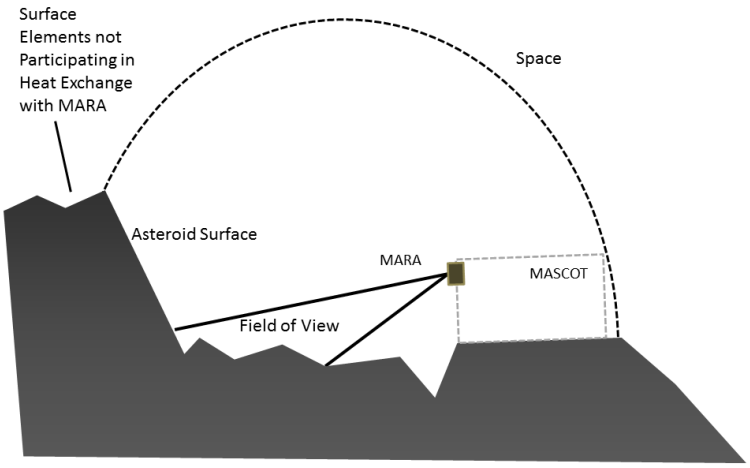

Figure 4.2: Schematic sketch of the radiative heat transfer model. MARA is situated in the lander MASCOT observing the asteroid surface with potentially multiple surface elements in the field of view.

surfaces inside the enclosure, respectively. The matrix $\hat{M}$ is obtained by rearranging Eq. 4.6 and can be expressed as

$$\hat{M} = \frac{1}{\pi} \begin{pmatrix} 1 & 0 & \dots & 0 \\ 0 & \frac{1}{\varepsilon_2} - \frac{1-\varepsilon_2}{\varepsilon_2} F_{22} & \dots & -\frac{1-\varepsilon_2}{\varepsilon_2} F_{2N} \\ \vdots & \vdots & \ddots & \vdots \\ 0 & -\frac{1-\varepsilon_N}{\varepsilon_N} F_{N2} & \dots & \frac{1}{\varepsilon_N} - \frac{1-\varepsilon_N}{\varepsilon_N} F_{NN} \end{pmatrix} \tag{4.9}$$

where we have assumed the emissivity of the detector to be unity, i.e., $\varepsilon_1 = 1$. Furthermore, the view factors of the N surface elements towards the detector are very small, such that $F_{j1} \approx 0$ for all $j > 1$. This is equivalent to the assumption that the influence of MARA on the surface temperature is negligible. All terms containing $\tau_{ij}(\lambda) \neq 1$ vanish. Inverting this matrix then gives the spectral radiosities for a given set of surface temperatures

$$\boldsymbol{J} = \hat{M}^{-1} \cdot \boldsymbol{B} \tag{4.10}$$

Once $\boldsymbol{J}$ is known, the net heat flux onto the detector can be calculated by considering

energy conservation. All radiative exchange between detector and surroundings has to to pass through the filter, such that the net radiation at the detector is given by

$$Q_1 = a_1 \int d\lambda \sum_{i=2}^{N} F_{1i}\, \tau(\lambda)[J_1(\lambda) - J_i(\lambda)] \tag{4.11}$$

It is worth noting that the assumption of an isothermal sensor with perfectly black interior will in general not hold, and small temperature inhomogeneities across the sensor will result in an offset heat flux, which will enter Eq. 4.11 as an additive constant. This offset has been estimated during instrument calibration (Grott et al., 2017) and could largely be corrected for by including a heating power dependent term in the analysis. However, verification measurements revealed that residual errors between 0.5 and 5 K remain. These channel and target temperature dependent uncertainties are included in the data synthesis and fitting in the following.

4.2.3 *Data Synthesis and Fitting*

In this paper, we determine confidence limits for estimating regolith thermophysical properties from MARA observations. To this end, we compare the flux generated by the asteroid's surface for different regolith thermophysical properties with that measured by the instrument. We determine the range of admissible surface properties by comparing emitted and measured fluxes taking instrument uncertainty into account. In the following, we apply the heat transfer model to two cases: First, we consider fluxes emitted by a homogeneous, flat surface, while in a second application we investigate the mixed signal generated by two surfaces at different temperatures.

In the first case, the enclosure defined by Eq. 4.6 consists of three surfaces, i.e., the detector (1), the target surface (2), and the sky (3). The emissivities of sky ε_3 and detector ε_1 are assumed to be unity, and the emissivity of the surface is denoted by $\varepsilon_2 = \varepsilon$ for brevity. The surface emissivity is considered to be constant in each of the filter channels, but will in general vary from filter to filter as a function of wavelength. The detector and target surface are assumed to be flat, such that $F_{11} = F_{22} = 0$. The area of the sky is assumed to be infinite, exchanging radiation only with the target surface and itself, such that $F_{31} = F_{32} = 0$ and $F_{33} = 1$. As the area of the detector is small compared to that of the target surface $F_{21} \approx 0$ and $F_{23} \approx 1$. F_{12} is defined by the instrument's field of view of $\theta = 20°$ full width half maximum (ibid.) and is approximated by

$$F_{12} = \frac{1}{2}(1 - \cos\theta) \tag{4.12}$$

This assumes that the target area is large enough to fill the entire field of view, independent of observation angle. The temperature of the sky is assumed to be 0 K, such that

$J_3 = 0$. Under these assumptions, the net heat flux at the detector calculated by means of Eq. 4.11 is given by

$$Q_1 = a_1 \pi \int d\lambda \, \frac{1}{2}(1 - \cos\theta)\tau(\lambda)[B(T_1, \lambda) - \varepsilon B(T_2, \lambda)] \tag{4.13}$$

In the second case, two large surfaces with different temperatures are located within the field of view, i.e., a new surface (4) is added to the enclosure. The two surfaces are again considered to be flat and parallel to each other such that the view factors $F_{24} = F_{42} = 0$. The emissivity of the new surface is considered to be equal to ε, and $F_{41} = 0$ as well as $F_{43} = 1$ are assumed, i.e., the view factor of the detector with respect to the surface is assumed to be small. The area fraction of each surface in the field of view then determines the view factors F_{12} and F_{14}, and

$$F_{12} = \frac{f_a}{2}(1 - \cos\theta) \tag{4.14}$$

$$F_{14} = \frac{f_b}{2}(1 - \cos\theta) \tag{4.15}$$

where f_a and f_b are the fractions of the field of view covered by each of the two surfaces and $f_a + f_b = 1$. The heat flux on the detector then equals

$$Q_1 = a_1 \pi \int d\lambda \, \frac{1}{2}(1 - \cos\theta)\tau(\lambda)[B(T_1, \lambda) - \varepsilon(f_a \, B(T_2, \lambda) + f_b \, B(T_4, \lambda))] \tag{4.16}$$

Net fluxes at the detector given by Eqs. 4.13 and 4.16 depend on the temperatures T_2 and T_4, which in turn depend on surface emissivity ε and thermal inertia Γ through the TPM (Section 4.2.1). Therefore, given ε and Γ, the signal generated by the instrument can be calculated in the following way: First, surface temperatures are determined using the TPM. Then, net heat fluxes at the detector are calculated using the net radiation method for heat transfer (Sec. 4.2.2). Finally, MARA signals are calculated from the instrument calibration coefficients S_0, S_1, and S_2 according to (ibid.):

$$U(\varepsilon, \Gamma) = S_0 + S_1 \, Q_1(\varepsilon, \Gamma) + S_2 \, Q_1(\varepsilon, \Gamma)^2 \tag{4.17}$$

The temperature uncertainties determined during calibration are much larger than the instrument noise and thus dominate the total error budget. For each synthesized data point we define the uncertainty $\sigma(T)$, which is determined by error propagation of the total temperature uncertainty from verification measurements (ibid.) into the signals. It depends on the target temperature and the channel. For example, at a target temperature of 250 K the temperature uncertainty in the silicon long pass channel is of the order of 0.5 K corresponding to 2 μV in signal.

To determine the admissible range of surface parameters compatible with the derived MARA signal (Eq. 4.17) we apply a χ^2-test. In a grid search, a suit of TPMs is calculated varying ε and Γ about their input values and the nominal instrument response for this

parameter combination is determined. A parameter set ε^* and Γ^* is then found to be admissible if the χ^2 defined by

$$\chi^2(\varepsilon^*, \Gamma^*, \varepsilon, \Gamma, \sigma) = \sum_i \frac{(U_i^*(\varepsilon^*, \Gamma^*) - U_i(\varepsilon, \Gamma))^2}{\sigma_i^2} \tag{4.18}$$

lies within a range $\Delta\chi^2 = |\chi_c^2(\alpha, \nu) - \chi_{min}^2|$ around the minimum χ_{min}^2 (Chapt 15.6 in Press et al. (1992)). In Eq. 4.18 the sum is evaluated over all data points. The χ_c^2 value depends on the confidence limit α as well as the number of degrees of freedom ν and is defined by

$$\alpha = \int_{\chi_c^2}^{\infty} f(\chi^2, \nu) d\chi^2 \tag{4.19}$$

where $f(\chi^2, \nu)$ is the χ^2-distribution and ν is equal to the number of data points minus the number of fit parameters (compare Aster et al. (2013)). This study simulates 37 nighttime data points corresponding to hour angle steps of 5°, leaving 35 degrees of freedom. For $\alpha = 0.05$ this corresponds to a $\chi_c^2 = 49.8$. For a sufficiently large dataset, χ_{min}^2 will be equal to the expectation $\langle f \rangle = \nu$, i.e., the number of degrees of freedom, which results in a range $\Delta\chi^2 = 14.8$. We can thus apply $\Delta\chi^2$ to estimate the range of admissible parameters by discarding all parameters yielding χ^2 values outside that range.

4.3 RESULTS

In the following, we investigate the feasibility of deriving thermal inertia from nighttime measurements given different sources of uncertainty. Besides the random instrument uncertainty, we consider two additional sources of systematic uncertainty. First, we investigate the effect of an unknown and wavelength dependent surface emissivity, second a heterogeneous surface in the field of view. For the latter, heterogeneous thermal properties can be expected for the different units, e.g. boulders and fines, resulting in different surface temperatures. This mixed signal is investigated for the case of two surfaces with different thermal inertia within the field of view of MARA. Two surfaces sufficiently show that this effect will systematically deform the diurnal temperature curve, hindering fitting the brightness temperature curves using a single thermal inertia.

4.3.1 *Homogeneous Surfaces*

First we consider a homogeneous surface with unknown emissivity and estimate how the trade-off between emissivity and surface thermal inertia influences the fidelity of

the retrieved thermal inertia. As an emissivity spectrum, we first consider a surface with constant emissivity $\varepsilon = 0.9$. Second, we study a surface exhibiting $\varepsilon(\lambda)$ corresponding to a measured serpentine spectrum as well as a measured spectrum of the Allende Meteorite. The spectra were measured at the Planetary Emissivity Lab (Maturilli et al., 2016) and the nominal thermal inertia of the surface was set to 250 $\mathrm{Jm^{-2}K^{-1}s^{-1/2}}$ in all cases.

The range of admissible emissivity and thermal inertia is retrieved by performing a grid search varying emissivity in steps of 0.01 from 0.75 to 1, and varying thermal inertia in steps of 2 $\mathrm{Jm^{-2}K^{-1}s^{-1/2}}$ from 100 to 400 $\mathrm{Jm^{-2}K^{-1}s^{-1/2}}$, discarding those ε/Γ-combinations resulting in χ^2-values outside the range set by $\Delta\chi^2 = 14.8$. This calculation is carried out independently for all six MARA channels. To estimate uncertainty ranges for the ε/Γ-combinations, the resulting error ellipses are projected onto the coordinate axes, the resulting axis-intervals corresponding to the 2σ-confidence intervals.

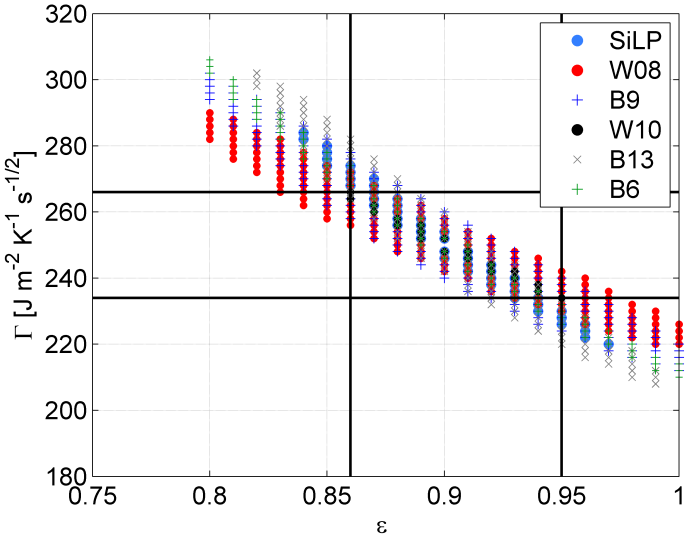

Figure 4.3: Admissible combinations of emissivity ε and thermal inertia Γ fitting the MARA signal in different wavelength channels (Tab. 4.2) generated by observing a surface with a flat emissivity spectrum of $\varepsilon = 0.9$ and a thermal inertia of $\Gamma = 250$ $\mathrm{Jm^{-2}K^{-1}s^{-1/2}}$. The black lines show the projection of the best fitting parameters onto axes.

Inversion results for the surface exhibiting a flat spectrum of $\varepsilon = 0.9$ and surface thermal inertia of 250 $\mathrm{Jm^{-2}K^{-1}s^{-1/2}}$ are shown in Fig. 4.3, where admissible parameter combinations are shown for each MARA channel. Since ε is the same in all channels, the range of admissible ε can be narrowed down considerably and the broadband filter W10 best constrains ε, resulting in $\varepsilon = 0.9^{+0.05}_{-0.04}$. Using this emissivity range, admissible thermal inertia is found to be 250 ± 16 $\mathrm{Jm^{-2}K^{-1}s^{-1/2}}$, and a anti-correlation between retrieved emissivities and thermal inertias is evident in Fig. 4.3. It is therefore

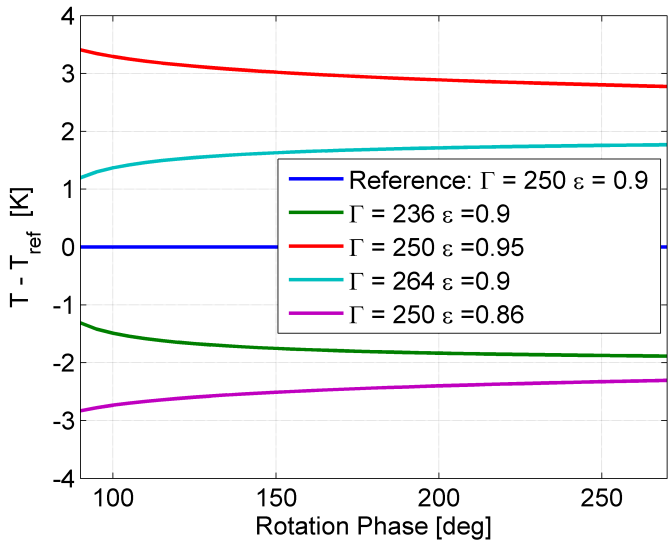

Figure 4.4: Brightness temperature difference between the reference TPM results and cases with changed thermal inertia and emissivity as a function of rotation phase. Thermal inertia and emissivity values considered correspond to the extreme admissible values obtained in Fig. 4.3.

worth noting that setting the emissivity to unity, as is often done in the literature, underestimates the thermal inertia, and values around 218 ± 8 Jm^{-2}K^{-1}s$^{-1/2}$ would be obtained instead of 250 ± 16 Jm^{-2}K^{-1}s$^{-1/2}$.

The effects of thermal inertia and emissivity on the diurnal temperature curve during nighttime are shown in Fig. 4.4, where the brightness temperature difference between temperatures obtained for the nominal parameter set and the extreme admissible values of thermal inertia and emissivity are given. Increased thermal inertia results in a positive temperature offset in addition to lowering the cooling rate, while an increase of emissivity results in a positive brightness temperature offset and increased cooling rate. Furthermore, for a fixed brightness temperature overestimating the emissivity will result in an underestimated kinetic temperature. During nighttime, this corresponds to a lower thermal inertia. This implies that an overestimated emissivity can compensate for an underestimated thermal inertia to some extent and explains the anti-correlation between thermal inertia and emissivity found in 4.3. However, as the effects of emissivity and thermal inertia significantly differ in strength, large deviations of emissivity and thermal inertia from the true parameters cannot compensate each other.

As a next step, we investigate a homogeneous surface with wavelength dependent emissivity, as it would be expected for regolith targets. Two cases are analyzed, and in the first test a serpentine emissivity spectrum is assumed, while in a second test the spectrum as measured for the Allende meteorite is prescribed. The former spectrum has been chosen since the Hayabusa2 target asteroid (162173) Ryugu may show signs

of aqueous alteration (Bus et al., 2002), while the second spectrum was taken to be representative for carbonaceous chondrite material. Results for the serpentine spectrum are shown in Fig. 4.5. Since emissivity is no longer constant across different filters, each filter has to be considered independently when estimating $\varepsilon(\lambda)$. However, since thermal inertia must be constant for all filters, the estimate of 250 $\pm$16 $\mathrm{Jm^{-2}K^{-1}s^{-1/2}}$ provided by the W10 filter can be used to narrow down the range of emissivities admissible in the other filters, and the corresponding range is indicated by the two black lines in Fig. 4.5. Admissible emissivity ranges are then given by those values within the band spanned by $\Gamma = 250 \pm 14$ $\mathrm{Jm^{-2}K^{-1}s^{-1/2}}$. As for the Allende spectrum, the inverted thermal inertia was found to be 250^{+14}_{-10} $\mathrm{Jm^{-2}K^{-1}s^{-1/2}}$ (not shown in figure).

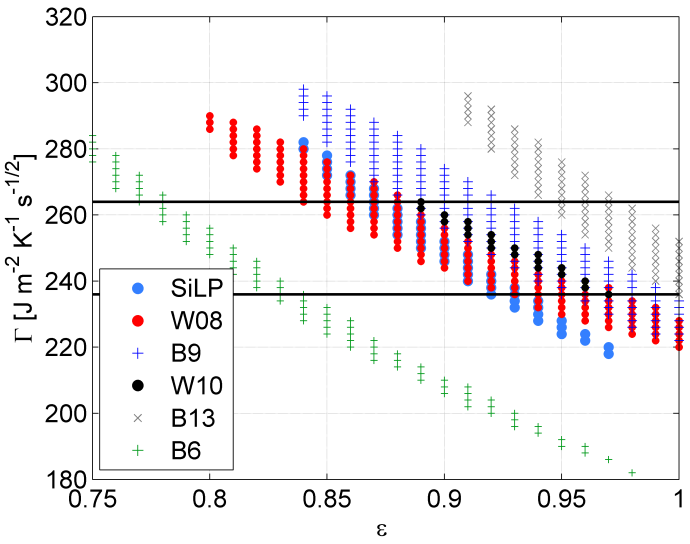

Figure 4.5: Same as Fig. 4.3, but for a surface exhibiting a serpentine-like emissivity spectrum. The black lines show the tightest constraint on the thermal inertia. Projecting the intersections of these two lines with each of channel's ellipses onto the ε-axis constrains the emissivity in each channel.

These results indicate that the MARA instrument can be used to estimate $\varepsilon(\lambda)$ for the narrow pass filters, provided thermal inertia (and thus surface temperature) are constrained by one of the broadband filters. In this case, emissivities can be constrained using the above approach, and results for simulations covering both the serpentine as well as the Allende spectra are shown in Fig. 4.6, where the measured spectra are shown together with the retrieved emissivities as a function of wavelength. Boxes indicate the emissivity uncertainties, and despite the relatively large uncertainty MARA measurements can distinguish between the two materials based on the spectral slope in the 6-10 μm wavelength range.

4.3.2 *Heterogeneous Surfaces*

Temperature heterogeneity in the field of view is another source of uncertainties when inverting measured fluxes for thermophysical properties. This could be caused by, e.g., shadows or the presence boulders embedded in fine grains corresponding to distinct thermal inertias. Mixed temperatures will influence the observed brightness temperature in a non-linear way, and the emitted flux must then be described by a superposition of Planck functions at different temperatures. The observed brightness temperature will thus be lower at dusk and higher at dawn as compared to the diurnal temperature curve of a homogeneous surface, and fitting the mixed signal using a single thermal inertia will result in systematic offsets between model and observation.

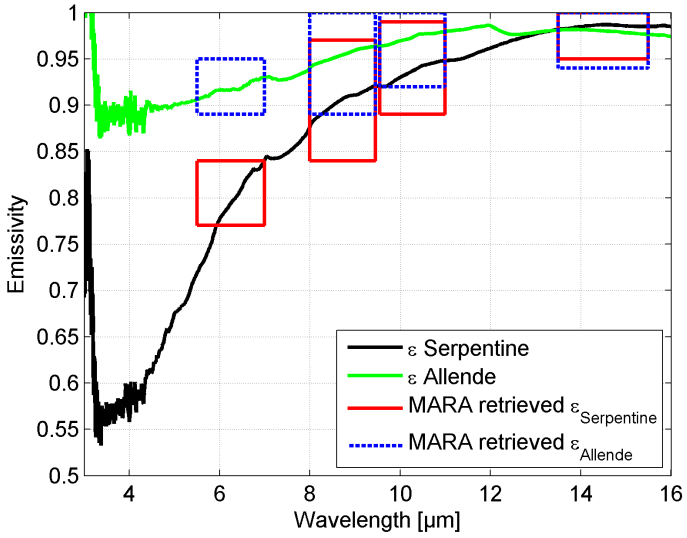

Figure 4.6: Emissivity as a function of wavelength as measured for a serpentine (black) and Allende Meteorite sample (green). Boxes indicate the emissivities retrieved using the corresponding MARA narrow-band filters, where blue boxes refer to the serpentine and red boxes refer to the Allende sample, respectively.

To demonstrate this effect, we model the flux emitted by a surface which is covered to 75 % by material with $\Gamma = 650$ Jm^{-2}K^{-1}s$^{-1/2}$ and to 25% by material with $\Gamma = 50$ Jm^{-2}K^{-1}s$^{-1/2}$. This would correspond to a surface partially covered with fine regolith and grain sizes of a few μm as well as coarse, centimeter-sized pebbles (Gundlach et al., 2013; Sakatani et al., 2017). The resulting mixed-signal diurnal brightness temperature curve is then modeled assuming a single surface thermal inertia, and the misfit between model and simulated observations is shown in Fig. 4.7 as a function of rotation phase. As is evident from the figure, the model using a single thermal inertia systematically overestimates temperatures at dusk by up to 6 K, while temperatures before sunrise are

underestimated by up to 2.5 K. The resulting misfit is systematically different from the effect of unknown emissivity shown in Fig. 4.4. Note also that a different best fitting single thermal inertia is found for each filter, and the derived values are summarized in Tab. 4.2.

If thermal inertia differs sufficiently between the units in the instrument's field of view, the fact that the observed brightness temperature curve cannot be modeled using a single thermal thermal inertia can now be used to disentangle the unit's individual contributions to the observed flux. Results of these calculations are presented in the following, assuming the emissivity to be constant and equal to 0.9 in all filters. Moreover, it is assumed that the area fractions of different units are known from the images of the MASCOT camera MasCam. Besides the 75/25-mixture of regolith mentioned above we simulate a surface that is equally covered by fine-grained and coarse-grained material, again using $\Gamma = 650$ Jm^{-2}K^{-1}s$^{-1/2}$ and $\Gamma = 50$ Jm^{-2}K^{-1}s$^{-1/2}$ respectively.

As surface emissivity is generally unknown, the sensitivity of the inversion results on emissivities different from the $\varepsilon = 0.9$ case used to generate the MARA signal has also been investigated. Here we limit our study to varying the assumed emissivity from 0.85 to 0.95 in three steps, as this range reasonably bounds the expected in-situ values.

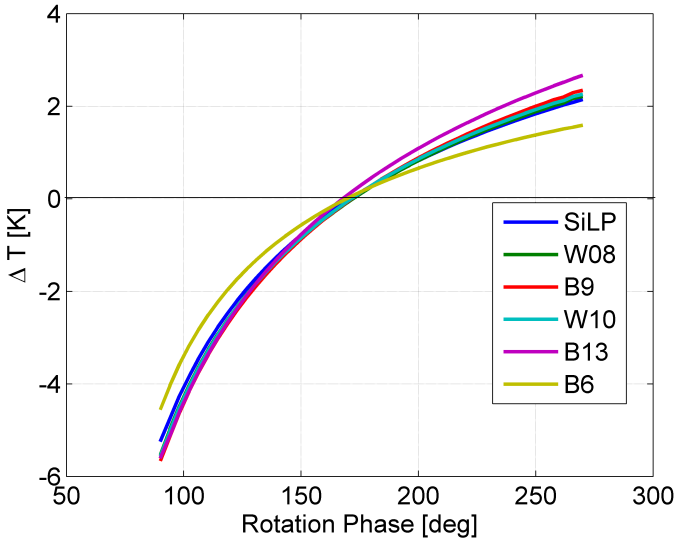

Figure 4.7: Brightness temperature misfit between the temperature curves for the heterogeneous surface and a model assuming a single thermal inertia. Results are shown as a function of rotation phase for the six MARA filters. For each filter, a single best fitting thermal inertia (compare Tab. 4.2) has been used to derive the model misfit.

After synthesizing MARA measurements for the given setup (Sec. 4.2.3), admissible thermal inertia combinations are determined using a grid search with Γ varying in steps of 2 Jm^{-2}K^{-1}s$^{-1/2}$ from $2 - 150$ and $550 - 750$ Jm^{-2}K^{-1}s$^{-1/2}$. As before, χ^2-values are

then calculated for each combination of thermal inertias and all parameters yielding a χ^2 outside of $\Delta\chi^2 = 14.8$ are discarded. χ^2-values are calculated for all MARA channels, and parameters are required to be admissible in all channels simultaneously. Unlike the case of a homogeneous surface, this reduces the range of admissible thermal inertia combinations compared to fitting just one filter. The reason is that each filter observes a different section of the spectrum and the B6 filter will for example be more sensitive to higher temperatures, which are encountered for the 650 $\mathrm{Jm^{-2}K^{-1}s^{-1/2}}$ surface during nighttime. The results of the parameter retrieval are shown in Fig. 4.8 where the color scale of the $\Delta\chi^2$-values of admissible parameter combinations has been chosen to represent averaged $\Delta\chi^2$ over all channels.

For equal area coverage, the retrieved thermal inertias range from $\Gamma_1 = 580$ to 736 $\mathrm{Jm^{-2}K^{-1}s^{-1/2}}$ and $\Gamma_2 = 32$ to 76 $\mathrm{Jm^{-2}K^{-1}s^{-1/2}}$, respectively, while in the 75/25-case we have $\Gamma_1 = 590$ to 722 $\mathrm{Jm^{-2}K^{-1}s^{-1/2}}$ and $\Gamma_2 = 8$ to 126 $\mathrm{Jm^{-2}K^{-1}s^{-1/2}}$, respectively. As is evident from the figure, the emissivity uncertainty of ± 0.05 represents a substantial contribution to the thermal inertia uncertainty, and it is considerably larger than the uncertainty caused by surface heterogeneity alone, which is expressed by the size of the individual error ellipses for a given fixed ε. For example $\Gamma_1 = 650^{+42}_{-40}$ $\mathrm{Jm^{-2}K^{-1}s^{-1/2}}$ and $\Gamma_2 = 50^{+10}_{-8}$ $\mathrm{Jm^{-2}K^{-1}s^{-1/2}}$ would be admissible for the equal area case if $\varepsilon = 0.9$ would be considered only. Also note that Fig. 4.8 confirms that an overestimated emissivity results in a systematically lower retrieved thermal inertia and vice versa (c.f. Figs. 4.5 and 4.3).

It is worth pointing out that the uncertainty of the retrieved Γ depends on the area coverage of the respective units, as large area fractions correspond to larger contributions to the measured signal. Therefore, thermal inertia of the dominant unit in the field of view can be retrieved with higher confidence. Furthermore, higher retrieved thermal inertias have intrinsically larger uncertainty, because the influence of thermal inertia on surface temperature and emitted flux is non-linear and more pronounced for smaller values of Γ. In the above examples, the thermal inertia contrast between the two surface units is chosen to be quite large, and it should be noted that the magnitude of the systematic distortion of the diurnal temperature curve strongly depends on surface properties. Ultimately, the ability to distinguish between different units will be limited by the measurement uncertainties and differences can vanish within these uncertainties. We found that for mid-range thermal inertia values of 100 to 500 $\mathrm{Jm^{-2}K^{-1}s^{-1/2}}$, the thermal inertias of two units have to differ by at least 300 $\mathrm{Jm^{-2}K^{-1}s^{-1/2}}$ for a single-thermal inertia fit to fail. This difference would need to be even larger at high thermal inertia values since the difference between the diurnal temperate curves further decreases in this case (Keihm et al., 2015).

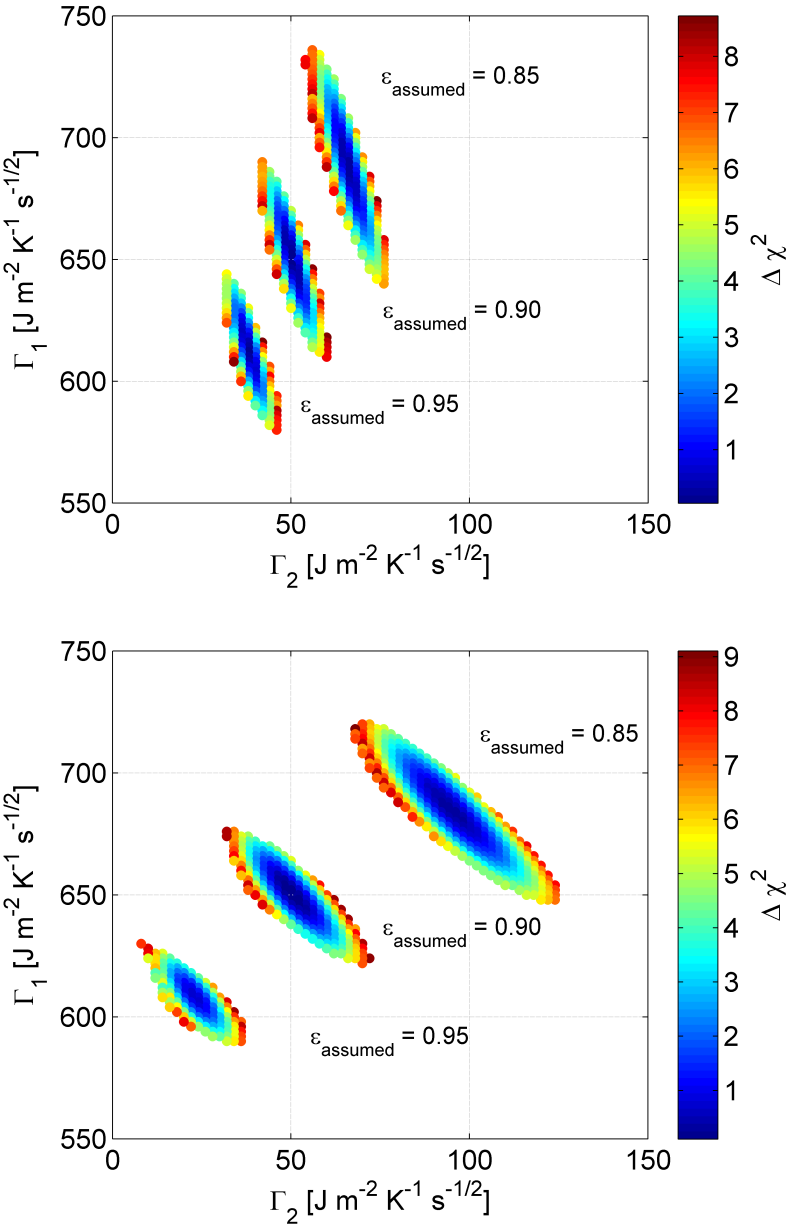

Figure 4.8: Color coded $\Delta\chi^2$ misfit as a function of retrieved thermal inertias $\Gamma_{1,2}$ indicating the range of acceptable parameters for three different emissivities. The observed surface was assumed to be partially covered by fine-grained and coarse-grained material with $\Gamma = 50$ and 650 $\mathrm{Jm^{-2}K^{-1}s^{-1/2}}$, respectively. Top: Surface area covered equally by both units. Bottom: Surface covered to 75% with coarse grained material.

4.4 SUMMARY AND CONCLUSIONS

In this paper we present a method to constrain regolith surface properties from surface brightness temperature measurements using the MARA instrument, which is a payload on the MASCOT asteroid lander of the Hayabusa2 mission to the C-type asteroid (162173) Ryugu (Grott et al., 2017). To estimate inversion uncertainties, synthetic MARA signals are generated using an asteroid thermophysical model, from which surface temperatures are derived. These are then used as input to generate synthetic MARA signals and instrument uncertainties as determined during calibration (ibid.) is included. Given the synthetic signals, the range of admissible surface properties is determined by recalculating observed signals for different surface property combinations, and the misfit between the different models is determined. Only those parameter combinations for which the misfit is within a critical range are then determined to be admissible, and respective uncertainty ranges are derived.

Given a homogeneous, gray-body ($\varepsilon(\lambda)$ = const.) surface within the instrument's field of view and assuming measurement uncertainty levels as appropriate for MARA, thermal inertia can be retrieved with high accuracy. For the case studied here ($\Gamma = 250$ $\mathrm{Jm^{-2}K^{-1}s^{-1/2}}$), thermal inertia can be determined to 6 %. The range of admissible parameter combinations decreases with increasing signal-to-noise ratio, and the silicon long pass and the W10 filter are found to best constrain surface properties. Contrary to other approaches for thermal inertia determination (e.g., Putzig et al., 2007), emissivity is fit simultaneously with thermal inertia, and ε can be constrained to 6 %. It is worth pointing out that the common assumption $\varepsilon = 1$ systematically underestimates the kinetic temperature. For nighttime measurements this leads to underestimated Γ, resulting in an error of up to 40 $\mathrm{Jm^{-2}K^{-1}s^{-1/2}}$ for the case studied here. For daytime measurements the thermal inertia would be overestimated.

If emissivity is allowed to vary as a function of wavelength, the spectral slope of the target surface could be retrieved. Uncertainties of $\varepsilon(\lambda)$ depend on the considered filter, but are generally of the order of 5 - 7 %. A change of ε by 5 % leads to temperature offsets of up to 3-5 K, well higher than the uncertainty of the temperature measurement, which is 1 - 1.5 K.

To apply this method, surface emissivity averaged of the full spectrum and weighted by the Planck function is needed as an input for the thermal model but this information is not usually available. However, this can be obtained by an iterative approach using the results of the first emissivity inversion as input for the TPM.

In the second part of our study we analyze the influence of surface heterogeneity on the retrieved thermal inertia, and the influence of area coverage, varying thermal inertia, as well as unknown emissivity are investigated. Contrary to the homogeneous surface, the presented approach for heterogeneous surfaces does not fit emissivity independently. Rather, we chose to absorb the uncertainty of unknown emissivity in the total error budget to reduce the amount of fitting parameters. Results show that

multiple thermal inertias for different units can be retrieved if respective area fractions for the units are known. Uncertainties depend on the thermal inertia contrast as well as area fraction coverage of a given unit. In addition, emissivity significantly influences the results, and again an anti-correlation between assumed emissivity and retrieved thermal inertia is found.

Summarizing our study, we retrieve the thermal inertia of a homogeneous surface with flat spectrum within 250 $\pm$16 $Jm^{-2}K^{-1}s^{-1/2}$, while the emissivity uncertainty is below 6 %. This corresponds to a grain size range of 24 - 32 mm assuming a porosity of 50 % and using the thermal conductivity model of Sakatani et al. (2017). For a heterogeneous surface covered by equal area fractions of fine-grained and coarse-grained material, we retrieve thermal inertias 658 $\pm$78 and 54 $\pm$22 $Jm^{-2}K^{-1}s^{-1/2}$ corresponding to grain sizes of 100 - 165 mm and 800 ¯m - 5 mm for the coarse and fine-grained material respectively.

A potential improvement of the above approach for analyzing on-asteroid data could be to attempt a three-parameter fit, trying to determine $\Gamma_{1,2}$ as well as ε simultaneously. The two broadband filters W10 and SiLP would then be used to constrain the thermal inertia for a set of assumed average emissivities, and emissivities in the other four channels would then be constrained using these thermal inertia combinations, looking for a global minimum. If the observed regolith consists of very fine grains, one should consider different emissivities for the low and high thermal inertia terrains (e.g. Maturilli et al. (2008)) but this effect is expected to be small for the larger grain sizes predicted for Ryugu.

This study assumes a nominal MASCOT landing on a flat surface, but the influence of local slope needs to be included for mission data analysis. The east-west tilt will determine local time, and the more the surface is tilted towards the east, the earlier the sun will rise above the horizon and illuminate the surface. The north-south slope will effectively change the latitude, therefore determining the day to night ratio. During MASCOT descent both MasCam and the Hayabusa2 cameras will observe the surface to localize the lander, and we will use a detailed asteroid shape model to determine the local tilt and illumination conditions.

The issue of being unable to fit observed brightness temperature curves using a single thermal inertia has been discussed before, and models fitting the observed signal to heterogeneous surfaces were implemented for Mars (Fergason et al. (2006b), Putzig et al. (2007), and Vasavada et al. (2017). Similar to the approach presented here, Fergason et al., 2006b used full diurnal temperature curves from the MER rover's miniTES instrument together with camera images to determine thermal inertia of rocks and sands in the field of view. Vasavada et al. (2017) used the Curiosity rover's REMS GTS to analyze surface thermophysical properties, and their model included vertical layering of material, considering dust on top of rocks or cemented crusts on top of loose material. Vasavada et al. (ibid.) found similar effects for vertical layering as we did for horizontal heterogeneity, indicating that a signal generated by a vertically heterogeneous surface

returns ill-fitting single thermal inertia models. Therefore, including layering may be necessary for interpreting MARA data, depending on what is observed during the on-asteroid mission.

An approach similar to the one presented here is the spectral rock abundance method (Bandfield et al., 2011; Nowicki et al., 2007), which uses observations of the surface at one point in time at multiple wavelengths to calculate the area fractions of rocks and fines. While thermal inertia for the rocks is assumed to be known, the rock abundance and thermal inertia of the fines are determined by the method. In contrast, we know the areal rock abundance from camera images and retrieve the thermal inertia of both rock and fines. Also, as shown above, using a single filter is sufficient to retrieve both thermal inertias if observations are not restricted to a single local time.

Another application of the presented model may be modeling telescopic, disk-integrated (unresolved) observations of asteroids, as the heterogeneous surfaces present on these bodies will generate observational bias similar to what has been investigated here. However, resolved optical images are necessary to apply the above method, which limits the range of applicability to those asteroids which have been visited by spacecraft. A case study could be asteroid (25143) Itokawa, for which remote sensing as well as in-situ data is available. For Itokawa, Müller et al. (2014) found a global thermal inertia of 700 ± 200 $\mathrm{Jm^{-2}K^{-1}s^{-1/2}}$, and Gundlach et al. (2013) determined a mean grain size of 1-2 cm using 750^{+50}_{-300} $\mathrm{Jm^{-2}K^{-1}s^{-1/2}}$. Yet, only 20 % of the surface is covered by centimeter-sized grains, whereas 80 % of the surface of Itokawa is covered by much coarser material (Saito et al., 2006). In the rough terrain one finds pebbles of tens of centimeters up to meter-sized boulders (Miyamoto et al., 2007), and a dominant particle size of 1-2 cm appears to be inconsistent with the image data. Therefore, it may be interesting to reanalyze the infrared observations of Itokawa, taking the presence of different geological units into account. Furthermore, the availability of a detailed shape model for Itokawa could also help to reduce ambiguities. Taken together, a reanalysis of the available data could provide a more accurate estimate of the thermal inertia for the rough material fraction, which appears to have a thermal inertia lower than estimates for bulk rock despite being much larger than the diurnal skin depth of Itokawa of about 1 cm (Müller et al., 2014).

4.5 ACKNOWLEDGMENTS

We thank the two anonymous reviewers for their very constructive suggestions and comments. The MASCOT lander on the Hayabusa2 Mission of JAXA is a DLR/CNES cooperation. MASCOT MARA has been developed and built under the leadership of the DLR Institute of Planetary Research with contracted contributions from the Institute of Photonic Technology. The Hayabusa2 Mission is operated by JAXA.

5

LATITUDINAL DEPENDENCE OF ASTEROID REGOLITH FORMATION BY THERMAL FATIGUE

Maximilian Hamm[a] (corresponding author), Hiroki Senshu[b], Matthias Grott[a]
[a]*German Aerospace Center (DLR), Insitute of Planetary Research, Rutherfordstr. 2, 12489 Berlin, Germany*
[b] *Chiba Institute of Technology, Planetary Exploration Research Center, Narashino, Japan*
Published in Icarus, Volume 319, February 2019, Pages 308-311
https://doi.org/10.1016/j.icarus.2018.09.033

ABSTRACT

The latitudinal dependence of regolith formation by thermal fatigue is studied for variable solar declination and surface thermal inertia. We find that regolith generation takes place in a surprisingly wide band around the equator and make predictions for the regolith distribution on the target asteroids of the upcoming Hayabusa2 and OSIRIS-REx missions.

5.1 INTRODUCTION

The surface of asteroids consists of broken-up material called regolith, with constituent sizes varying from boulders to fine dust grains. Visiting spacecraft have characterized the texture of regolith covers in great detail, and a wealth of data has been returned from, e.g., Itokawa (Yano et al., 2006), Vesta (Jaumann et al., 2012), and Eros (Thomas et al., 2001). To understand the nature of the processes shaping these surfaces, it is crucial to understand the process of regolith formation, as it sets the stage for any subsequent surface evolution through, for example, regolith migration (Garcia et al., 2015). Recent studies have shown the importance of thermal fatigue as a regolith forming process (e.g. Eppes et al., 2015; Molaro et al., 2015, 2017; Viles et al., 2010), which could erode the surface faster than micrometeoroid impacts (Delbo et al., 2014; Dombard et al., 2010). However, the efficiency of this process as a function of latitude, solar declination and surface thermal inertia has not been well characterized to date.

Thermal fatigue describes the cracking and chipping of rocks by thermal stresses (e.g. Luque et al., 2011; Viles et al., 2010) and it results in the generation of fragments of ever decreasing size. Studies investigating thermal stresses in objects exposed to the space environment include comets (Auger et al., 2018; Kührt, 1984), meteoroids (Čapek et al., 2010, 2012), boulders (Molaro et al., 2017) and granular microstructures (Molaro

et al., 2015), and thermal fatigue is sometimes parameterized in terms of spatial or temporal temperature gradients (e.g. Auger et al., 2018; Molaro et al., 2017). However, while macroscopic temperature gradients can add to thermal fatigue on a macroscopic scale, the different thermal expansion of constituents can induce thermal fatigue on the microscopic scale, i.e. the individual grains constituting a boulder (Molaro et al., 2015). Molaro et al., 2015, 2017 demonstrated that in both cases the amplitude of the diurnal temperature wave is a more suitable proxy for the thermally induced breakdown of regolith.

This work will investigate the spatial distribution of thermal forcing on the target body rather than an actual thermo-mechanical fatigue model. The purpose is to understand the regolith distribution on a global scale rather than the breakdown of individual boulders. We assume that if thermal fatigue occurs at all, it will be strongest where the thermal forcing is strongest. To this end, we calculate the latitudes with the largest amplitude of the diurnal temperature curve as a representation of thermal stress. Results will show how these latitudes of maximum forcing change with thermal inertia and solar declination. We will then relate the results to C-type asteroid (162173) Ryugu, the target of the Hayabusa-2 mission (Müller et al., 2017; Tsuda et al., 2013), as well as B-type asteroid (101955) Bennu, the target of the OSIRIS-Rex mission (Lauretta et al., 2015).

5.2 THEORY AND METHODS

We calculate temperature profiles on a sphere solving the one-dimensional heat conduction equation for a homogeneous half-space using an explicit finite differences scheme (Takita et al., 2017). Temperatures are calculated on a grid with 250 nodes in depth for latitudes and longitudes varying in steps of one degree. The sphere is assumed to rotate with a period of 7.63 h and is placed at a fixed solar distance of 1.2 AU, corresponding to the rotational and orbital parameters of (162173) Ryugu (Müller et al., 2017). The influence of thermal inertia Γ and solar declination δ on the diurnal temperature amplitudes ΔT is calculated by studying their influence on the surface energy balance given by

$$-\Gamma\sqrt{\frac{\pi}{P}}\frac{\partial T}{\partial z} = (1-A)I - \sigma\varepsilon T^4 \tag{5.1}$$

where P is the rotation period, A is albedo, σ the Stephan-Boltzmann constant, ε the emissivity, and z the depth normalized to the diurnal skin depth. It is worth noting that while we fix the rotational period to that of (162173) Ryugu in the following, Eq. 5.1 implies that the effects of rotation period and thermal inertia can compensate each

other. Therefore, results presented below can be scaled to other rotation periods by adjusting the chosen thermal inertia. Insolation I is given by

$$I(t) = \frac{I_0}{r_h^2}(\cos\phi\cos\delta\cos\psi(t) + \sin\phi\sin\delta) \tag{5.2}$$

where $I_0 = 1366.1\mathrm{W/m^2}$ is the solar constant at $1AU$, r_h is heliocentric distance, δ is solar declination, and ϕ is latitude with $\phi = 0$ at the equator. The local hour angle $\psi(t) = \omega t$ changes with time as the asteroid rotates and noon is defined by $\psi(t = 0) = 0$. During nighttime I is set to zero.

The amplitude of the diurnal temperature variations is defined by $\Delta T = \frac{1}{2}(T_{max} - T_{min})$, where T_{max} and T_{min} are the maximum and minimum diurnal temperatures at the given location. The temperature rise during daytime is larger and faster than the cooling during the night, and the amplitude ΔT is thus generally dominated by the daytime temperature rise. It tends to increase towards the subsolar point $\phi = \delta$, where the maximum illumination

$$I_{max} = \frac{I_0}{r_h^2}\cos(\phi - \delta) \tag{5.3}$$

occurs. However, the length of the night remains a limiting factor. The larger the solar declination δ, the further north the sub-solar point and the shorter is the night, limiting the cooling of the surface. Due to the cosine dependence of the maximum illumination on the angle $\phi - \delta$, I_{max} changes only slowly near the subsolar point, but the length of the night sharply increases away from $\phi = \delta$. Consequently, the minimum diurnal temperature decreases towards lower latitudes, and ΔT reaches its maximum south of the subsolar latitude for δ larger than a critical value, ultimately limited by the boundary latitude of permanent insolation at $\phi = 90^\circ - \delta$. Surfaces with high thermal inertia Γ react delayed to insolation changes, and large Γ reduces heating and cooling rates, which reduces the influence of short nights. Therefore, the amplitudes of the diurnal temperature curve ΔT will decrease with increasing Γ, and high Γ will shift the latitude of maximum amplitude towards higher latitudes.

5.3 RESULTS

In the following, we will investigate the location of maximum temperature amplitude ΔT as a function of solar declination δ and thermal inertia. While solar declination will be varied between 0° and 85°, thermal inertia will be varied between 500 and 3000 $\mathrm{Jm^{-2}K^{-1}s^{-1/2}}$. These values cover the expected range of thermal inertia for various meteorites, ranging from 640 $\mathrm{Jm^{-2}K^{-1}s^{-1/2}}$ for CM2 chondrites to 3000 $\mathrm{Jm^{-2}K^{-1}s^{-1/2}}$ for E4 chondrites (Opeil et al., 2010). Non-chondritic materials like serpentine or enstatite also fall within this range. We choose the thermal inertia values to represent

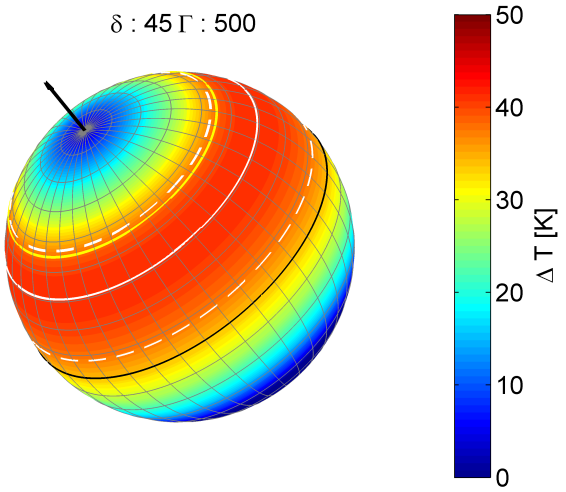

Figure 5.1: Amplitudes of diurnal temperature curves for a solar declination of $\delta = 45°$, and a thermal inertia of $\Gamma = 500\,\mathrm{Jm^{-2}K^{-1}s^{-1/2}}$. The yellow line corresponds to the subsolar point $\phi = \delta$. The latitude of the maximum amplitude is represented by a solid white line, the dashed white lines indicate the latitude where $\Delta T = 0.9\Delta T_{max}$, and the solid black line represents the equator.

bulk material instead of unconsolidated material, as we want to estimate where thermal fatigue would be most likely to breakdown consolidated surface material.

As an example, the latitudinal distribution of temperature amplitudes ΔT is illustrated in Fig. 5.1, where a solar declination of $\delta = 45°$ and a thermal inertia of $\Gamma = 500\,\mathrm{Jm^{-2}K^{-1}s^{-1/2}}$ have been assumed. The solid black line represents the equator and the subsolar latitude $\phi = \delta$ is indicated by the yellow line. The latitude ϕ_{max} of the maximum ΔT is represented in Fig. 5.1 by a solid white line. The dashed white lines represent the latitudes where 90 % of the maximum ΔT is reached, and these span a band of about $\pm 20°$ in latitude. This should correspond to the region in which most of the thermal fatigue can be expected, and it covers a significant fraction of the northern hemisphere. The 90 % band is truncated in the north by the line of permanent insolation, which for $\delta = 45°$ coincides with the subsolar latitude. It is worth noting that for low solar declination, the 90 % band widens to up to $\pm 30°$, while for large δ the band can narrow down to $\pm 5°$. Furthermore, large thermal inertia Γ would also cause slightly narrower bands (not shown).

Results for the entire range of considered parameters are shown in Fig. 5.2, which shows the maximum latitude ϕ_{max} for the diurnal temperature amplitude as a function of solar declination δ and thermal inertia Γ. The subsolar latitude $\phi = \delta$ as well as the

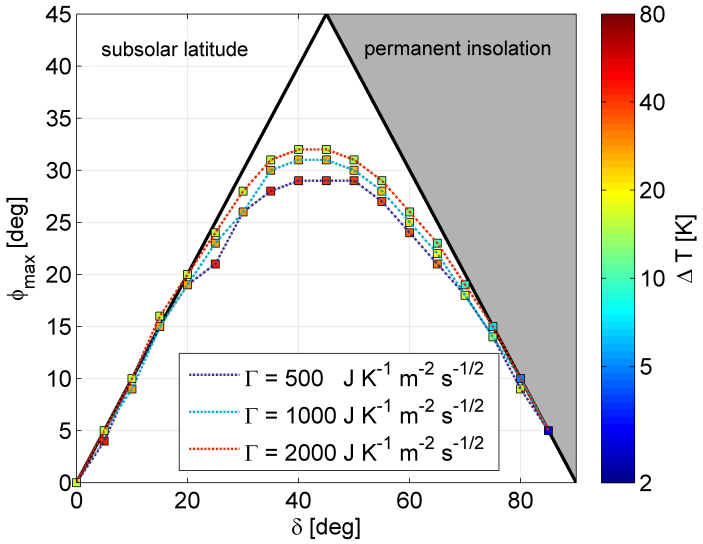

Figure 5.2: Latitude ϕ_{max} of the maximum diurnal temperature amplitude ΔT_{max} as a function of solar declination δ and thermal inertia Γ. The color indicates the magnitude; the grey area indicates the latitudes with permanent insolation depending on solar declination. Results for $\Gamma = 3000$ Jm^{-2}K^{-1}s$^{-1/2}$ are not shown since they are indistinguishable from $\Gamma = 2000$ Jm^{-2}K^{-1}s$^{-1/2}$

area of permanent insolation are indicated for reference and the magnitude of ΔT_{max} is shown in color. As expected, ΔT_{max} is larger for lower δ and Γ.

The latitude ϕ_{max} of maximum temperature amplitude closely follows the subsolar latitude up to $\delta = 30°$. From there on, the increase of ϕ_{max} flattens, reaching its maximum of 29° to 32° at $\delta = 45°$. For larger solar declination ϕ_{max} decreases again, following the boundary of permanent insolation in accordance with the theoretical expectations discussed in Section 5.2. It is worth noting that ϕ_{max} is almost independent of Γ which has its strongest influence at solar declinations close to 45°, where the cooling rate is most significant due to the short night as discussed in Section 5.2.

5.4 CONCLUSIONS

The amplitude of the diurnal variation of the surface temperature can drive thermal fatigue on asteroids, and we have calculated thermophysical models for C-type asteroid (162173) Ryugu to determine the latitudes at which the diurnal temperature amplitudes become maximal. These are assumed to be representative for thermal stresses on the macroscopic and microscopic scales. The presented work encompasses a broad range of pole orientations and regolith compositions. Furthermore, Eq. 5.1 implies

that our results can be applied to other rotation periods by scaling the thermal inertia appropriately.

The thermal stress field is a superposition of contributions from microscopic and macroscopic stresses, which in turn are to first order proportional the temperature amplitude (Molaro et al., 2015, 2017; online methods Delbo et al., 2014). However, stress concentrations will occur at cracks or exposed parts of boulders (Molaro et al., 2015) such that a global simulation of thermal fatigue would require detailed assumptions concerning boulder size and topography. These are generally not available prior to visiting spacecraft observations. Instead, we focused on the global trend in regolith formation by thermal fatigue.

If thermal fatigue occurs at all, it will be strongest where the strongest forcing occurs, and it has been a common assumption that this is the case around the equator. However, we identify subsolar latitude, i.e. solar declination, length of night, and thermal inertia as factors determining the latitude of maximum forcing, which does not necessarily coincide with the equator. Furthermore, as the asteroid orbits the sun, solar declination changes from its maximum on one hemisphere to its minimum on the opposite hemisphere depending on the tilt of the rotational axis. The spot of maximum thermal forcing therefore oscillates around the equator inducing regolith breakdown in a latitudinal band around that spot. This band is not sharply defined as the maximum of the temperature amplitude is relatively flat, and 90% of the forcing occurs within bands of $\pm 10^\circ$ to $\pm 30^\circ$ around the latitude of maximum forcing. Thus, we find that 90% of the forcing can occur in surprisingly large parts of the surface. In particular, it implies that even for a very high obliquity thermal fatigue should be strongest at, but not limited to, the equator.

This is in agreement with spacecraft observations of asteroids like, e.g., the surface of asteroid (4) Vesta, which shows ponds of fine material that are distributed between $+30^\circ$ and -10° (Jaumann et al., 2012). On S-type asteroid (433) Eros, fine regolith is also located in circular ponds in a $\pm 30^\circ$ band around the equator (Robinson et al., 2001). These ponds also contain boulders that were scattered over the surface by a large impact (Thomas et al., 2001) and which were subsequently eroded by thermal stress and formed fine regolith aprons around them (Dombard et al., 2010). Thermal fatigue is not necessarily limited to these craters, but it could be more efficient there as the impact created a damage zone in the surface material, thus locally lowering thermal inertia.

The eccentricity of an asteroid's orbit causes asymmetry between the northern and southern hemispheres as thermal fatigue will be stronger at perihelion. As a result, the boulders would be more degraded on one hemisphere compared to the other if the spin axis is tilted with respect to the orbital plane. Contrarily, if the spin axis is almost perpendicular to its orbital plane, as suspected for (101955) Bennu (Lauretta et al., 2015) the subsolar latitude will remain close to the equator during the entire orbit, and a particle-size dichotomy would not be expected.

Our results imply that thermal fatigue should be much less effective at the poles or in the near-polar regions between 90° and 70°. However, regolith migration and orbital evolution could obscure the regolith distribution pattern originally induced by thermal fatigue. Regolith migration could on the one hand transport fine regolith to higher latitudes, but on the other hand fast spinning asteroids could transport regolith towards the equator forming an equatorial bulge as proposed for (101955) Bennu (Scheeres, 2015). In both cases, regolith formation could be decoupled from the observed regolith distribution to some extent. Furthermore, a change of the orientation of the rotational axis would change the location of regolith formation on evolutionary time scales, such that fine regolith could be formed by thermal fatigue at locations not predicted for the observed axis orientation. An example could be the fine regolith that is present close to the poles on S-type asteroid (25143) Itokawa, where it seems likely that material was transported to high latitudes (Miyamoto et al., 2007).

The upcoming asteroid sample return missions Hayabusa2 (Tsuda et al., 2013) and OSIRIS-Rex (Lauretta et al., 2015) will provide the opportunity to observe the morphology and thermal environment of asteroids (162173) Ryugu and (101955) Bennu in-situ. Both asteroids are expected to consist of chondritic material, and while the thermal inertia of Ryugu will be estimated using a radiometer on the MASCOT lander (Grott et al., 2017; Hamm et al., 2018) as well as the Hayabusa2 orbiter's thermal infrared imager (Okada et al., 2017), Bennu's thermal inertia will be observed by OSIRIS-REx' thermal emission spectrometer (Christensen et al., 2018). Estimates of the thermal inertia will allow for deriving global maps of grainsizes (Sakatani et al., 2017; Takita et al., 2017), and the combined observations of morphological features, grainsizes, and returned samples will provide new insights into the regolith formation process on these bodies. This will enable a comparison with the theoretical predictions presented here.

5.5 ACKNOWLEDGMENTS

This work has been supported by the JSPS Summer Program 2017, grant number SP17305. We thank the two anonymous reviewers for their helpful, constructive contributions.

6

LOW THERMAL CONDUCTIVITY BOULDER WITH HIGH POROSITY IDENTIFIED ON C-TYPE ASTEROID (162173) RYUGU

M. Grott[1], J. Knollenberg[1], M. Hamm[1], K. Ogawa[2], R. Jaumann[1], K. Otto[1], M. Delbo[3], P. Michel[3], J. Biele[4], W. Neumann[5], M. Knapmeyer[1], E. Kührt[1], H. Senshu[6], T. Okada[7], J. Helbert[1], A. Maturilli[1], N. Müller[1], A. Hagermann[8], N. Sakatani[7], S. Tanaka[7], T. Arai[9], S. Mottola[1], S. Tachibana[10], I. Pelivan[11,12], L. Drube[1], J.-B. Vincent[1], H. Yano[7], C. Pilorget[13], K. D. Matz[1], N. Schmitz[1], A. Koncz[1], S. Schröder[1], F. Trauthan[1], M. Schlotterer[14], C. Krause[4], T.-M. Ho[14], A. Moussi-Soffys[15]

[1]German Aerospace Center (DLR), Berlin, Germany, [2]Department of Planetology, Graduate School of Science, Kobe University, Kobe, Japan, [3]Université Côte d'Azur, Observatoire de la Côte d'Azur, CNRS, Laboratoire Lagrange, Nice, France, [4]German Aerospace Center (DLR), Cologne, Germany, [5]Institut für Planetologie, University of Münster, Münster, Germany, [6]Planetary Exploration Research Center, Chiba Institute of Technology, Narashino, Japan, [7]Institute of Space and Astronautical Science, Japan Aerospace Exploration Agency, Sagamihara, Japan, [8]University of Stirling, Stirling, UK, [9]Division of System and Information Engineering, Ashikaga University, Tochigi, Japan, [10]UTokyo Organization for Planetary and Space Science, University of Tokyo, Japan, [11]Institute of Mathematics, University of Potsdam, Germany, [12]Fraunhofer Heinrich Hertz Institute (HHI), Berlin, Germany, [13]Institut d'Astrophysique Spatiale, Université Paris Sud, Orsay, France, [14]German Aerospace Center (DLR), Bremen, Germany, [15]Centre National d'Etudes Spatiales (CNES), France

Published in Nature Astronomy, 15 July 2019
https://doi.org/10.1038/s41550-019-0832-x

6.1 ABSTRACT

C-type asteroids are among the most pristine objects in the solar system, but little is known about their interior structure and surface properties. Telescopic thermal infrared observations have so far been interpreted in terms of a regolith covered surface with low thermal conductivity and particle sizes in the centimeter range. This includes observations of C-type asteroid (162173) Ryugu (Gundlach et al., 2013; Sakatani et al., 2017; Wada et al., 2018). However, upon arrival of the Hayabusa2 spacecraft at Ryugu, a regolith cover of sand- to pebble-sized particles was found to be absent (Jaumann et al., 2019; Sugita et al., 2019). Rather, the surface is largely covered by cobbles and boulders, seemingly incompatible with the remote sensing infrared observations. Here we report on the first in-situ thermal infrared observations of a boulder on a C-type asteroid. We found that the boulder's thermal inertia was much lower than anticipated

based on laboratory measurements of meteorites, and that a surface covered by such low conductivity boulders would be consistent with remote sensing observations. Our results furthermore indicate high boulder porosities as well as a low tensile strength in the few hundred kPa range. The predicted low tensile strength confirms the suspected observational bias (Flynn et al., 2018) in our meteorite collections, as such asteroidal material would be too frail to survive atmospheric entry (Popova et al., 2011).

6.2 LETTER

On October 3rd, 2018, the Hayabusa2 spacecraft (Watanabe et al., 2017) delivered the MASCOT (Ho et al., 2017) (Mobile Asteroid Surface Scout) lander to the surface of asteroid (162173) Ryugu, where MASCOT's infrared radiometer MARA (Grott et al., 2017) obtained surface brightness temperature measurements for a full day-night cycle. The instrument's field of view covered a spot of approximately 10 cm in diameter on the surface, which was also observed by MASCOT's optical camera MasCam (Jaumann et al., 2019). The scene observed by MARA and MasCam(ibid.) is shown in Figure 6.1, with the footprint of the MARA 8-12 µm broadband sensor indicated in red. MARA is viewing the top face of a slightly raised (∼3 cm) boulder in front of MASCOT. The boulder is rough in surface texture at the sub-centimeter scale and generally appears angular to sub-angular. Particles with diameters larger than 0.6 mm are resolvable at the bottom of the image (∼0.2 mm per pixel resolution), but only a few separate roundish grains can be identified as loose grains on this formation. Furthermore, an optically thick cover of fine particles is not observed, and bright inclusions are visible at multiple locations including the area viewed by MARA. Highly resolved areas in the MasCam image show that the boulder is composed of a relatively dark matrix with mostly bright but also darker inclusions at the millimeter scale (ibid.).

Remote spectral observations of Ryugu suggest a composition similar to heated CM (CM2) or CI meteorites (Moskovitz et al., 2013). However, the texture observed in close-up images (compare Fig. 6.1) shows millimeter-sized inclusions in at least one location and bright speckles at varying distances. This seems to be incompatible with a CM2 composition, for which petrographic analysis (King et al., 1978) shows maximum grain sizes around 0.2 mm. On the other hand, CI meteorites are predominantly composed of a fine-grained matrix with a mottled appearance, and the texture observed by MASCOT resembles that of the rare CI2 Tagish Lake meteorite, which possesses up to 2 mm large calcium aluminum rich inclusions (Brown et al., 2000). Thus, CI2 type meteorites appear to be the closest known Ryugu analogue. However, as Tagish Lake is a rare sample and variations in inclusion sizes are common for carbonaceous chondrites, it is not feasible to derive a definite meteorite analogue. Rather, it may be possible that the investigated boulder is not represented in any meteorite collection on Earth.

Temperatures measured using MARA's 8-12 µm filter are shown as a function of local time in Figure 6.2a along with the best-fitting thermal models taking the illumination

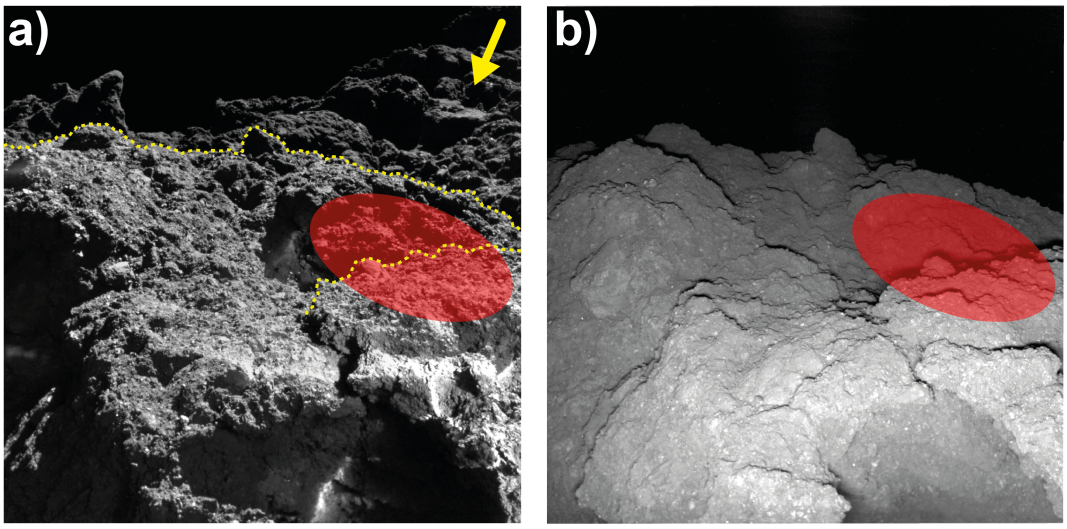

Figure 6.1: MasCam Image of the boulder observed by MASCOT indicating the MARA field of view (red shaded area). a) The location in daylight (local time 9:20) with the yellow arrow indicating the approximate direction of illumination with sun elevation and azimuth at 40.2° and 67.2°. The image suggests that MASCOT is located in front of an angular to sub-angular formation whose edges are outlined by the yellow dotted line. The yellow dashed line indicates the edge of an elevated part of the boulder (compare the nighttime image on the right). The front face of the formation orientated towards MARA is approximately 3 cm above the plane MASCOT is located on. b) The same location at night (local time 23:18) illuminated by the camera's red LED. Only the foreground is visible due to the limited illumination provided. The images are distorted with pixel resolutions varying between approximately 0.2 mm at the bottom and 3 mm near the horizon. Note that due to a minor relocation of MASCOT the scene in panel b) is slightly shifted towards the left with respect to panel a)

conditions at the landing site as well as surface roughness into account (see methods). Diurnal temperatures rise steeply in the morning, but start dropping around 11:07 local time, indicating shadows passing through the radiometer field of view before noon. Maximum temperatures reach 302 K shortly after local noon and the sun sets at 16:39 local time. The complex shape of the daytime temperature curve indicates a rough surface, consistent with camera observations. During nighttime, temperatures drop to 205 K.

As daytime data is affected by surface roughness and re-radiation from the environment, only equilibrated nighttime temperatures are used to fit thermophysical models. Best-fitting models (see methods) are indicated in Figure 6.2a and correspond to a thermal inertia (Γ) of 282 $\mathrm{J\,m^{-2}\,K^{-1}\,s^{-1/2}}$. While fitting nighttime data perfectly, the steep increase of temperature during the morning is underestimated, while midday temperatures are overestimated. Taking surface roughness into account (green solid

line in Figure 6.2a), the quality of the fit to midday temperatures is much improved, but early morning temperatures cannot be fit using this model. The latter are influenced by light reflected from the MASCOT lander, and a local terrain model including reflections would be necessary to improve results. Nevertheless, since only equilibrium nighttime temperatures are used to estimate the thermal inertia Γ, presented results are largely independent of surface roughness and topography.

Admissible thermal inertia values are shown as a function of maximum insolation in Figure 6.2b, where the orientation of the surface normal has been systematically varied around its nominal value. The color bar shows the χ^2 of the individual fits, and emissivity has been varied between 0.9 and 1. Low Γ corresponds to low emissivity and models with and without re-radiation have been considered. As a result, admissible thermal inertia values for the boulder in the MARA field of view were found to be 282^{+93}_{-35} J m^{-2} K^{-1} s$^{-1/2}$. This estimate is similar to telescopically determined thermal inertia values (Wada et al., 2018) of 150 to 300 J m^{-2} K^{-1} s$^{-1/2}$ and values determined by the thermal infrared imager on the Hayabusa2 spacecraft (Sugita et al., 2019), which range from 200 to 500 J m^{-2} K^{-1} s$^{-1/2}$. It therefore seems likely that boulders dominate the thermal emission from Ryugu, which would be consistent with the high rock abundance determined from orbiter images (ibid.). Therefore, contrary to expectation, the low thermal inertia derived for Ryugu does not correspond to a pebble-sized regolith-covered surface (Gundlach et al., 2013; Wada et al., 2018). Rather, boulder to block-sized clasts themselves appear to have thermal inertia lower than that of CM2 Cold Bokkeveld, which has the lowest thermal inertia (600 - 700 J m^{-2} K^{-1} s$^{-1/2}$) of a meteorite measured so far.

While thin layers of fine material could in principle mask the thermal signature of competent rock, the boulder observed by MARA appears to be free from an optically thick, dusty layer. Furthermore, the presence of a fine dust layer can be ruled out by considering a two layer thermal model. Results of the calculations (see methods) are shown in Figure 6.3, where dust with a thermal inertia of 25 J m^{-2} K^{-1} s$^{-1/2}$ was assumed to cover a boulder with a thermal inertia of 700 J m^{-2} K^{-1} s$^{-1/2}$. As is evident, the model is incompatible with the observed nighttime cooling rates, and the boulder observed by MARA itself must exhibit very low bulk thermal conductivity to fit the data. However, it cannot be ruled out that the low conductivity zone is limited to a highly porous outer layer. Such a layer may for example be generated by cracking due to thermal fatigue (Delbo et al., 2014; Hamm et al., 2019; Molaro et al., 2017) and could extend to a few thermal skin depths.

Given the above estimate of thermal inertia, thermal conductivity can be derived for a given bulk density and heat capacity (see methods). Furthermore, since thermal conductivity k of porous material depends more on porosity ϕ, and thus the total area of inter-grain contacts, than on the conductivity of the grains themselves (Sakatani et al., 2017), the porosity of the investigated boulder could in principle be estimated if the functional dependence of $k(\phi)$ were known. However, while models for H and

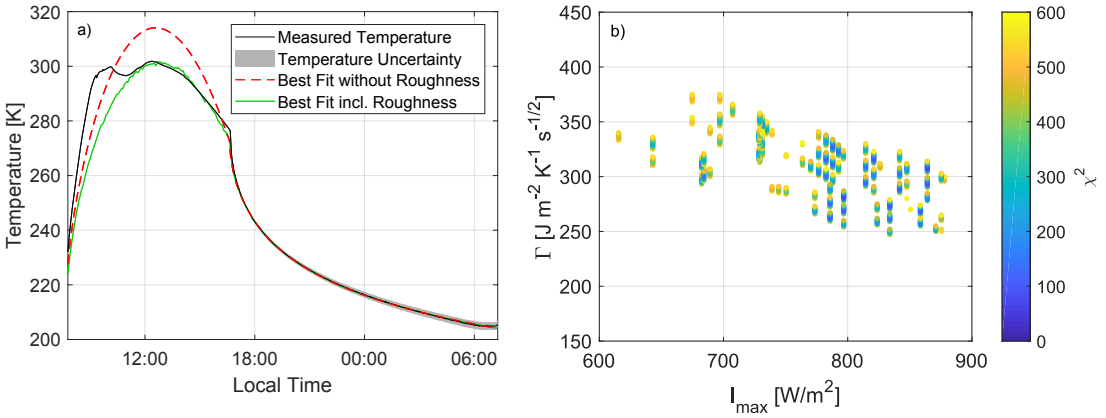

Figure 6.2: Observed and modeled surface temperatures and derived thermal inertia. a) Variation of surface temperature observed in-situ at geographical coordinates of 22.22 ± 0.05°S, 317.26 ± 0.07°E. Temperature is shown as a function of time as derived from the MARA 8-12 µm filter and using a surface emissivity of $\varepsilon = 1$. Error bars indicate 2σ confidence limits and uncertainties are below 0.5 K and 1.5 K during daytime and nighttime, respectively. Data are shown together with best fitting thermal models. While the model shown as a dashed red line assumes a flat surface, midday temperatures are reduced by surface roughness effects for the model shown in green. The steep rise of morning temperatures is caused by reflections from the MASCOT lander (not modeled). Best fitting models correspond to a thermal inertia of 282 $\mathrm{J\,m^{-2}\,K^{-1}\,s^{-1/2}}$ and a crater density of 0.34 (see methods). b) Retrieved thermal inertia as a function of the maximum insolation for the respective surface orientation. Emissivity has been varied between $\varepsilon = 0.9$ and 1. The χ^2 value of the individual fits is shown in color and admissible thermal inertia values were found to be 282^{+93}_{-35} $\mathrm{J\,m^{-2}\,K^{-1}\,s^{-1/2}}$.

L chondrites indicate that porosity and thus thermal conductivity is governed by dehydration- or shock-induced cracks (Flynn et al., 2018; Henke et al., 2016; Krause et al., 2011), thermal conductivity data on CI chondrites are absent. Nevertheless, since cracks are abundant in CI types (Tonui et al., 2014), it stands to reason that a similar mechanism would reduce thermal conductivity in these types and models derived for H and L chondrites should be applicable to CI types, too.

Two models (Flynn et al., 2018; Henke et al., 2016) for thermal conductivity as a function of porosity are shown in Figure 4a. Available data for H, L, and CM chondrites are shown together with the thermal conductivities extrapolated for Ryugu. The first model (Henke et al., 2016) results in $28 < \phi < 34\%$, typical for CM and CI chondrites, which have class average porosities of 22.2% and 34.9%, respectively (Flynn et al., 2018). The second model (ibid.) yields $41 < \phi < 55\%$. Other models applicable to partially-sintered granular material (Henke et al., 2016) yield intermediate results. Corresponding thermal conductivities are 0.06 - 0.13 and 0.09 – 0.16 $\mathrm{W\,m^{-1}\,K^{-1}}$, respectively, and thus much lower than measurements reported for the thermal conductivities of meteorites. Measurements on CI chondrites are missing entirely, but since CI chondrites are those

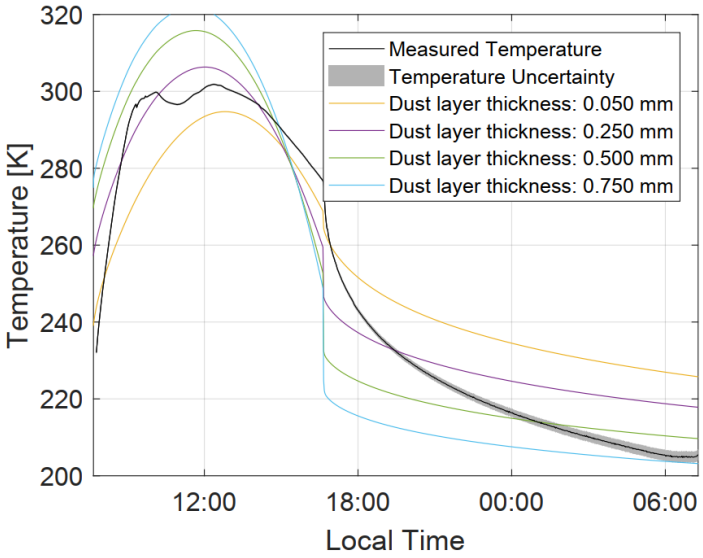

Figure 6.3: Modeled temperatures for a dust covered surface. Variation of surface temperature as a function of time as derived from the MARA 8-12 µm filter and using a surface emissivity of $\varepsilon = 1$. Error bars indicate 2σ confidence limits and uncertainties are below 0.5 K and 1.5 K during daytime and nighttime, respectively. Data are shown together with the results of a two layer thermal model, which assumes best fitting illumination conditions as well as a thin dust layer covering the underlying boulder. Dust thermal inertia is assumed to be 25 $\mathrm{J\,m^{-2}\,K^{-1}\,s^{-1/2}}$. Results for four different dust thicknesses assuming a boulder thermal inertia of 700 $\mathrm{J\,m^{-2}\,K^{-1}\,s^{-1/2}}$ are shown.

meteorites with highest porosities (Flynn et al., 2018), low conductivities could be expected.

Pores in the boulder would be observable in nighttime images, as the illumination provided by the MasCam LED array covers a variety of directions. However, no such pores are observed, indicating that potential pores must be smaller than 1 mm. The radiative contribution to the total heat transport inside the boulder can now be estimated by considering radiative heat exchange between parallel planes (Sakatani et al., 2017), and for pores smaller than 1 mm this results in a minor contribution to the overall thermal conductivity. The latter must therefore be governed by solid conduction through grain contacts. Given porosity and thermal conductivity, the amount of contacts can be estimated, which in turn can be converted to an estimate of tensile strength (see methods). Given the values derived above and assuming a Young's modulus representative for carbonaceous chondrites, tensile strength of the boulder is estimated to be 200 to 280 kPa and thus considerably lower than measurements on meteorite samples (Flynn et al., 2018), which generally show tensile strengths of the order of one to a few MPa (Ostrowski et al., 2019). This low tensile strength indicates an observational bias, namely that any hypothetical meteoroid originating from the boulder observed by

MASCOT would likely break up during atmospheric entry (Popova et al., 2011) and would thus be absent in our meteorite collections.

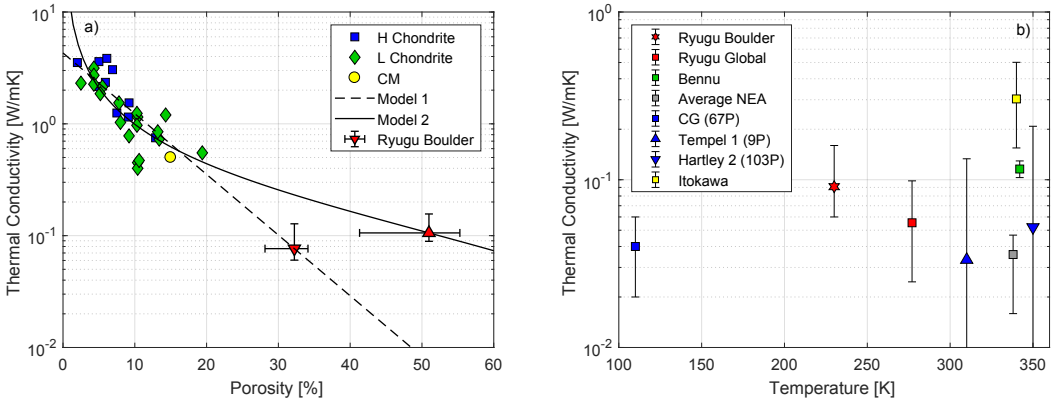

Figure 6.4: Derived thermal conductivity and boulder porosity. a) Thermal conductivity as a function of porosity. Data for H, L, and CM chondrites is shown together with two models fitting the data for porosities below 20%. For the low thermal conductivities determined from MARA measurements, models have to be extrapolated to high porosities. Depending on the model used, porosities between $28-34\%$ and $41-55\%$ are obtained. b) Thermal conductivity as a function of temperature as derived for different small bodies. For the boulder in the MARA field of view, a grain density of 2420 kg m^{-3} has been assumed. Heat capacity (Wada et al., 2018) was evaluated at 230 K, corresponding to the average observed nighttime temperature. In addition, conductivity values as derived from disc integrated measurements of Ryugu, disc integrated measurements of asteroid Bennu (DellaGiustina et al., 2019), as well as the estimated average thermal conductivity for near Earth asteroids (NEA) (Delbo et al., 2007) are shown. As a comparison, conductivity derived from in-situ observations of comet 67P/Churyumov–Gerasimenko (Spohn et al., 2015) as well as values derived from spacecraft observations of comets 9P/Tempel 1 (Davidsson et al., 2009; Groussin et al., 2013) and 103P/Hartley 2 (Groussin et al., 2013) are given. In contrast, the conductivity derived from disc integrated measurements of asteroid Itokawa (Müller et al., 2014) is also shown.

Thermal conductivity values derived above can be compared to estimates for other minor bodies, and corresponding data are shown in Figure 4b, where thermal conductivity is given as a function of temperature for asteroids (162173) Ryugu (Wada et al., 2018), (101955) Bennu (DellaGiustina et al., 2019), and the average estimated for small near Earth asteroids (Delbo et al., 2007). Values are compatible within error bars and similar to values derived for comets 67P/Churyumov–Gerasimenko (Spohn et al., 2015), 9P/Tempel 1 (Davidsson et al., 2009; Groussin et al., 2013), and 103P/Hartley 2 (Groussin et al., 2013) when heat capacity is properly scaled for temperature and appropriate densities are assumed (see methods section). On the other hand, estimates for S-type asteroid (25143) Itokawa (Fujiwara et al., 2006; Müller et al., 2014) are larger by a factor of three, indicating that thermal properties of C-type asteroids are more similar to those of comets than those of S-type asteroids. It is also worth noting that

no cubic dependence of thermal conductivity on temperature is observed in Figure 4b, which could indicate that radiative heat transfer through large pores is negligible in the bodies considered here.

The high porosities derived here have important implications for Ryugu's parent body. Assuming initial porosities (Yang et al., 2000) of the order of 70%, the Ryugu precursor needs to have been large enough to reduce intrinsic (micro-) porosity to values below 55% by compaction and aqueous alteration, while simultaneously avoiding porosities to drop below 28%. This implies that the material we observe on Ryugu's surface today was either produced in the outer layers of a larger (50-100 km sized) parent body, or the interior of a smaller, kilometer-sized body. The latter would be feasible provided accretion occurred while ^{26}Al was still active, in which case aqueous alteration and hot pressing of the precursor material would be efficient. In this way, porosities of 45% can be achieved starting from initial porosities of 70% even on small, kilometer-sized objects, provided that a water ice dominated primordial composition similar to that of CI/CM chondrites is assumed (Neumann et al., 2014, 2015).

6.3 METHODS

6.3.1 *Asteroid Thermophysical Model*

To estimate thermophysical properties from the brightness temperatures observed, a thermophysical model of the Ryugu boulder was constructed assuming a single, flat surface in the MARA field of view. A specific heat c_p of 600 J kg^{-1} K^{-1} and density ρ of 1270 kg m^{-3} have been assumed for the boulder, consistent with pre-encounter estimates (Wada et al., 2018). Parameters have been assumed to be constant and independent of temperature, as more complicated models did not improve the quality of the fit. Thermal conductivity k was treated as a free fitting parameter, and results are reported in terms of surface thermal inertia

$$\Gamma = \sqrt{k\rho c_p} \tag{6.1}$$

Insolation of the surface in the field of view was varied around the average surface normal which, according to the Ryugu shape model, points towards longitude 314.207°E and latitude 34.599°S in the asteroid fixed frame at the landing site. In a local frame, elevation and azimuth of the normal vector have been varied by 25° and 360° around this surface normal, respectively. This accounts for the unknown orientation of the surface in the MARA field of view and covers all plausible illumination conditions. Results are reported in terms of the maximum insolation corresponding to the respective surface normal. Furthermore, the times of sunrise and sunset have been adapted to fit MARA observations, which indicate that sunrise is delayed by 37 min with respect to the nominal insolation. In addition, the sun sets 21 min earlier than predicted by

the illumination model and insolation has been adapted accordingly. This is consistent with the terrain at the landing site, which shows that MASCOT is situated in a local depression.

Re-radiation from the environment onto the surface observed by MARA was taken into account using a local terrain model. View factors f from the surrounding topography to the surface have been estimated from the model and were found to amount to 0.048 ± 0.007 for facets within 1 meter of the MASCOT landing site (see supplementary Figures 6.5 and 6.6). No facet showed $f > 0.08$. In the thermophysical modeling, f has been varied between 0 and 0.08 to provide a conservative upper limit. The incident flux was then derived assuming that the surrounding terrain has temperatures T_{obs} corresponding to those on the surface of the boulder observed by MARA. As thermal re-radiation decreases the estimated thermal inertia, $f = 0.08$ results in an upper limit for the derived thermal inertia.

Given insolation I and thermal inertia Γ, the 1D heat equation is solved (Hamm et al., 2018) using

$$-\Gamma\sqrt{\frac{\pi}{P}}\frac{\partial T}{\partial z} = (1-A)I - \sigma\varepsilon T^4 + f\sigma\varepsilon T_{obs}^4 \tag{6.2}$$

as the upper boundary condition. Here, T is surface temperature, Γ thermal inertia, P rotation period, A bond albedo, σ the Stephan-Boltzmann constant, z depth normalized to the diurnal skin depth (Spencer et al., 1989), ε emissivity, and f the view factor to the surrounding environment. In the calculations, an albedo of $A = 0.0146$ is assumed while emissivity was varied between 0.9 and 1. The rotation period of Ryugu is 7.6326 h.

6.3.2 *Data Fitting*

To avoid complications caused by inhomogeneous temperatures in the MARA field of view due to the changing illumination conditions and re-radiation from the surroundings, only equilibrated nighttime data were used to fit thermophysical models (Christensen et al., 2004) and invert for thermophysical parameters. To fit the data, a suite of models was computed by systematically varying thermal inertia and the orientation of the surface normal in a grid search approach. In the models, thermal inertia was varied in steps of $1\,\mathrm{J\,m^{-2}\,K^{-1}\,s^{-1/2}}$ between 170 and 410 $\mathrm{J\,m^{-2}\,K^{-1}\,s^{-1/2}}$, elevation of the target surface normal was varied in steps of 5° between 90° and 65°, and azimuth of the target surface normal was varied in steps of 10° between 0° and 360°. For each model, the χ^2 value between model and data was computed and models resulting in a χ^2 larger than a critical value were discarded. Here we choose a critical χ^2_{crit} corresponding to a 2σ confidence interval (Hamm et al., 2018)

$$0.05 = \int_{\chi^2_{crit}}^{\infty} f(\chi^2, \nu)\, d\chi^2 \tag{6.3}$$

where $f(\chi^2, \nu)$ is the χ^2-distribution and ν is equal to the number of data points minus the number of fitting parameters. We obtain a critical χ^2_{crit} of 587.8 for the 534 data points obtained between 17:15 and 07:16 local time used in the fitting. The minimum χ^2_{min} obtained for the best fit was found to be $\chi^2_{min} = 66$.

This procedure was repeated by varying surface emissivity and assuming values of $\varepsilon = 0.9$, 0.95 and 1. Furthermore, models with view factors to the surroundings of $f = 0$ and 0.08 have been computed to study the effect of re-radiation, which was found to have only a small influence on nighttime temperatures. The stated uncertainty for the thermal inertia was then derived from the lowest and highest admissible values of all simulations. The best-fitting model has an emissivity of $\varepsilon = 1$. For consistency, the emissivity used for both the thermophysical models and the derivation of surface temperature from the observed flux was identical in all cases.

6.3.3 *Surface Roughness*

For a rough surface, observed flux depends on the solar zenith angle ϕ, the angle between surface normal and observation direction δ, as well as the angle between projections of the sun vector and the observation direction onto the surface ψ. These need to be taken into account when calculating fluxes received by the instrument. Here, the rough surface is modeled as a surface covered by spherical-section craters (Giese et al., 1990; Kührt et al., 1992), assuming lateral heat transport to be negligible. Using this model, a factor $c_r(\phi, \delta, \psi, t, \lambda)$ is calculated for each time t and observed wavelength λ relating the flux emitted by a flat surface F to the flux emitted by the rough surface $F_r = c_r(\phi, \delta, \psi, t, \lambda)F$. This model is scale-independent (Kührt et al., 1992), leaving the crater density on the surface and the opening angle of the craters as free parameters. The latter is kept constant at 180°, corresponding to a surface covered by hemispherical depressions. The model also depends on parameters such as albedo and heliocentric distance, which are all kept constant to be consistent with the thermophysical model described above. c_r was calculated at $\lambda = 10$ µm.

6.3.4 *Two-Layer Model*

To estimate the possible influence of a low conductivity dust layer on the modeling results, a two layer regolith model assuming geometry parameters corresponding to those of the best fitting one-layer model was calculated. In the model, the dust layer is treated in the continuum approximation, i.e., it is assumed that thermal transport properties inside the layer can be treated using the theory of porous media (Sakatani et al., 2017). This approximation breaks down if thin layers of dust are present, in which case radiative heat transport inside the dust layer would need to be treated explicitly. Here we assume that the dust layer has a thermal inertia of $25\,\mathrm{J\,m^{-2}\,K^{-1}\,s^{-1/2}}$. This

corresponds to typical particle sizes of $\sim$ 10 µm at porosities of 80% (ibid.). Therefore, our model assumptions are valid for layer thicknesses in excess of 50 µm.

Models have then been calculated varying the thermal inertia of the bottom layer along with the top layer thickness. Even thin dust layers appreciably distort the temperature curves, and using bottom layer thermal inertias between 250 and 700 $\mathrm{J\,m^{-2}\,K^{-1}\,s^{-1/2}}$, nighttime cooling curves could only be fitted within the errorbars for thermal inertias close to the values reported above. This indicates that the thermophysical properties of the boulder itself govern thermal emission.

6.3.5 *Thermal Conductivity and Porosity Estimate*

Thermal conductivity k and porosity ϕ for the boulder observed by MARA are calculated by solving

$$k = \frac{\Gamma^2}{c_p \rho_s (1-\phi)} \tag{6.4}$$

for a given functional dependence for $k(\phi)$. Here, Γ is thermal inertia, c_p is specific heat, ρ_s is grain density, and ϕ is porosity. For the grain density ρ_s, the average density of CI chondrites (Flynn et al., 2018; Macke et al., 2011) $\rho_s = 2420\,\mathrm{kg\,m^{-3}}$ has been assumed. Heat capacity was determined by evaluating (Wada et al., 2018) $c_p(T)$ at $T = 230$ K. For the functional dependence of $k(\phi)$, two models have been considered. Both are based on empirical fits to available thermal conductivity data for chondritic meteorites, and the first relation (Flynn et al., 2018) is

$$k(\phi) = \frac{0.11(1-\phi)}{\phi} \tag{6.5}$$

while the second relation (Henke et al., 2016) is

$$k(\phi) = 4.3 e^{-\phi/0.08} \tag{6.6}$$

Both formulations fit the experimental data equally well, but diverge at porosities larger than 20%.

To compare the thermal conductivity estimates for meteorites with those for comets, cometary thermal inertia estimates have been converted to an estimate of thermal conductivity assuming a cometary bulk density of 300 $\mathrm{kg\,m^{-3}}$ as derived from spacecraft observations (Groussin et al., 2013) of the Deep Impact experiment on 9P/Tempel 1. For the heat capacity, a value of 1000 $\mathrm{J\,kg^{-1}\,K^{-1}}$ was used (ibid.). For the computation of thermal conductivities for (101955) Bennu, (25143) Itokawa, and average NEA, heat

capacity (Wada et al., 2018) was evaluated at a temperature of 340 K, while for the disc-averaged measurement of (162173) Ryugu a temperature of 277 K has been assumed. Assumed bulk densities for (162173) Ryugu (ibid.), average NEA (Delbo et al., 2007), (25143) Itokawa (Fujiwara et al., 2006), and (101955) Bennu were 1270 kg m^{-3}, 1950 kg m^{-3}, 1950 kg m^{-3}, 1270 kg m^{-3}, respectively.

6.3.6 *Strength Estimate*

To estimate mechanical tensile strength given thermal conductivity k and porosity ϕ, the amount of inter-grain contacts is estimated neglecting radiative heat transport using (Sakatani et al., 2017)

$$k = \frac{4}{\pi^2} k_s (1-\phi) C H \tag{6.7}$$

where the grain thermal conductivity k_s has been assumed to be 2.95 W m^{-1} K^{-1} as appropriate for serpentine. Here, $H = r_c/R$ is the Hertz factor with r_c being the contact radius and R the radius of interacting spheres. For the coordination number C, the relation

$$C = \frac{2.812(1-\phi)^{-1/3}}{f_c^2(1+f_c^2)} \tag{6.8}$$

was used, where

$$f_c = 0.07318 + 2.193\phi - 3.357\phi^2 + 3.194\phi^3 \tag{6.9}$$

Given k, k_s, ϕ, C and H can then be calculated. For a random packing of identical, isotropic and homogeneous spheres with shear modulus μ and Poisson's ratio ν, the bulk elastic parameters can then be related to those in a porous medium following the approach of Digby (Digby, 1981): in Hertzian contact theory, two identical spheres have a circular contact area of radius r_c, depending on the confining pressure and the Young's modulus of the sphere material. In extension of the Hertz contact model, Digby assumes that the contact area between two spheres contains a small, concentric area of radius $r < r_c$ where the spheres are firmly bonded, i.e., remain in contact even without confining pressure. He obtains the effective Lamé parameters of the packing

$$\lambda_{Digby} = \frac{\mu C(1-\phi)}{5\pi R}\left[\frac{r_c}{1-\nu} - \frac{2r}{2-\nu}\right] \tag{6.10}$$

$$\mu_{Digby} = \frac{1}{2}\frac{\mu C(1-\phi)}{5\pi R}\left[\frac{2r_c}{1-\nu} - \frac{6r}{2-\nu}\right] \tag{6.11}$$

We take the adhesive region as a model for a sintering neck between two particles and consider the case without confining pressure, where $r \equiv r_c$. Using the relation

$$E = \mu \frac{3\lambda + 2\mu}{\lambda + \mu} \tag{6.12}$$

between Lamé-parameters and Young's modulus, and the relation

$$E = \mu(1 + \nu) \tag{6.13}$$

between shear modulus, Lamé parameter λ, Young's modulus E, we obtain the effective Young's modulus

$$E_{Digby} = \frac{1}{2\pi} \frac{r_c}{R} C(1 - \phi) \frac{1}{1 - \nu^2} \frac{5 - 4\nu}{5 - 3\nu} E \tag{6.14}$$

of the conglomerate of sintered spheres in relation to the Young's modulus of the matrix material. Since $0 \leq \nu \leq 1/2$ usually holds for Poisson's ratio, the dependence of E_{Digby} on ν amounts to a factor between 0.988 and $8/7$, or to $256/255 \approx 1.004$ if the matrix material is Poissonian. Therefore, we finally obtain

$$E_{Digby} \cong \frac{1}{2\pi} HC(1 - \phi)E = \frac{\pi}{8} \frac{k}{k_s} E \tag{6.15}$$

and the obtained (reduced) Young's modulus is then converted into an estimate of tensile strength σ_t using the empirical relation (Scholz, 2002)

$$\sigma_t = \frac{E_{Digby}}{500} = \frac{\pi}{4000} \frac{k}{k_s} E \tag{6.16}$$

7 The Young's modulus E of ordinary chondrites is usually reported (Flynn et al., 2018) to be of the order of tens of GPa, while values for carbonaceous chondrites are usually much lower (Ibrahim, 2012; Jones, 2009), ranging from a few to about 10 GPa. Here we assume 10 GPa to be representative for the Ryugu boulder, pointing out that this likely places an upper limit on the derived tensile strength.

6.4 ACKNOWLEDGMENTS

The MASCOT lander on the Hayabusa2 Mission of JAXA is a DLR/CNES cooperation. MASCOT MARA has been developed and built under the leadership of the DLR Institute of Planetary Research with contracted contributions from the Institute of Photonic Technology. The Hayabusa2 Mission is operated by JAXA. Funding: K.O. acknowledges funding by the JSPS Core-to-Core Program "International Network of Planetary Sciences." A.H. acknowledges funding by STFC under grant no. ST/S001271/1

6.5 SUPPORTING INFORMATION

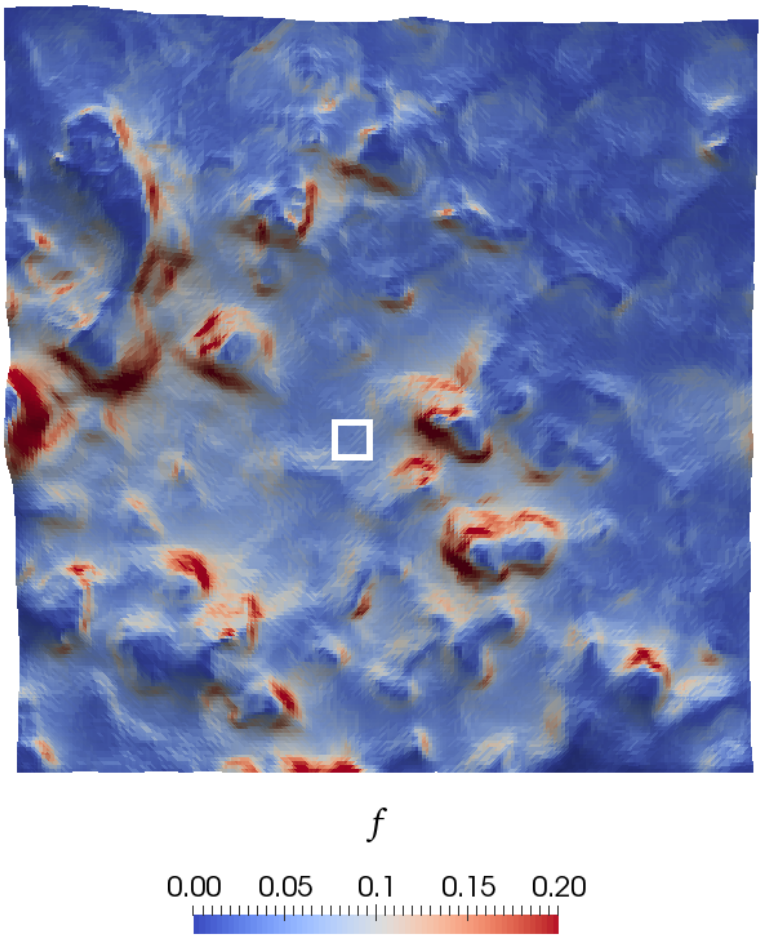

Figure 6.5: The integrated view factor f, i.e., the sum over all view factors of a given facet to all other visible facets in the model, as evaluated for a digital terrain model of the MASCOT landing site. The integrated view factor f is displayed in color. The colorbar saturates at 0.2. The MASCOT landing site is indicated by the white square.

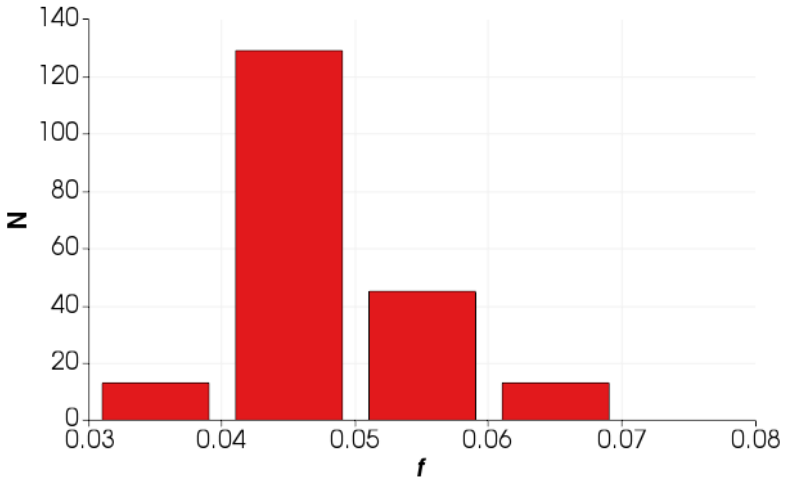

Figure 6.6: Histogram of viewfactors f for 400 selected facets centered at the MASCOT landing site. The average viewfactor is $f = 0.048 \pm 0.007$ (1σ).

7 CONCLUSIONS

7.1 SUMMARY

This chapter summarizes the main findings of the three presented studies and discusses their relevance in the broader scientific context. In chapter 4 the thermophysical model and data fitting method that were applied to the MARA data set were presented in a study that was published in Hamm et al. (2018). The fitting procedure was a χ^2 grid search and resulted in an intuitive visualization of the parameter space from which the uncertainty of the thermal inertia estimate and its correlation to other free parameters, e.g. emissivity and rock abundance, could be deduced. An interesting result was the possibility to retrieve an estimate of thermal inertia and emissivity simultaneously. The uncertainty of the retrieved emissivity is larger than 0.05 and thus similar to the depth of typical spectral features (Maturilli et al., 2016). However, the presented method includes the uncertainty of the emissivity in the uncertainty of the thermal inertia estimate, whereas most studies usually assume a single emissivity neglecting its influence on the thermal inertia determination. Furthermore, the presented simulations indicated that it should be possible to obtain information about the thermal-infrared spectral slope of the surface material using the narrow band filters of MARA. The presented net radiation heat transfer model allowed to interpret heterogeneous temperatures in the field of view. Such a situation arises when, e.g., the surface in the field of view is composed of a mixture of larger rocks and fines. Since the thermal inertia and with it the diurnal temperature evolution depends on the particle size of the regolith, a mix of temperatures would be observed by MARA. Additionally, small-scale topography and shadows can cause heterogeneous temperatures. While no fines were observed on Ryugu within the field of view of MARA, the presented model provides the flexibility to incorporate shadowing and small-scale topography in future analyses when a complex 3D shape model of the observed boulder becomes available.

The study in chapter 5 presented the latitudinal dependence of the diurnal temperature amplitude on a spherical asteroid by using the thermophysical model with variable obliquity and thermal inertia. It was published in Hamm et al. (2019). The diurnal temperature amplitude governs thermal stresses in boulders and thus drives thermal fatigue (Molaro et al., 2015, 2017). Therefore, the study provided insights into the location at which to expect thermal fatigue on an asteroid's surface. The main result of the study was that thermal fatigue is not limited to the equator. Instead, the latitude of maximum thermal forcing is determined by the balance between length of night and illumination power. Depending on the obliquity of the asteroid this latitude can

oscillate within a broad band around the equator during one orbit. Furthermore, the study pointed out that the maximum of the temperature amplitude is very flat and 90% of the maximum amplitude is still obtained in a large latitudinal band of $\pm 10^{\circ}$ to $\pm 30^{\circ}$ around this maximum. To relate the results of this study to Ryugu its topography has to be taken into account by relating the local slopes of the surface to latitudes on a sphere with the same solar declination. This will be discussed in the following section 7.2.

In chapter 6 the MARA in-situ observations on the surface of Ryugu and their analysis was presented, and results were published in Grott et al. (2019). These measurements were the first in-situ measurements in the thermal infrared covering a full diurnal cycle on an asteroid. The quality of the data was high with uncertainties below 1.5 K for the nighttime temperature observed in the two broad filters of MARA (Grott et al., 2017). MARA observed the temperature evolution of a single boulder and a low thermal inertia of 247-375 $\mathrm{J\,m^{-2}\,K^{-1}\,s^{-1/2}}$ was estimated (Grott et al., 2019). The study excluded the presence of a dust cover as the observed nighttime temperatures could in no case be reproduced by 2-layer models assuming a dust layer with variable thickness and low thermal inertia covering a rock layer with variable thermal inertia. Therefore, the low thermal inertia is likely a bulk property of the boulder. This was unexpected as the bulk thermal inertia of the surface regolith were assumed to be an order of magnitude higher (Wada et al., 2018). Yet, the results were consistent with the observation of the Hayabusa2 orbiter (Sugita et al., 2019) and disk-integrated observations from ground and space (Müller et al., 2017). The latter were interpreted as an indication for an asteroid surface covered by fine regolith consisting of 3 - 30 mm sized particles (Gundlach et al., 2013; Wada et al., 2018) and the presence of a large amount of meter-sized boulders was a surprise.

An explanation for the low thermal inertia given by the study was that the boulder consist of highly porous material. The study estimated the porosity to be between 28 and 55 % (Grott et al., 2019). The lower range of that estimate is consistent with the average porosity of CI (22.2 %) and CM (34.9 %) chondrites (Flynn et al., 2018). The upper range of the porosity estimate is more consistent with pristine fragments of the Tagish lake meteorite where a high porosity of up to 45 % was observed (Ralchenko et al., 2014). The regolith on Ryugu might be similar to these types of meteorites. The thermal inertia, thermal conductivity, and porosity estimates in this study were conservative and the thermal inertia and conductivity estimates are solid upper limits, while the porosity is a solid lower limit. The highest possible thermal inertia is retrieved for assuming an emissivity of $\varepsilon = 1$ and neglecting thermal radiation from the surrounding terrain. Consequently, any refinements in the analysis will result in lower retrieved thermal inertia, and consequently a higher porosity estimate.

7.2 IMPLICATIONS

The results presented in this work have important implications for the nature of Ryugu's surface material and the formation of Ryugu itself. How can the low observed thermal inertia and thermal conductivity be explained and how can the high porosity estimate be interpreted? A possibility is that thermal fatigue causes the low thermal conductivity of the surface material which was studied in chapter 5 (Hamm et al., 2019) and is discussed in the following.

Ryugu's obliquity is 171.64°, which means that it is spinning retrograde with an axis tilt of less than 9 degrees. Hamm et al. (ibid.) showed that on a sphere with the same axis tilt 90% of the thermal forcing occur within latitudes around ±30°. Ryugu's shape is similar to a spinning top. The mean slopes between 45° north and south on the conical hemispheres were estimated to be between 34 and 42° relative to the rotation axis (supplementary material of Watanabe et al. (2019)). In terms of illumination condition, these slopes are equivalent to latitudes on a spherical model, such that the results of chapter 5 for latitudes between 34 and 42° can be directly applied to the surface of Ryugu. The study indicates that most of Ryugu's surface is exposed to similar amounts of thermal forcing. If thermal fatigue is a relevant process on Ryugu, it should occur almost everywhere on its surface. The range of thermal inertia in that study was set to vary between 500 and 3000 $\mathrm{J\,m^{-2}\,K^{-1}\,s^{-1/2}}$ (Hamm et al., 2019) which covered the bulk values of rock and porous C-chondrites. However, the regolith on Ryugu has an even lower thermal inertia such that the diurnal temperature amplitudes were larger than anticipated in this study. The observed diurnal temperature range on Ryugu was 97 K. This is about half the temperature amplitude used in the experimental work by Delbo et al. (2014) which demonstrated that thermal fatigue will lead to small parts of regolith breaking off larger pieces. Models calculated by Molaro et al. (2017) support this work. They show that thermal stress will result in vertical and horizontal cracks in boulders, indicating that angular fragments could form due to thermal fatigue.

The presence of finer regolith fragments and macroscopic cracks would cause a low thermal inertia of the surface and some cracks and angular fragments were observed in the MasCam descent images (Jaumann et al., 2019). Contrarily, MasCam images of the boulder observed by MARA showed neither cracks nor loose particles and the presence of a dust layer could also be excluded by thermophysical models (Grott et al., 2019). Consequently, macroscopic cracks and fine regolith cannot explain the low observed thermal inertia. However, thermal fatigue might have caused microscopic cracks that could not be resolved by MASCAM. Yet, such microscopic cracks would not increase the porosity of the boulder significantly and are unlikely to explain the high porosity.

Alternatively, the observed porosity could be caused by loss of volatiles due to intensive, external heating. Such a situation could have occurred in the past if Ryugu's chaotic orbital evolution brought Ryugu close to the sun (Michel et al., 2010). This was discussed by Kitazato et al. (2019) as a possible cause for the flat NIRS3 spectra which

were similar to those of thermally processed C-chondrites. The possibility of short-term external heating was discussed by Sugita et al. (2019) and the principle component analysis presented in their study was consistent with intermediate dehydration of CM and CI chondrites. However, Sugita et al. (ibid.) point out that the observed small spread in the principle components indicates a homogenous dehydration of Ryugu's parent body through internal heating rather than external heating. As the parent body was then disrupted by an impact, Ryugu would have accreted from the debris originating from various depths of the parent body. In this case, observed homogeneous degree of dehydration would be a bulk property of Ryugu's material rather than a property of the visible layer.

In the light of the results by Hayabusa2 (Kitazato et al., 2019; Sugita et al., 2019; Watanabe et al., 2019) a high bulk porosity of the surface material could be a good explanation for the low thermal inertia estimated from the MARA measurements. While a high porosity limited to the outer layer of the regolith due to thermal fatigue or volatile loss through external heating cannot be excluded from MARA data alone, a high bulk porosity of 28 % to 55% (Grott et al., 2019) is consistent with the analysis of Sugita et al. (2019).

Such a high porosity is also consistent with the porosity of CM and CI meteorite samples (Flynn et al., 2018). CI1 chondrites might be different from Ryugu's surface material as they are devoid of inclusions, whereas MasCam observed abundant inclusions in the boulder on Ryugu which is consistent with CM chondrites or CI2 Tagish Lake rather than CI1 chondrites (Jaumann et al., 2019). However, the inclusions of CM chondrites are usually smaller than the ones observed on Ryugu (King et al., 1978). As stated above, the porosity of CI2 Tagish Lake samples is also consistent with the higher porosity estimates obtained from the MARA data (Ralchenko et al., 2014) such that a CI2 chondrites might be a good representation of Ryugu.

Assuming that the observed porosity is a property of the bulk material rather than being limited to a thermally processed outer layer, the porosity of the planetesimal parent body of Ryugu can be estimated. The porosity of the planetesimal reduces with time, e.g. through aqueous alteration and hot pressing, such that the initial porosity of the planetesimal needs to be even higher than the 28 % to 55% reported in this study (Neumann et al., 2014, 2015). As discussed in chapter 6, the initial porosity of Ryugu's parent body needed to be 70 % such that a compaction according to the model by Neumann et al. (2014) would lead to a porosity between 28 % and 55 % (Grott et al., 2019). This model also sets constraints to the size of the parent body, as larger objects experience stronger compaction. Ryugu would have formed either from material of the outer layer of a 50 - 100 km sized object or in the interior of a smaller one. The latter would require the presence of radioactive heat-generating ^{26}Al such that aqueous alteration and hot pressing could produce the observed porosity (Grott et al., 2019; Neumann et al., 2014). The latter scenario is consistent with the parent body proposed by Sugita et al. (2019) which assumes a water-ice dominated primordial

composition, which is also assumed for the aqueously altered CI and CM chondrites, and subsequent partial dehydration through internal heating due to the decay of radioactive ^{26}Al. The assumed high porosity of the parent body is consistent with the accretion model of a gentle gravitational collapse as described by e.g. Blum et al. (2017). In this model planetesimals form in streaming instabilities in the protosolar disk where pebbles concentrate in high pressure regions in the turbulent gas (e.g. Carrera et al., 2017; Drążkowska et al., 2017; Klahr et al., 2003; Youdin et al., 2005). In these models planetesimals grow rapidly and the streaming instability mechanism has the advantage of overcoming the issue of inward drift that would cause the planetesimal to spiral into the sun (Johansen et al., 2007).

In summary, the results of MARA are consistent with those of MasCam (Jaumann et al., 2019), NIRS3 (Kitazato et al., 2019), and ONC (Sugita et al., 2019). Ryugu is likely to be the remnant of a parent body that was aqueously altered and globally dehydrated through internal heating. The surface material is highly porous and upper estimates are consistent with CI2 chondrites while lower estimates are consistent with CM chondrites. These results will be tested by the compositional and structural analysis of the samples from Ryugu's surface that Hayabusa2 will return to Earth. While, the original, macroscopic structure of the samples will be destroyed by the sampling process, the microstructure of the samples should remain intact and might provide important context to the observations of Ryugu's surface material by Hayabusa2 and MASCOT.

The MASCOT mission was a great success and changed the view of C-type asteroids. Asteroid surfaces covered by large boulders can still exhibit a low thermal inertia, which is usually associated with granular surface material. Since several new missions to asteroids are currently in the planning phase, they should consider that the thermal inertia estimate for their respective target has to be interpreted with care. Planning of surface interactions needs to consider the possibility that there might be abundant large boulders covering the surface even if the thermal inertia points towards fine grains.

BIBLIOGRAPHY

Akai, J. (1992). "TTT diagram of serpentine and saponite, and estimation of metamorphic heating degree of Antarctic carbonaceous chondrites." In: *Antarctic Meteorite Research* 5, p. 120.

Aster, R., Borchers, B., and Thurber, C. (2013). *Parameter Estimation and Inverse Problems*. 2nd ed. Academic Press. Chap. 9.4, pp. 224–228.

Auger, A. T., Groussin, O., Jorda, L., El-Maarry, M. R., Bouley, S., et al. (2018). "Meter-scale thermal contraction crack polygons on the nucleus of comet 67P/Churyumov-Gerasimenko." In: *Icarus* 301, pp. 173–188. ISSN: 0019-1035. DOI: https://doi.org/10.1016/j.icarus.2017.09.037.

Bandfield, J., Ghent, R., Vasavada, A., Paige, D., Lawrence, S., et al. (2011). "Lunar surface rock abundance and regolith fines temperatures derived from LRO Diviner Radiometer data." In: *J. Geophys. Res.* 116, E00H02. DOI: 10.1029/2011JE003866.

Belton, M. J., Chapman, C. R., Klaasen, K. P., Harch, A. P., Thomas, P. C., et al. (1996). "Galileo's encounter with 243 Ida: An overview of the imaging experiment." In: *Icarus* 120.1, pp. 1–19.

Bibring, J.-P., Hamm, V., Langevin, Y., Pilorget, C., Arondel, A., et al. (2017). "The MicrOmega Investigation Onboard Hayabusa2." In: *Space Science Reviews* 208.1, pp. 401–412. DOI: 10.1007/s11214-017-0335-y.

Biele, J. and Ulamec, S. (2008). "Capabilities of Philae, the Rosetta Lander, in: Origin and Early Evolution of Comet Nuclei." In: *Space Sciences Series of ISSI* 28, pp. 275–289.

Binzel, R. P., Reddy, V., and Dunn, T. L. (2015). "The Near-Earth Object Population: Connections to Comets, Main-Belt Asteroids, and Meteorites." In: *Asteroids IV*. Ed. by P. Michel, F. E. DeMeo, and W. F. Bottke. Tucson, AZ, USA: Univ. of Arizona Press, pp. 243–257.

Binzel, R. P. and Sauter, L. M. (1992). "Trojan, Hilda, and Cybele asteroids: New lightcurve observations and analysis." In: *Icarus* 95.2, pp. 222–238.

Blum, J., Gundlach, B., Krause, M., Fulle, M., Johansen, A., et al. (2017). "Evidence for the formation of comet 67P/Churyumov-Gerasimenko through gravitational collapse of a bound clump of pebbles." In: *Monthly Notices of the Royal Astronomical Society* 469.Suppl_2, S755–S773.

Bottke, W., Vokrouhlický, D., Rubincam, D., and Nesvorný, D. (2006). "The Yarkovsky and YORP Effects: Implications for Asteroid Dynamics." In: *Ann. Rev. Earth Plan. Sci.* 34, pp. 157–191.

Bottke, W. F. (2008). "Asteroids: How to make a flying saucer." In: *Nature* 454.7201, p. 173.

Bowell, E., Hapke, B., Domingue, D., Lumme, K., Peltoniemi, J., et al. (1989). *Application of photometric models to asteroids*. Tucson, AZ, USA: Univeristy of Arizona Press, pp. 524–556.

Brearley, A. (2006). "The action of water." In: *Meteorites and the early solar system II*. Univ Arizona Press, Tucson.

Brown, P. G., Hildebrand, A. R., Zolensky, M. E., Grady, M., Clayton, R. N., et al. (2000). "The fall, recovery, orbit, and composition of the Tagish Lake meteorite: A new type of carbonaceous chondrite." In: *Science* 290.5490, pp. 320–325.

Bus, S. and Binzel, R. (2002). "Phase II of the Small Main-Belt Asteroid Spectroscopic Survey. A Feature-Based Taxonomy." In: *Icarus* 158 (1), pp. 146–177.

Čapek, D and Vokrouhlickỳ, D (2004). "The YORP effect with finite thermal conductivity." In: *Icarus* 172.2, pp. 526–536.

Capria, M. T., Tosi, F, De Sanctis, M., Capaccioni, F, Ammannito, E, et al. (2014). "Vesta surface thermal properties map." In: *Geophysical Research Letters* 41.5, pp. 1438–1443.

Carrera, D., Gorti, U., Johansen, A., and Davies, M. B. (2017). "Planetesimal formation by the streaming instability in a photoevaporating disk." In: *The Astrophysical Journal* 839.1, p. 16.

Chase Jr., S. (1969). "Infrared Radiometer for the 1969 Mariner Mission to Mars." In: *Applied Optics* 8 (3), pp. 639–642.

Chesley, S., Ostro, S., Vokrouhlický, D., Čapek, D., Giorgini, J., et al. (2003). "Direct Detection of the Yarkovsky Effect by Radar Ranging to Asteroid 6489 Golevka." In: *Science* 302 (5651), pp. 1739–1742.

Christensen, P. R., Bandfield, J. L., Hamilton, V. E., Howard, D. A., Lane, M. D., et al. (2000). "A thermal emission spectral library of rock-forming minerals." In: *Journal of Geophysical Research: Planets* 105.E4, pp. 9735–9739. DOI: doi:10.1029/1998JE000624.

Christensen, P. R., Hamilton, V. E., Mehall, G. L., Pelham, D., O'Donnell, W., et al. (2018). "The OSIRIS-REx Thermal Emission Spectrometer (OTES) Instrument." In: *Space Science Reviews* 214.5, p. 87. ISSN: 1572-9672. DOI: 10.1007/s11214-018-0513-6.

Christensen, P., Bandfield, J., Hamilton, V., Ruff, S., Kieffer, H., et al. (2001). "Mars Global Surveyor Thermal Emission Spectrometer experiment: Investigation description and surface science results." In: *J. Geophys. Res.* 106.E10, pp. 23823–23871. DOI: 10.1029/2000JE001370.

Christensen, P. R., Jakosky, B. M., Kieffer, H. H., Malin, M. C., McSween, H. Y., et al. (2004). "The thermal emission imaging system (THEMIS) for the Mars 2001 Odyssey Mission." In: *Space Science Reviews* 110.1-2, pp. 85–130.

Connelly, J. N., Bizzarro, M., Krot, A. N., Nordlund, k., Wielandt, D., et al. (2012). "The Absolute Chronology and Thermal Processing of Solids in the Solar Protoplanetary Disk." In: *Science* 338.6107, p. 651. DOI: 10.1126/science.1226919.

Coradini, A, Capaccioni, F, Erard, S, Arnold, G, De Sanctis, M., et al. (2011). "The surface composition and temperature of asteroid 21 Lutetia as observed by Rosetta/VIRTIS." In: *Science* 334.6055, pp. 492–494.

Cross, P. C., Decius, J., and Wilson, E. B. (1955). *Molecular Vibrations: The Theory of Infrared and Raman Vibrational Spectra. Cross*. McGraw-Hill.

Dahlgren, M and Lagerkvist, C.-I. (1995). "A study of Hilda asteroids. I. CCD spectroscopy of Hilda asteroids." In: *Astronomy and Astrophysics* 302, p. 907.

Dahlgren, M., Lagerkvist, C.-I., Fitzsimmons, A, Williams, I., and Gordon, M (1997). "A study of Hilda asteroids. II. Compositional implications from optical spectroscopy." In: *Astronomy and Astrophysics* 323, pp. 606–619.

Davidsson, B. J. R. and Rickman, H. (2014). "Surface roughness and three-dimensional heat conduction in thermophysical models." In: *Icarus* 243, pp. 58–77. ISSN: 00191035. DOI: 10.1016/j.icarus.2014.08.039.

Davidsson, B. J., Gutiérrez, P. J., and Rickman, H. (2009). "Physical properties of morphological units on Comet 9P/Tempel 1 derived from near-IR Deep Impact spectra." In: *Icarus* 201.1, pp. 335–357.

Davidsson, B. J., Rickman, H., Bandfield, J. L., Groussin, O., Gutiérrez, P. J., et al. (2015). "Interpretation of thermal emission. I. The effect of roughness for spatially resolved atmosphereless bodies." In: *Icarus* 252, pp. 1–21.

Davis, D., Chapman, C., Greenberg, R, and Weidenschilling, S. (1982). "Hirayama families: Chips off the old block or collections of rubble piles?" In: *Bulletin of the American Astronomical Society*. Vol. 14, p. 720.

DeMeo, F. E., Alexander, C. M., Walsh, K. J., Chapman, C. R., and Binzel, R. P. (2015). "The Compositional Structure of the Asteroid Belt." In: *Asteroids IV*. Ed. by P. Michel, F. E. DeMeo, and W. F. Bottke. Tucson, AZ, USA: Univ. of Arizona Press, pp. 13–41.

DeMeo, F. and Carry, B. (2014). "Solar System evolution from compositional mapping of the asteroid belt." In: *Nature* 505.7485, p. 629.

DeMeo, F. E., Binzel, R. P., Slivan, S. M., and Bus, S. J. (2009). "An extension of the Bus asteroid taxonomy into the near-infrared." In: *Icarus* 202.1, pp. 160–180. DOI: 10.1016/j.icarus.2009.02.005.

Delbo, M., Libourel, G., Wilkerson, J., Murdoch, N., Michel, P., et al. (2014). "Thermal fatigue as the origin of regolith on small asteroids." In: *Nature* 508, pp. 233–236. DOI: 10.1038/nature13153.

Delbo, M., Dell'Oro, A., Harris, A. W., Mottola, S., Mueller, M., et al. (2007). "Thermal inertia of near-Earth asteroids and implications for the magnitude of the Yarkovsky effect." In: *Icarus* 190.1, pp. 236–249.

DellaGiustina, D., Emery, J., Golish, D., Rozitis, B., Bennett, C., et al. (2019). "Properties of rubble-pile asteroid (101955) Bennu from OSIRIS-REx imaging and thermal analysis." In: *Nature Astronomy* 3.4, p. 341.

Dermott, S. F. and Murray, C. D. (1983). "Nature of the Kirkwood gaps in the asteroid belt." In: *Nature* 301.5897, pp. 201–205. DOI: 10.1038/301201a0.

Dew, P. M. and Walsh, J. E. (1981). "A Set of Library Routines for Solving Parabolic Equations in One Space Variable." In: *ACM Transactions on Mathematical Software* 7.3, pp. 295–314.

Di Sisto, R. P., Brunini, A., Dirani, L. D., and Orellana, R. B. (2005). "Hilda asteroids among Jupiter family comets." In: *Icarus* 174.1, pp. 81–89.

Digby, P. (1981). "The effective elastic moduli of porous granular rocks." In: *Journal of Applied Mechanics* 48.4, pp. 803–808.

Dombard, A. J., Barnouin, O. S., Prockter, L. M., and Thomas, P. C. (2010). "Boulders and ponds on the Asteroid 433 Eros." In: *Icarus* 210.2, pp. 713–721. DOI: 10.1016/j.icarus.2010.07.006.

Drążkowska, J and Alibert, Y. (2017). "Planetesimal formation starts at the snow line." In: *Astronomy & Astrophysics* 608, A92.

Duxbury, T. C., Newburn, R. L., Acton, C. H., Carranza, E., McElrath, T. P., et al. (2004). "Asteroid 5535 Annefrank size, shape, and orientation: Stardust first results." In: *Journal of Geophysical Research: Planets* 109.E2.

Emery, J. P., Cruikshank, D. P., and Van Cleve, J. (2006). "Thermal emission spectroscopy (5.2–38 μm) of three Trojan asteroids with the Spitzer Space Telescope: Detection of fine-grained silicates." In: *Icarus* 182.2, pp. 496–512. DOI: https://doi.org/10.1016/j.icarus.2006.01.011.

Emery, J. P., Marzari, F., Morbidelli, A., French, L. M., and Grav, T. (2015). "The Complex History of Trojan Asteroids." In: *Asteroids IV*. Ed. by P. Michel, F. E. DeMeo, and W. F. Bottke. Tucson, AZ, USA: Univ. of Arizona Press, pp. 203–221.

Emery, J., Fernández, Y., Kelley, M., Warden, K., Hergenrother, C, et al. (2014). "Thermal infrared observations and thermophysical characterization of OSIRIS-REx target asteroid (101955) Bennu." In: *Icarus* 234, pp. 17–35.

Endreß, M. and Bischoff, A. (1996). "Carbonates in CI chondrites: Clues to parent body evolution." In: *Geochimica et Cosmochimica Acta* 60.3, pp. 489–507.

Eppes, M.-C., Willis, A., Molaro, J., Abernathy, S., and Zhou, B. (2015). "Cracks in Martian boulders exhibit preferred orientations that point to solar-induced thermal stress." In: *Nature Communications* 6, p. 6712. DOI: 10.1038/ncomms7712.

Farnocchia, D., Chesley, S., Vokrouhlickỳ, D, Milani, A, Spoto, F, et al. (2013). "Near Earth asteroids with measurable Yarkovsky effect." In: *Icarus* 224.1, pp. 1–13.

Fergason, R. L., Christensen, P. R., and Kieffer, H. H. (2006a). "High-resolution thermal inertia derived from the Thermal Emission Imaging System (THEMIS): Thermal model and applications." In: *Journal of Geophysical Research* 111.E12004. DOI: 10.1029/2006je002735.

Fergason, R. L., Christensen, P. R., Bell III, J. F., Golombeck, M. P., Herkenhoff, K. E., et al. (2006b). "Physical properties of the Mars Exploration Rover landing sites as inferred from Mini-TES-derived thermal inertia." In: *Journal of Geophysical Research* 111.E02S21. DOI: 10.1029/2005JE002583.

Flynn, G. J., Consolmagno, G. J., Brown, P., and Macke, R. J. (2018). "Physical properties of the stone meteorites: Implications for the properties of their parent bodies." In: *Geochemistry* 78.3, pp. 269 –298. ISSN: 0009-2819. DOI: https://doi.org/10.1016/j.chemer.2017.04.002.

Formisano, M, De Sanctis, M., Magni, G, Federico, C, and Capria, M. (2015). "Ceres water regime: Surface temperature, water sublimation and transient exo (atmo) sphere." In: *Monthly Notices of the Royal Astronomical Society* 455.2, pp. 1892–1904.

Fujiwara, A., Kawaguchi, J, Yeomans, D., Abe, M, Mukai, T, et al. (2006). "The rubble-pile asteroid Itokawa as observed by Hayabusa." In: *Science* 312.5778, pp. 1330–1334.

Garcia, R. F., Murdoch, N., and Mimoun, D. (2015). "Micro-meteoroid seismic uplift and regolith concentration on kilometric scale asteroids." In: *Icarus* 253, pp. 159 –168. DOI: https://doi.org/10.1016/j.icarus.2015.02.014.

Gear, C. W. (1971). *Numerical initial value problems in ordinary differential equations*. Prentice Hall PTR.

Giese, B. and Kührt, E. (1990). "Theoretical interpretation of infrared measurements at Deimos in the framework of crater radiation." In: *Icarus* 44, pp. 142–153.

Gómez-Elvira, J., Armiens, C., Castañer, L., Domínguez, M., Genzer, M., et al. (2012). "REMS: The Environmental Sensor Suite for the Mars Science Laboratory Rover." In: *Space Science Review* 170 (1-4), pp. 583–640. DOI: 10.1007/s11214-012-9921-1.

Grott, M., Knollenberg, J., Borgs, B., Hänschke, F., Kessler, E., et al. (2017). "The MASCOT Radiometer MARA for the Hayabusa 2 Mission." In: *Space Science Reviews* 208.1-4, pp. 413–431. DOI: 10.1007/s11214-016-0272-1.

Grott, M., Knollenberg, J., Hamm, M., Ogawa, K., Jaumann, R., et al. (2019). "Low thermal conductivity boulder with high porosity identified on C-type asteroid (162173) Ryugu." In: *Nature Astronomy*. ISSN: 2397-3366. DOI: 10.1038/s41550-019-0832-x.

Groussin, O, Sunshine, J., Feaga, L., Jorda, L, Thomas, P., et al. (2013). "The temperature, thermal inertia, roughness and color of the nuclei of Comets 103P/Hartley 2 and 9P/Tempel 1." In: *Icarus* 222.2, pp. 580–594.

Gulkis, S., Allen, M., Allmen, P. von, Beaudin, G., Biver, N., et al. (2015). "Subsurface properties and early activity of comet 67P/Churyumov-Gerasimenko." In: *Science* 347.6220, aaa0709.

Gundlach, B. and Blum, J. (2013). "A new method to determine the grain size of planetary regolith." In: *Icarus* 223.1, pp. 479–492. DOI: 10.1016/j.icarus.2012.11.039.

Hamilton, V. E., Vasavada, A. R., Sebastian, E., Torre Juárez, M. de la, Ramos, M., et al. (2014). "Observations and preliminary science results from the first 100 sols of MSL Rover Environmental Monitoring Station ground temperature sensor measurements at Gale Crater." In: *Journal of Geophysical Research: Planets* 119.4, pp. 745–770. DOI: 10.1002/2013je004520.

Hamm, M., Grott, M., Kührt, E., Pelivan, I., and Knollenberg, J. (2018). "A method to derive surface thermophysical properties of asteroid (162173) Ryugu (1999JU3) from in-situ surface brightness temperature measurements." In: *Planetary and Space Science* 159, pp. 1–10. ISSN: 0032-0633. DOI: https://doi.org/10.1016/j.pss.2018.03.017.

Hamm, M., Senshu, H., and Grott, M. (2019). "Latitudinal dependence of asteroid regolith formation by thermal fatigue." In: *Icarus* 319, pp. 308–311.

Harris, A. W. (1998). "A Thermal Model for Near-Earth Asteroids." In: *Icarus* 131, pp. 291–301.

Harris, A. W. and Drube, L. (2016). "Thermal tomography of asteroid surface structure." In: *The Astrophysical Journal* 827.2, p. 127.

Harris, A., Barucci, M., Cano, J., Fitzsimmons, A, Fulchignoni, M, et al. (2013). "The European Union funded NEOShield project: A global approach to near-Earth object impact threat mitigation." In: *Acta Astronautica* 90.1, pp. 80–84.

Harris, A. W., Delbó, M., Binzel, R. P., Davies, J. K., Roberts, J., et al. (2001). "Visible to thermal-infrared spectrophotometry of a possible inactive cometary nucleus." In: *Icarus* 153.2, pp. 332–337.

Harris, A. W. and Lagerros, J. S. (2002). "Asteroids in the thermal infrared." In: *Asteroids III* 205.

Hartmann, W. K., Tholen, D. J., and Cruikshank, D. P. (1987). "The relationship of active comets,"extinct" comets, and dark asteroids." In: *Icarus* 69.1, pp. 33–50.

Hayne, P. O., Bandfield, J. L., Siegler, M. A., Vasavada, A. R., Ghent, R. R., et al. (2017). "Global regolith thermophysical properties of the Moon from the Diviner Lunar Radiometer Experiment." In: *Journal of Geophysical Research: Planets* 122.12, pp. 2371–2400.

Hemingway, B., Robie, R., and Wilson, W. (1973). "Specific heats of lunar soils, basalt, and breccias from the Apollo 14, 15, and 16 landing sites, between 90 and 350 K." In: *Lunar and Planetary Science Conference Proceedings*. Vol. 4, p. 2481.

Henke, S., Gail, H.-P., and Trieloff, M. (2016). "Thermal evolution and sintering of chondritic planetesimals-III. Modelling the heat conductivity of porous chondrite material." In: *Astronomy & Astrophysics* 589, A41.

Hercik, D., Auster, H.-U., Blum, J., Fornacon, K.-., Fujimoto, M., et al. (2017). "The MASCOT Magnetometer." In: *Space Science Reviews* 208.1, pp. 433–449. DOI: 10.1007/s11214-016-0236-5.

Hiesinger, J. and Helbert, J. M. C.-I. T. (2010). "The Mercury radiometer and thermal infrared spectrometer (MERTIS) for the BepiColombo mission." In: *Planet. Space Sci.* 58.1-2, pp. 144–165.

Ho, T.-M., Baturkin, V., Grimm, C., Grundmann, J. T., Hobbie, C., et al. (2017). "MASCOT—The Mobile Asteroid Surface Scout Onboard the Hayabusa2 Mission." In: *Space Sci. Rev.* 208.1-4, pp. 339–374. DOI: 10.1007/s11214-016-0251-6.

Howell, J. R., Siegler, R., and & Mengüc, M. P. (2016). *Thermal Radiation Heat Transfer*. 6th ed. CRC Press. Chap. 5, pp. 205–231.

Hunt, G. R. and Salisbury, J. W. (1974). *Mid-Infrared Spectral Behavior of Igneous Rocks.* Tech. rep. No. AFCRL-TR-74-0625. AIR FORCE CAMBRIDGE RESEARCH LABS HANSCOM AFB MASS.

Ibrahim, M. I. (2012). "The Elastic Properties of Carbonaceous Chondrites M. Sc. Thesis." In: *Department of Geoscience, University of Calgary*.

Ishiguro, M., Kuroda, D., Hasegawa, S., Kim, M.-J., Choi, Y.-J., et al. (2014). "Optical Properties of (162173) 1999 Ju3: In Preparation for the Jaxa Hayabusa2 sample Return Mission." In: *The Astrophysical Journal* 792.1. DOI: 10.1088/0004-637x/792/1/74.

Ivezić, Ž., Tabachnik, S., Rafikov, R., Lupton, R. H., Quinn, T., et al. (2001). "Solar System Objects Observed in the Sloan Digital Sky Survey Commissioning Data." In: *The Astronomical Journal* 122.5, pp. 2749–2784. DOI: 10.1086/323452.

Iwata, T., Kitazato, K., Abe, M., Ohtake, M., Arai, T., et al. (2017). "NIRS3: The Near Infrared Spectrometer on Hayabusa2." In: *Space Science Reviews* 208.1, pp. 317–337. DOI: 10.1007/s11214-017-0341-0.

Jarosewich, E. (1990). "Chemical analyses of meteorites: A compilation of stony and iron meteorite analyses." In: *Meteoritics* 25.4, pp. 323–337.

Jaumann, R., Williams, D. A., Buczkowski, D. L., Yingst, R. A., Preusker, F., et al. (2012). "Vesta's shape and morphology." In: *Science* 336.6082, pp. 687–690. DOI: 10.1126/science.1219122.

Jaumann, R., Schmitz, N., Koncz, A., Michaelis, H., Schroeder, S. E., et al. (2017). "The Camera of the MASCOT Asteroid Lander on Board Hayabusa 2." In: *Space Sci. Rev.* 208.1, pp. 375–400.

Jaumann, R., Schmitz, N., Ho, T.-M., Schröder, S., Otto, K., et al. (2019). "Images from the surface of asteroid Ryugu show rocks similar to carbonaceous chondrite meteorites." In: *Science* accepted, aaw8627.

Jewitt, D. (2012). "The active asteroids." In: *The Astronomical Journal* 143.3, p. 66.

Johansen, A., Oishi, J. S., Mac Low, M.-M., Klahr, H., Henning, T., et al. (2007). "Rapid planetesimal formation in turbulent circumstellar disks." In: *Nature* 448.7157, p. 1022.

Jones, S. F. (2009). "Elastic Wave Velocity, Porosity, and Pore Geometry of Ordinary Chondrites and Artificially Shocked Samples. M. Sc. Thesis." In: *Department of Geoscience, University of Calgary*.

Kallemeyn, G. W. and Wasson, J. T. (1981). "The compositional classification of chondrites—I. The carbonaceous chondrite groups." In: *Geochimica et Cosmochimica Acta* 45.7, pp. 1217–1230.

Kallemeyn, G. W., Rubin, A. E., Wang, D., and Wasson, J. T. (1989). "Ordinary chondrites: Bulk compositions, classification, lithophile-element fractionations and composition-petrographic type relationships." In: *Geochimica et Cosmochimica Acta* 53.10, pp. 2747–2767.

Kallemeyn, G. W., Rubin, A. E., and Wasson, J. T. (1991). "The compositional classification of chondrites: V. The Karoonda (CK) group of carbonaceous chondrites." In: *Geochimica et Cosmochimica Acta* 55.3, pp. 881–892.

Kallemeyn, G. W., Rubin, A. E., and Wasson, J. T. (1994). "The compositional classification of chondrites: VI. The CR carbonaceous chondrite group." In: *Geochimica et Cosmochimica Acta* 58.13, pp. 2873–2888.

Kallemeyn, G. W., Rubin, A. E., and Wasson, J. T. (1996). "The compositional classification of chondrites: VII. The R chondrite group." In: *Geochimica et Cosmochimica Acta* 60.12, pp. 2243–2256.

Kameda, S., Suzuki, H., Takamatsu, T., Cho, Y., Yasuda, T., et al. (2017). "Preflight Calibration Test Results for Optical Navigation Camera Telescope (ONC-T) Onboard the Hayabusa2 Spacecraft." In: *Space Science Reviews* 208.1, pp. 17–31. DOI: 10.1007/s11214-015-0227-y.

Kataoka, Akimasa, Tanaka, Hidekazu, Okuzumi, Satoshi, and Wada, Koji (2013). "Fluffy dust forms icy planetesimals by static compression." In: *A&A* 557, p. L4. DOI: 10.1051/0004-6361/201322151.

Kawaguchi J.and Uesugi, K. and Fujiwara, A. (2003). "The MUSES-C mission for the sample and return—its technology development status and readiness." In: *Acta Astronautica* 52.2, pp. 117 –123. DOI: https://doi.org/10.1016/S0094-5765(02)00146-7.

Keihm, S, Tosi, F, Kamp, L, Capaccioni, F, Gulkis, S, et al. (2012). "Interpretation of combined infrared, submillimeter, and millimeter thermal flux data obtained during the Rosetta fly-by of Asteroid (21) Lutetia." In: *Icarus* 221.1, pp. 395–404.

Keihm, S., Tosi, F., Capria, M. T., De Sanctis, M. C., Longobardo, A., et al. (2015). "Separation of thermal inertia and roughness effects from Dawn/VIR measurements of Vesta surface temperatures in the vicinity of Marcia Crater." In: *Icarus* 262, pp. 30–43. DOI: 10.1016/j.icarus.2015.08.028.

Keller, H., Barbieri, C., Koschny, D., Lamy, P., Rickman, H., et al. (2010). "E-type asteroid (2867) Steins as imaged by OSIRIS on board Rosetta." In: *Science* 327.5962, pp. 190–193.

Kieffer, H. H. (2013). "Thermal model for analysis of Mars infrared mapping." In: *Journal of Geophysical Research: Planets* 118.3, pp. 451–470. DOI: 10.1029/2012je004164.

Kieffer, H. H., Neugebauer, G., Munch, G., Chase, S., and Miner, E. (1972). "Infrared thermal mapping experiment: The Viking Mars orbiter." In: *Icarus* 16.1, pp. 47 –56. DOI: https://doi.org/10.1016/0019-1035(72)90136-4.

King, T. V. and King, E. A. (1978). "Grain size and petrography of C2 and C3 carbonaceous chondrites." In: *Meteoritics* 13.1, pp. 47–72.

Kirkwood, D. (1867). *Meteoritic Astronomy*. Philadelphia: Lippincott.

Kita, N. T., Yin, Q.-Z., MacPherson, G. J., Ushikubo, T., Jacobsen, B., et al. (2013). "26Al-26Mg isotope systematics of the first solids in the early solar system." In: *Meteoritics & Planetary Science* 48.8, pp. 1383–1400. DOI: 10.1111/maps.12141.

Kitazato, K, Milliken, R., Iwata, T, Abe, M, Ohtake, M, et al. (2019). "The surface composition of asteroid 162173 Ryugu from Hayabusa2 near-infrared spectroscopy." In: *Science*, eaav7432.

Klahr, H and Bodenheimer, P (2003). "The Formation of a Planet in the Eye of a Hurricane–A Three Phase Model for Planet Formation." In: *Bulletin of the American Astronomical Society*. Vol. 35, p. 961.

Kleine, T., Touboul, M., Orman, J. A. V., Bourdon, B., Maden, C., et al. (2008). "Hf–W thermochronometry: Closure temperature and constraints on the accretion and cooling history of the H chondrite parent body." In: *Earth and Planetary Science Letters* 270.1, pp. 106 –118. ISSN: 0012-821X. DOI: https://doi.org/10.1016/j.epsl.2008.03.013.

Koga, S. C., Sugita, S., Kamata, S., Ishiguro, M., Hiroi, T., et al. (2018). "Spectral decomposition of asteroid Itokawa based on principal component analysis." In: *Icarus* 299, pp. 386–395.

Koschny, D., Soja, R. H., Engrand, C., Flynn, G. J., Lasue, J., et al. (2019). "Interplanetary Dust, Meteoroids, Meteors and Meteorites." In: *Space Science Reviews* 215.4, p. 34.

Krause, M., Blum, J., Skorov, Y. V., and Trieloff, M. (2011). "Thermal conductivity measurements of porous dust aggregates: I. Technique, model and first results." In: *Icarus* 214.1, pp. 286–296.

Krot, A. N., Keil, K., Scott, E. R. D., Goodrich, C. A., and Weisberg, M. K. (2014). "Classification of Meteorites and Their Genetic Relationships." In: *Meteorites and Cosmochemical Processes*. Ed. by A. M. Davis, pp. 1–63.

Kührt, E. (1984). "Temperature profiles and thermal stresses in cometary nuclei." In: *Icarus* 60.3, pp. 512–521. ISSN: 0019-1035. DOI: https://doi.org/10.1016/0019-1035(84)90158-1.

Kührt, E., Giese, B., Keller, H. U., and Ksanfomality, L. (1992). "Interpretation of the KRFM-infrared measurements of phobos." In: *Icarus* 96.2, pp. 213–218. DOI: 10.1016/0019-1035(92)90075-i.

Lagerros, J. (1996). "Thermal physics of asteroids. I. Effects of shape, heat conduction and beaming." In: *Astronomy and Astrophysics* 310, pp. 1011–1020.

Landsman, Z. A., Licandro, J., Campins, H., Ziffer, J., Prá, M. d., et al. (2016). "The Veritas and Themis asteroid families: 5–14 μm spectra with the Spitzer Space Telescope." In: *Icarus* 269, pp. 62–74. DOI: 10.1016/j.icarus.2016.01.008.

Lauretta, D. S., Bartels, A. E., Barucci, M. A., Bierhaus, E. B., Binzel, R. P., et al. (2015). "The OSIRIS-REx target asteroid (101955) Bennu: Constraints on its physical, geological, and dynamical nature from astronomical observations." In: *Meteoritics & Planetary Science* 50.4, pp. 834–849. ISSN: 10869379. DOI: 10.1111/maps.12353.

Lauretta, D., DellaGiustina, D., Bennett, C., Golish, D., Becker, K., et al. (2019). "The unexpected surface of asteroid (101955) Bennu." In: *Nature*, p. 1.

Leyrat, C, Coradini, A, Erard, S, Capaccioni, F, Capria, M., et al. (2011). "Thermal properties of the asteroid (2867) Steins as observed by VIRTIS/Rosetta." In: *Astronomy & Astrophysics* 531, A168.

Lowry, S. C., Fitzsimmons, A., Pravec, P., Vokrouhlickỳ, D., Boehnhardt, H., et al. (2007). "Direct detection of the asteroidal YORP effect." In: *science* 316.5822, pp. 272–274.

Luque, A., Ruiz-Agudo, E., Cultrone, G., Sebastián, E., and Siegesmund, S. (2011). "Direct observation of microcrack development in marble caused by thermal weather-

ing." In: *Environmental Earth Sciences* 62.7, pp. 1375–1386. DOI: 10.1007/s12665-010-0624-1.

Lyon, R. (1965). "Analysis of rocks by spectral infrared emission (8 to 25 microns)." In: *Economic Geology* 60.4, pp. 715–736.

Macke, R. (2010). "Survey of meteorite physical properties: density, porosity and magnetic susceptibility [PhD thesis]." In: *Orlando, FL: University of Central Florida*.

Macke, R. J., Consolmagno, G. J., and Britt, D. T. (2011). "Density, porosity, and magnetic susceptibility of carbonaceous chondrites." In: *Meteoritics & Planetary Science* 46.12, pp. 1842–1862.

Magri, C., Howell, E. S., Vervack Jr, R. J., Nolan, M. C., Fernández, Y. R., et al. (2018). "SHERMAN, a shape-based thermophysical model. I. Model description and validation." In: *Icarus* 303, pp. 203–219.

Mainzer, A., Bauer, J., Grav, T., Masiero, J., Cutri, R. M., et al. (2011). "PRELIMINARY RESULTS FROM NEOWISE: AN ENHANCEMENT TO THEWIDE-FIELD INFRARED SURVEY EXPLORER FOR SOLAR SYSTEM SCIENCE." In: *The Astrophysical Journal* 731.1, p. 53. DOI: 10.1088/0004-637x/731/1/53.

Marshall, S. E., Howell, E. S., Magri, C., Vervack Jr, R. J., Campbell, D. B., et al. (2017). "Thermal properties and an improved shape model for near-Earth asteroid (162421) 2000 ET70." In: *Icarus* 292, pp. 22–35.

Masiero, J. R., Mainzer, A., Grav, T, Bauer, J., Cutri, R., et al. (2011). "Main belt asteroids with WISE/NEOWISE. I. Preliminary albedos and diameters." In: *The Astrophysical Journal* 741.2, p. 68.

Matsui, T. and Osako, M. (1979). "Thermal property measurement of Yamato meteorites." In: *Mem. National Instit. Polar Res.* 15, pp. 243–252.

Maturilli, A., Helbert, J., and Moroz, L. (2008). "The Berlin emissivity database (BED)." In: *Planetary and Space Science* 56.3-4, pp. 420–425. DOI: 10.1016/j.pss.2007.11.015.

Maturilli, A., Helbert, J., Ferrari, S., Davidsson, B., and D'Amore, M. (2016). "Characterization of asteroid analogues by means of emission and reflectance spectroscopy in the 1- to 100-μm spectral range." In: *Earth, Planets and Space* 68.1. DOI: 10.1186/s40623-016-0489-y.

McCluney, W. (1994). *Introduction to Radiometry and Photometry*. 1st ed. ARTECH HOUSE, INC.

McSween, H. Y., Mittlefehldt, D. W., Beck, A. W., Mayne, R. G., and McCoy, T. J. (2010). "HED meteorites and their relationship to the geology of Vesta and the Dawn mission." In: *The Dawn Mission to Minor Planets 4 Vesta and 1 Ceres*. Springer, pp. 141–174.

Mellon, M., Jakosky, B., Kieffer, H., and Christensen, P. (2000). "High-Resolution Thermal Inertia Mapping from the Mars Global Surveyor Thermal Emission Spectrometer." In: *Icarus* 148.2, pp. 437–455. DOI: 10.1006/icar.2000.6503.

Michel, P., Richardson, D. C., Durda, D. D., Jutzi, M., and Asphaug, E. (2015). "Collisional Formation and Modeling of Asteroid Families." In: *Asteroids IV*. Ed. by P.

Michel, F. E. DeMeo, and W. F. Bottke. Tucson, AZ, USA: Univ. of Arizona Press, pp. 375–397.

Michel, P. and Delbo, M. (2010). "Orbital and thermal evolutions of four potential targets for a sample return space mission to a primitive near-Earth asteroid." In: *Icarus* 209.2, pp. 520–534.

Miyamoto, H., Yano, H., Scheeres, D. J., Abe, S., Barnouin-Jha, O., et al. (2007). "Regolith migration and sorting on asteroid Itokawa." In: *Science* 316.5827, pp. 1011–1014. DOI: 10.1126/science.1134390.

Mizuno, T., Kase, T., Shiina, T., Mita, M., Namiki, N., et al. (2017). "Development of the Laser Altimeter (LIDAR) for Hayabusa2." In: *Space Science Reviews* 208.1, pp. 33–47. DOI: 10.1007/s11214-015-0231-2.

Molaro, J. L., Byrne, S., and Langer, S. A. (2015). "Grain-scale thermoelastic stresses and spatiotemporal temperature gradients on airless bodies, implications for rock breakdown." In: *Journal of Geophysical Research: Planets* 120.2, pp. 255–277. DOI: 10.1002/2014je004729.

Molaro, J. L., Byrne, S., and Le, J. L. (2017). "Thermally induced stresses in boulders on airless body surfaces, and implications for rock breakdown." In: *Icarus* 294, pp. 247–261. DOI: 10.1016/j.icarus.2017.03.008.

Moskovitz, N. A., Abe, S., Pan, K.-S., Osip, D. J., Pefkou, D., et al. (2013). "Rotational characterization of Hayabusa II target Asteroid (162173) 1999 JU3." In: *Icarus* 224.1, pp. 24–31.

Muenow, D., Keil, K, and McCoy, T. J. (1995). "Volatiles in unequilibrated ordinary chondrites: Abundances, sources and implications for explosive volcanism on differentiated asteroids." In: *Meteoritics* 30.6, pp. 639–645.

Müller, T. G., Sekiguchi, T., Kaasalainen, M., Abe, M., and Hasegawa, S. (2005). "Thermal infrared observations of the Hayabusa spacecraft target asteroid 25143 Itokawa." In: *Astronomy & Astrophysics* 443.1, pp. 347–355. DOI: 10.1051/0004-6361:20053862.

Müller, T. G., Hasegawa, S., and Usui, F. (2014). "(25143) Itokawa: The power of radiometric techniques for the interpretation of remote thermal observations in the light of the Hayabusa rendezvous results." In: *Publications of the Astronomical Society of Japan* 66.3, pp. 52–52. DOI: 10.1093/pasj/psu034.

Müller, T. G., Durech, J., Ishiguro, M., Mueller, M., Krühler, T., et al. (2017). "Hayabusa-2 mission target asteroid 162173 Ryugu (1999 JU3): Searching for the object's spin-axis orientation." In: *Astronomy & Astrophysics* 599, A103. DOI: 10.1051/0004-6361/201629134.

Müller, T., Miyata, T, Kiss, C, Gurwell, M., Hasegawa, S, et al. (2013). "Physical properties of asteroid 308635 (2005 YU55) derived from multi-instrument infrared observations during a very close Earth approach." In: *Astronomy & Astrophysics* 558, A97.

Nakamura, T., Noguchi, T., Tanaka, M., Zolensky, M. E., Kimura, M., et al. (2011). "Itokawa dust particles: a direct link between S-type asteroids and ordinary chondrites." In: *Science* 333.6046, pp. 1113–6. DOI: 10.1126/science.1207758.

Nesvornỳ, D. and Bottke, W. F. (2004). "Detection of the Yarkovsky effect for main-belt asteroids." In: *Icarus* 170.2, pp. 324–342.

Neugebauer, G., Münch, G., Kieffer, H., Chase Jr., S. C., and Miner, E. (1971). "Mariner 1969 Infrared Radiometer Results: Temperatures and Thermal Properties of the Martian Surface." In: *The Astronomical Journal* 76, p. 719. DOI: 10.1086/111189.

Neumann, W., Breuer, D., and Spohn, T. (2014). "Modelling of compaction in planetesimals." In: *Astronomy & Astrophysics* 567, A120.

Neumann, W., Breuer, D., and Spohn, T. (2015). "Modelling the internal structure of Ceres: coupling of accretion with compaction by creep and implications for the water-rock differentiation." In: *Astronomy & Astrophysics* 584, A117.

Neumann, W., Henke, S., Breuer, D., Gail, H.-P., Schwarz, W. H., et al. (2018). "Modeling the evolution of the parent body of acapulcoites and lodranites: A case study for partially differentiated asteroids." In: *Icarus* 311, pp. 146–169.

Nowicki, S. A. and Christensen, P. R. (2007). "Rock abundance on Mars from the Thermal Emission Spectrometer." In: *Journal of Geophysical Research* 112, E05007. DOI: 10.1029/2006je002798.

Ogawa, K., Shirai, K., Sawada, H., Arakawa, M., Honda, R., et al. (2017). "System Configuration and Operation Plan of Hayabusa2 DCAM3-D Camera System for Scientific Observation During SCI Impact Experiment." In: *Space Science Reviews* 208.1, pp. 125–142. DOI: 10.1007/s11214-017-0347-7.

Okada, T., Fukuhara, T., Tanaka, S., Taguchi, M., Imamura, T., et al. (2017). "Thermal Infrared Imaging Experiments of C-Type Asteroid 162173 Ryugu on Hayabusa2." In: *Space Sci. Rev.* 208.1-4, pp. 255–286. DOI: 10.1007/s11214-016-0286-8.

Okuzumi, S., Tanaka, H., Kobayashi, H., and Wada, K. (2012). "RAPID COAGULATION OF POROUS DUST AGGREGATES OUTSIDE THE SNOW LINE: A PATHWAY TO SUCCESSFUL ICY PLANETESIMAL FORMATION." In: *The Astrophysical Journal* 752.2, p. 106. DOI: 10.1088/0004-637x/752/2/106.

Opeil, C. P., Consolmagno, G. J., and Britt, D. T. (2010). "The thermal conductivity of meteorites: New measurements and analysis." In: *Icarus* 208.1, pp. 449–454. ISSN: 00191035. DOI: 10.1016/j.icarus.2010.01.021.

Opeil, C. P., Consolmagno, G. J., Safarik, D. J., and Britt, D. T. (2012). "Stony meteorite thermal properties and their relationship with meteorite chemical and physical states." In: *Meteoritics & Planetary Science* 47.3, pp. 319–329. ISSN: 1086-9379. DOI: 10.1111/j.1945-5100.2012.01331.x.

Ormel, C. W., Spaans, M., and Tielens, A. G. G. M. (2007). "Dust coagulation in protoplanetary disks: porosity matters." In: *A&A* 461.1, pp. 215–232. DOI: 10.1051/0004-6361:20065949.

Ostrowski, D and Bryson, K (2019). "The physical properties of meteorites." In: *Planetary and Space Science* 165, pp. 148 –178. ISSN: 0032-0633. DOI: https://doi.org/10.1016/j.pss.2018.11.003.

Paddack, S. J. (1969). "Rotational bursting of small celestial bodies: Effects of radiation pressure." In: *Journal of Geophysical Research* 74.17, pp. 4379–4381. DOI: 10.1029/JB074i017p04379.

Paige, D. A., Foote, M. C., Greenhagen, B. T., Schofield, J. T., Calcutt, S., et al. (2010). "The Lunar Reconnaissance Orbiter Diviner Lunar Radiometer Experiment." In: *Space Science Reviews* 150.1, pp. 125–160. DOI: 10.1007/s11214-009-9529-2.

Pelivan, I., Drube, L., Kührt, E., Helbert, J., Biele, J., et al. (2017). "Thermophysical modeling of Didymos' moon for the Asteroid Impact Mission." In: *Advances in Space Research* 59.7, pp. 1936–1949. DOI: 10.1016/j.asr.2016.12.041.

Piqueux, S. and Christensen, P. R. (2009a). "A model of thermal conductivity for planetary soils: 1. Theory for unconsolidated soils." In: *J. Geophys. Res.* 114, E09005. DOI: 10.1029/2008je003309.

Piqueux, S. and Christensen, P. R. (2009b). "A model of thermal conductivity for planetary soils: 2. Theory for cemented soils." In: *J. Geophys. Res.* 114, E09006. DOI: 10.1029/2008je003309.

Piqueux, S. and Christensen, P. R. (2011). "Temperature-dependent thermal inertia of homogeneous Martian regolith." In: *Journal of Geophysical Research* 116.E07004. DOI: 10.1029/2011je003805.

Popova, O., Borovička, J., Hartmann, W. K., Spurnỳ, P., Gnos, E., et al. (2011). "Very low strengths of interplanetary meteoroids and small asteroids." In: *Meteoritics & Planetary Science* 46.10, pp. 1525–1550.

Pravec, P. and Harris, A. W. (2000). "Fast and slow rotation of asteroids." In: *Icarus* 148.1, pp. 12–20.

Press, W. H., Teukolsky, S. A., Vetterling, W. T., and Flannery, B. P. (1992). *Numerical Recipes in C (2Nd Ed.): The Art of Scientific Computing*. New York, NY, USA: Cambridge University Press. Chap. 15, pp. 659–661.

Prockter, L, Murchie, S, Cheng, A, Krimigis, S, Farquhar, R, et al. (2002). "The NEAR shoemaker mission to asteroid 433 eros." In: *Acta Astronautica* 51.1-9, pp. 491–500.

Putzig, N. and Mellon, M. (2007). "Apparent thermal inertia and the surface heterogeneity of Mars." In: *Icarus* 191.1, pp. 68–94. DOI: 10.1016/j.icarus.2007.05.013.

Ralchenko, M, Britt, D., Samson, C, Herd, C., Herd, R., et al. (2014). "Bulk physical properties of the Tagish Lake meteorite frozen pristine fragments." In: *Lunar and Planetary Science Conference*. Vol. 45, p. 1021.

Rayner, J., Toomey, D., Onaka, P., Denault, A., Stahlberger, W., et al. (2003). "SpeX: a medium-resolution 0.8–5.5 micron spectrograph and imager for the NASA infrared telescope facility." In: *Publications of the Astronomical Society of the Pacific* 115.805, p. 362.

Reddy, V., Dunn, T. L., Thomas, C. A., Moskovitz, N. A., and H., B. T. (2015). "Mineralogy and Surface Composition of Asteroids." In: *Asteroids IV*. Ed. by P. Michel, F. E. DeMeo, and W. F. Bottke. Tucson, AZ, USA: Univ. of Arizona Press, pp. 43–65.

Robinson, M. S., Thomas, P. C., Veverka, J., Murchie, S., and Carcich, B. (2001). "The nature of ponded deposits on Eros." In: *Nature* 413, p. 396. DOI: 10.1038/35096518.

Rubincam, D. P. (1995). "Asteroid orbit evolution due to thermal drag." In: *J.Geophys.Res.: Planets* 100.E1, pp. 1585–1594. DOI: 10.1029/94JE02411.

Rubincam, D. P. (2000). "Radiative spin-up and spin-down of small asteroids." In: *Icarus* 148.1, pp. 2–11.

Russell, C. and Raymond, C. (2011). "The dawn mission to Vesta and Ceres." In: *The Dawn Mission to Minor Planets 4 Vesta and 1 Ceres*. Springer, pp. 3–23.

Saiki, T., Imamura, H., Arakawa, M., Wada, K., Takagi, Y., et al. (2017). "The Small Carry-on Impactor (SCI) and the Hayabusa2 Impact Experiment." In: *Space Science Reviews* 208.1, pp. 165–186. DOI: 10.1007/s11214-016-0297-5.

Saiki, T., Sawada, H., Okamoto, C., Yano, H., Takagi, Y., et al. (2013). "Small carry-on impactor of Hayabusa2 mission." In: *Acta Astronautica* 84, pp. 227 –236. DOI: https://doi.org/10.1016/j.actaastro.2012.11.010.

Saito, J., Miyamoto, H., Nakamura, R., Ishiguro, M., Michikami, T., et al. (2006). "Detailed images of asteroid 25143 Itokawa from Hayabusa." In: *Science* 312.5778, pp. 1341–1344. DOI: 10.1126/science.1125722.

Sakatani, N., Ogawa, K., Iijima, Y., Arakawa, M., Honda, R., et al. (2017). "Thermal conductivity model for powdered materials under vacuum based on experimental studies." In: *AIP Advances* 7 (015310). DOI: 10.1063/1.4975153.

Sakatani, N., Ogawa, K., Arakawa, M., and Tanaka, S. (2018). "Thermal conductivity of lunar regolith simulant JSC-1A under vacuum." In: *Icarus* 309, pp. 13–24. ISSN: 00191035. DOI: 10.1016/j.icarus.2018.02.027.

Salisbury, J. W., D'Aria, D. M., and Jarosewich, E. (1991). "Midinfrared (2.5–13.5 μm) reflectance spectra of powdered stony meteorites." In: *Icarus* 92.2, pp. 280–297. ISSN: 0019-1035. DOI: https://doi.org/10.1016/0019-1035(91)90052-U.

Salisbury, J. W. and Hunt, G. R. (1974). "Meteorite spectra and weathering." In: *Journal of Geophysical Research* 79.29, pp. 4439–4441.

Sánchez, D. P. and Scheeres, D. J. (2012). "DEM simulation of rotation-induced reshaping and disruption of rubble-pile asteroids." In: *Icarus* 218.2, pp. 876–894.

Scheeres, D. J. (2015). "Landslides and Mass shedding on spinning spheroidal asteroids." In: *Icarus* 247, pp. 1–17. ISSN: 0019-1035. DOI: https://doi.org/10.1016/j.icarus.2014.09.017.

Scheeres, D., McMahon, J., French, A., Brack, D., Chesley, S., et al. (2019). "The dynamic geophysical environment of (101955) Bennu based on OSIRIS-REx measurements." In: *Nature Astronomy* 3.4, p. 352.

Scholz, C. H. (2002). *The Mechanics of Earthquakes and Faulting*. 2nd ed. Cambridge University Press.

Schulz, R, Sierks, H, Küppers, M, and Accomazzo, A (2012). "Rosetta fly-by at asteroid (21) Lutetia: An overview." In: *Planetary and Space Science* 66.1, pp. 2–8.

Sears, D. W., Kallemeyn, G. W., and Wasson, J. T. (1982). "The compositional classification of chondrites: II The enstatite chondrite groups." In: *Geochimica et Cosmochimica Acta* 46.4, pp. 597–608.

Spencer, J. R., Lebofsky, L. A., and Sykes, M. V. (1989). "Systematic biases in radiometric diameter determinations." In: *Icarus* 78.2, pp. 337–354.

Spohn, T., Seiferlin, K., Hagermann, A., Knollenberg, J., Ball, A. J., et al. (2007). "Mupus – A Thermal and Mechanical Properties Probe for the Rosetta Lander Philae." In: *Space Science Reviews* 128.1, pp. 339–362. DOI: 10.1007/s11214-006-9081-2.

Spohn, T., Knollenberg, J., Ball, A. J., Banaszkiewicz, M., Benkhoff, J., et al. (2015). "Thermal and mechanical properties of the near-surface layers of comet 67P/Churyumov-Gerasimenko." In: *Science* 349.6247, aab0464. DOI: 10.1126/science.aab0464.

Statler, T. S. (2009). "Extreme sensitivity of the YORP effect to small-scale topography." In: *Icarus* 202.2, pp. 502–513.

Sugita, S., Honda, R., Morota, T., Kameda, S., Sawada, H., et al. (2019). "The geomorphology, color, and thermal properties of Ryugu: Implications for parent-body processes." In: *Science* 364.6437, eaaw0422.

Szurgot, M., Wach, R. A., and Przylibski, T. A. (2012). "Thermophysical properties of the Sołtmany meteorite." In: *Meteorites* 2.

Takir, D. and Emery, J. P. (2012). "Outer Main Belt asteroids: Identification and distribution of four 3-μm spectral groups." In: *Icarus* 219.2, pp. 641–654. DOI: https://doi.org/10.1016/j.icarus.2012.02.022.

Takita, J., Senshu, H., and Tanaka, S. (2017). "Feasibility and Accuracy of Thermophysical Estimation of Asteroid 162173 Ryugu (1999 JU3) from the Hayabusa2 Thermal Infrared Imager." In: *Space Science Reviews* 208.1-4, pp. 287–315. DOI: 10.1007/s11214-017-0336-x.

Taylor, P. A., Margot, J.-L., Vokrouhlickỳ, D., Scheeres, D. J., Pravec, P., et al. (2007). "Spin rate of asteroid (54509) 2000 PH5 increasing due to the YORP effect." In: *Science* 316.5822, pp. 274–277.

Tholen, D. J. and Barucci, M. A. (1989). "Asteroid taxonomy." In: *Asteroids II*. Ed. by R. P. Binzel, T. Gehrels, and M. S. Matthews. Tucson, AZ, USA: Univ. of Arizona Press, pp. 298–315.

Thomas, P. C., Veverka, J., Robinson, M. S., and Murchie, S. (2001). "Shoemaker crater as the source of most ejecta blocks on the asteroid 433 Eros." In: *Nature* 413, pp. 394–396. DOI: 10.1038/35096513.

Tonui, E., Zolensky, M., Hiroi, T., Nakamura, T., Lipschutz, M. E., et al. (2014). "Petrographic, chemical and spectroscopic evidence for thermal metamorphism in carbonaceous chondrites I: CI and CM chondrites." In: *Geochimica et Cosmochimica Acta* 126, pp. 284–306.

Tosi, F., Capria, M. T., De Sanctis, M. C., Combe, J. P., Zambon, F., et al. (2014). "Thermal measurements of dark and bright surface features on Vesta as derived from Dawn/VIR." In: *Icarus* 240, pp. 36–57. DOI: 10.1016/j.icarus.2014.03.017.

Tsuda, Y., Yoshikawa, M., Abe, M., Minamino, H., and Nakazawa, S. (2013). "System design of the Hayabusa 2—Asteroid sample return mission to 1999 JU3." In: *Acta Astronautica* 91, pp. 356–362. DOI: 10.1016/j.actaastro.2013.06.028.

Ushikubo, T., Nakashima, D., Kimura, M., Tenner, T. J., and Kita, N. T. (2013). "Contemporaneous formation of chondrules in distinct oxygen isotope reservoirs." In: *Geochimica et Cosmochimica Acta* 109, pp. 280 –295. ISSN: 0016-7037. DOI: https://doi.org/10.1016/j.gca.2013.01.045.

Van Schmus, W. and Wood, J. A. (1967). "A chemical-petrologic classification for the chondritic meteorites." In: *Geochimica et Cosmochimica Acta* 31.5, pp. 747–765.

Vasavada, A. R., Piqueux, S., Lewis, K. W., Lemmon, M. T., and Smith, M. D. (2017). "Thermophysical properties along Curiosity 's traverse in Gale crater, Mars, derived from the REMS ground temperature sensor." In: *Icarus* 284, pp. 372–386. DOI: 10.1016/j.icarus.2016.11.035.

Veverka, J, Thomas, P, Harch, A, Clark, B, Bell III, J., et al. (1999). "NEAR encounter with asteroid 253 Mathilde: overview." In: *Icarus* 140.1, pp. 3–16.

Viles, H., Ehlmann, B., Wilson, C. F., Cebula, T., Page, M., et al. (2010). "Simulating weathering of basalt on Mars and Earth by thermal cycling." In: *Geophysical Research Letters* 37.18, p. L18201. DOI: doi:10.1029/2010GL043522.

Wada, K., Grott, M., Michel, P., Walsh, K. J., Barucci, A. M., et al. (2018). "Asteroid Ryugu before the Hayabusa2 encounter." In: *Progress in Earth and Planetary Science* 5.1, p. 82. DOI: 10.1186/s40645-018-0237-y.

Walsh, K. J., Richardson, D. C., and Michel, P. (2008). "Rotational breakup as the origin of small binary asteroids." In: *Nature* 454.7201, p. 188.

Watanabe, S., Tsuda, Y., Yoshikawa, M., Tanaka, S., Saiki, T., et al. (2017). "Hayabusa2 Mission Overview." In: *Space Science Reviews* 1, pp. 3–16. DOI: 10.1007/s11214-017-0377-1.

Watanabe, S, Hirabayashi, M, Hirata, N, Hirata, N., Noguchi, R, et al. (2019). "Hayabusa2 arrives at the carbonaceous asteroid 162173 Ryugu—A spinning top–shaped rubble pile." In: *Science* 364.6437, pp. 268–272.

Weisberg, M. K., Prinz, M., Clayton, R. N., Mayeda, T. K., Grady, M. M., et al. (1996). "The K (Kakangari) chondrite grouplet." In: *Geochimica et Cosmochimica Acta* 60.21, pp. 4253–4263.

Yamada, R., Senshu, H., Namiki, N., Mizuno, T., Abe, S., et al. (2017). "Albedo Observation by Hayabusa2 LIDAR: Instrument Performance and Error Evaluation." In: *Space Science Reviews* 208.1, pp. 49–64. DOI: 10.1007/s11214-016-0240-9.

Yang, R., Zou, R., and Yu, A. (2000). "Computer simulation of the packing of fine particles." In: *Physical review E* 62.3, pp. 3900–3908.

Yano, H., Kubota, T., Miyamoto, H., Okada, T., Scheeres, D., et al. (2006). "Touchdown of the Hayabusa spacecraft at the Muses Sea on Itokawa." In: *Science* 312.5778, pp. 1350–1353. DOI: 10.1126/science.1126164.

Yeomans, D., Chodas, P., Keesey, M., Owen, W., and Wimberly, R. (1993). "Targeting an asteroid-The Galileo spacecraft's encounter with 951 Gaspra." In: *The Astronomical Journal* 105, pp. 1547–1552.

Yomogida, K. and Matsui, T. (1983). "Physical properties of ordinary chondrites." In: *Journal of Geophysical Research: Solid Earth* 88.B11, pp. 9513–9533.

Youdin, A. N. and Goodman, J. (2005). "Streaming instabilities in protoplanetary disks." In: *The Astrophysical Journal* 620.1, p. 459.

Čapek, D. and Vokrouhlický, D. (2010). "Thermal stresses in small meteoroids." In: *Astronomy and Astrophysics* 519. ISSN: 0004-6361 1432-0746. DOI: 10.1051/0004-6361/201014281.

Čapek, D. and Vokrouhlický, D. (2012). "Thermal stresses in small meteoroids." In: *Astronomy & Astrophysics* 539. ISSN: 0004-6361 1432-0746. DOI: 10.1051/0004-6361/201117697.

自分が竜宮城に行ってからなんと

300年も経ってしまったということを知りました。

It was then that Taro learned that three hundred years had passed since he had gone to Ryugu-jo.
(From "The Tale of Urashima Taro")[1]

1 https://www.gov-online.go.jp/eng/publicity/book/hlj/html/201407/201407_09_jp.html

COLOPHON

This document was typeset using the typographical look-and-feel `classicthesis` template developed by André Miede and Ivo Pletikosić. The style was inspired by Robert Bringhurst's seminal book on typography "*The Elements of Typographic Style*".